Title

Evaluating and targeting mechanisms of immune evasion in cancer

Author

Solomon, Paige Elana

Publication Date

2023

Peer reviewed|Thesis/dissertation

Evaluating and targeting mechanisms of immune evasion in cancer

by
Paige Solomon

DISSERTATION
Submitted in partial satisfaction of the requirements for degree of
DOCTOR OF PHILOSOPHY

in

Chemistry and Chemical Biology

in the

GRADUATE DIVISION
of the
UNIVERSITY OF CALIFORNIA, SAN FRANCISCO

Approved:

DocuSigned by:
James A. Wells
5F2F4D1A06164C2...

James A. Wells
Chair

DocuSigned by:
Michael T. McManus
[illegible]

Michael T. McManus

DocuSigned by:
Davide Ruggero
[illegible]

Davide Ruggero

DocuSigned by:
Hiten D. Madhani
242AFD8ACF95471...

Hiten D. Madhani

Committee Members

Acknowledgements

My graduate experience at UCSF has been incredible, and I would like to thank the people that have contributed so meaningfully to my education and enriched the last six years with so much joy.

I am extremely grateful to my advisor, Jim Wells. You are an exemplar of how adventurous and critical thinking leads to scientific achievement. Your trust, mentorship, and constant support have given me the skills and the confidence to follow my own scientific curiosities. Thank you for cultivating the type of lab that attracts bright and energetic individuals from across the world, who have become my collaborators, mentors, and friends. I will remember my time in the Wells lab fondly, and I am so honored to be your trainee.

I would like to thank my previous mentors Fred Ernani, Jenny Nelson, and Parag Mallik. Thank you for investing your time and mentorship in me when I was a young and green scientist, and thank you for the continued support and check-ins throughout graduate school.

I would like to thank all my collaborators who made this research possible: Cole Bracken, Lisa Kirkemo, Kevin Leung, Leanne Sayles, Betsy Young, Shoshana Zha, Mark Almond, Gary Wilson, Jacqueline Carozza, Haoqing Wang, Alon Wellner, Alejandro Sweet-Cordero, Oren Rosenberg, Josh Coon, Lingyin Li, and, Chang Liu. These scientific achievements would not have been possible without your skills and expertise. Thank you to my thesis committee members Davide Ruggero, Michael McManus, and Hiten Madhani for your time, guidance, and support.

Thank you to all the members of the Wells lab. I am fortunate to have worked with Jamie Byrnes and Katie Schaeffer, two brilliant postdocs who have gifted me with invaluable

mentorship and friendship. Nick Rettko, thank you for lighting up the lab with your hilarious jokes, engaging conversations, and murder mystery parties. Irene Liu, you are one-of-a-kind. Thank you for your kindness, impeccable taste in music, and extremely dark humor. Cole Bracken, the laughter, positivity, and support you have given me is unmatched. It is so special to have shared the graduate school experience with you, and I feel lucky to have found a best friend here. I would also like to thank my other good friends in the CCB cohort, Adam Cotton and Paul Klauser.

Thank you to my best friends: Jean Montag, Sarah Maisel, Eliza Thompson, Megan Cai, Adebia Ntoso, Alison Feldman, Emily Aguilar, and Kassidy Iwashita. You have brought me joy, humor, excitement, and balance that kept me afloat during graduate school. Spending time with you was always a source of energy. Thank you to the greater Leavenworth group of friends for the endless fun and lasting memories together.

Finally, I want to thank my family, Edward Solomon, Darlene Solomon, and Mitchell Solomon. Thank you for your unconditional support and love that have brought me to this point. Mitchell, as the only non-scientist in our family you have gone out of your way to learn about my research and cheer me on. Thank you for being someone I can always count on. Mom, you are the most self-less and kind-hearted person in my life. You have shown me what it looks like to have a successful career, while always lifting up the people around you, and still making it to yoga three times a week. Dad, your intelligence and life-long dedication to scientific pursuit inspire me each day. Thank you for motivating me to achieve and be my best, and always being my source of logic, comfort, and humor along the way. Mom and dad, you are two of the greatest scientific role models a person could have. Except for naming our childhood dogs Schroedinger and Dirac, you never pushed Mitchell or me into science or your footprints. Thank you for

sharing the world you love, but allowing me space and time to find my own identity and purpose as a scientist. Making you proud has been constant driving force for me. Mitchell and I are so lucky to have you as our parents.

Contributions

Chapter 1 of this thesis is a reprint of the material as it appears in:

Solomon, P.E., Kirkemo, L.L., Wilson, G.M., Leung, K.K., Almond, M.H., Sayles, L.C., Sweet-Cordero, E.A., Rosenberg, O.S., Coon, J.J. and Wells, J.A., 2022. Discovery Proteomics Analysis Determines That Driver Oncogenes Suppress Antiviral Defense Pathways Through Reduction in Interferon-β Autocrine Stimulation. *Molecular & Cellular Proteomics*, *21*(7).

Chapter 2 of this thesis is a reprint of the material as it has been submitted to *Nat Chem Biol*.:

Solomon, P.E., Bracken, C.J., Carozza, J.A., Wang, H., Young, E.P., Wellner, A., Chang, C.L., Sweet-Cordero, E.A., Li, L., and Wells, J.A., 2023. Discovery of VH domains that allosterically inhibit human ENPP1, a target critical for immune suppression in cancer.

Evaluating and targeting mechanisms of immune evasion in cancer

By

Paige E. Solomon

Abstract

Immunotherapies such as adoptive cell therapies and checkpoint inhibitors are curing previously lethal cancers, however only a small fraction of patients are responsive. A major predictor of the response to immunotherapy is the extent of tumor infiltrating lymphocytes (TILs) in the tumor microenvironment. Unfortunately, most solid tumors exclude TILs through various immunosuppressive mechanisms and are classified as immune 'cold' tumors. In this thesis research, we studied how the expression of dominant oncogenes broadly modulates immune evasion phenotypes across cancer models. We translated those findings into therapeutic antibodies that stimulate innate immune pathways to turn immune 'cold' tumors 'hot' and improve response rates to immunotherapies.

In Chapter 1 we used discovery proteomics to characterize isogenic models of driver oncogenes (Myc, KRAS, BRAF, MEK, AKT, HER2, EGFR) and identify common axes of dysregulation. From an unbiased approach, the most ubiquitous and dramatic molecular and functional phenotype across oncogenes was the suppression of proteins regulated by type 1 interferon, particularly antiviral dsRNA sensors. These effects were validated in patient- and cancer-derived tumor cells driven by KRAS and/or Myc oncogenes. These results have broad implications for standard therapies like radiation, epigenetic and cytotoxic drugs, and

immunotherapies that require type 1 interferon and antiviral pathways for their cytotoxic effects, and suggest opportunities for oncolytic and gene-therapy viruses.

In Chapter 2 we used *in vitro* display technologies and protein engineering to build therapeutic antibodies that re-activate innate immune signaling in the tumor microenvironment. ENPP1 is an extracellular phosphodiesterase that hydrolyzes cGAMP, an immunostimulant that is transported between cells to activate type 1 interferon. ENPP1 is frequently up-regulated on tumor cells, and small molecule drugs have shown inhibiting ENPP1 stimulates type 1 interferon signaling and sensitizes immune 'cold' tumors to radiation and immunotherapy. Here, we generated first-in-class variable heavy (VH) single-domain antibodies that bind and allosterically inhibit ENPP1. The VH domains were recombinantly engineered into multivalent formats and immunotherapies that improved their selectivity and potency. A cryo-EM structure of the VH-ENPP1 complex revealed its allosteric inhibitory epitope and a novel mechanism of substrate-selective inhibition.

Table of Contents

List of Figures

List of Tables

Chapter 1

Discovery proteomics analysis determines that driver oncogenes suppress antiviral defense pathways through reduction in interferon-β autocrine stimulation

1.1 Abstract

Since the discovery of oncogenes there has been tremendous interest to understand their mechanistic basis and to develop broadly actionable therapeutics. Some of the most frequently activated oncogenes driving diverse cancers are c-MYC, EGFR, HER2, AKT, KRAS, BRAF, and MEK. Using a reductionist approach, we explored how cellular proteomes are remodeled in isogenic cell lines engineered with or without these driver oncogenes. The most striking discovery for all seven oncogenic models was the systematic down-regulation of scores of antiviral proteins regulated by Type 1 interferon (T1IFN). These findings extended to cancer cell lines and PDX models of highly refractory pancreatic cancer and osteosarcoma driven by KRAS and MYC oncogenes. The oncogenes reduced basal expression of and autocrine stimulation by T1IFN

causing remarkable convergence on common phenotypic and functional profiles. In particular, there was dramatically lower expression of dsRNA sensors including DDX58 (RIG-I) and OAS proteins, which resulted in attenuated functional responses when the oncogenic cells were treated with the dsRNA mimetic, polyI:C, and increased susceptibility to infection with an RNA virus. Our reductionist approach provides molecular and functional insights connected to immune evasion hallmarks in cancers and suggests therapeutic opportunities.

1.2 Introduction

Cancer is dominated by a set of driver oncogenes that remodel cellular physiology to achieve hallmarks of the disease(1, 2). c-MYC (MYC), EGFR, HER2, AKT, KRAS, BRAF, and MEK are classic examples of powerful oncogenes that activate several distinct tumorigenic axes in cancers(3–5). For example, MYC is a master transcriptional regulator for thousands of genes that coordinate cellular proliferation and biogenesis(6, 7). MYC is dysregulated in more than 50% of cancers of all tissues, but is especially implicated in prostate cancers and B-cell cancers such as Burkitt's lymphoma, which is driven by chromosomal translocation of MYC(7–9). MYC copy number amplification has also been correlated to the metastatic progression of osteosarcoma (OS), a highly pediatric bone cancer that becomes severely fatal in advanced disease(10, 11). The signal transduction oncogenes regulate the MAPK (KRAS/BRAF/MEK) or PI3K/AKT proliferation pathways that are activated by the growth receptors EGFR and HER2. Mutant KRAS is the most prominent oncogene in human cancers, and in particular pancreatic cancer carries the highest rate of mutation to KRAS and is one of the most lethal types of tumor(12–14). Another signaling oncogene is AKT, a kinase that functions within the PI3K proliferative transduction pathway.

Activation of AKT is present in many cancers, including over 40% of breast cancers, and is a predictor of poor prognosis and drug resistance(15, 16).

There is considerable interest in understanding the molecular changes induced by driver oncogenes to identify unifying hallmarks and broader drug targets(1, 2). Molecular studies using cancer cell lines, patient-derived xenograft (PDX) models, and primary tumors clearly demonstrate that tumor development drives massive multi-omics changes. A challenge is that these human cancer-derived systems usually have unique combinations of genomic mutations making it difficult to attribute specific molecular changes to each oncogene and confounding the generalizability for target discovery. To reduce the complexity, investigators have used isogenic cell lines that knock-out or overexpress specific oncogenes to measure the consequences of isolated molecular perturbations. These reductionist experiments can systematically define the changes driven by oncogenes, building fundamental knowledge to interrogate diverse cancers. Although not based directly on complex primary human tumors, isogenic studies allow control of a single gene and are renewable platforms to identify common hallmarks and broad drug targets across oncogenes.

We previously engineered a series of isogenic cell lines with or without seven different driver oncogenes, MYC, EGFR, HER2, AKT, KRAS, BRAF, and MEK, to specifically identify membrane proteins that change for targeting by immunotherapy(17, 18). Here we apply discovery proteomics for each of these isogenic cell lines to understand oncogene-driven remodeling of the cytosolic proteome and to identify conserved dysregulation across multiple oncogenes. The most remarkable result for all oncogenes and models tested was the down-regulation of Type 1 interferon (T1IFN) and antiviral response proteins, especially those associated with viral dsRNA sensing. This effect was also dramatically seen in two PDX models of metastatic OS with high

MYC copy number as well as two pancreatic ductal adenocarcinoma (PDAC) cell lines driven by KRAS mutation and MYC amplification. Using systematic molecular and functional analyses, we demonstrate cells expressing oncogenes have impaired dsRNA-sensing antiviral responses and increased susceptibility to RNA virus. These findings are relevant to immune evasion hallmarks in cancer and have implications for the efficacies of radiation, genotoxic, epigenetic, immune, and viral therapies that utilize interferon and antiviral pathways.

1.3 Results

Integrative proteomic analysis of cells expressing driver oncogenes identified massive suppression of T1IFN and antiviral response pathways.

We used label-free whole cell proteomics to characterize the effect of MYC overexpression for two isogenic MYC models. P493-6 cells are an isogenic model of Burkitt's lymphoma and overexpress MYC on a tetracycline-repressible promotor(30). P493-6 cells were treated in the presence or absence of tetracycline to generate low or high MYC expression cell lines, respectively. As a second isogenic model, LHS-PrEC (LHS) prostate epithelial cells were engineered with a MYC overexpression plasmid or an empty vector (EV) control(18). We additionally tested two PDX cell lines of metastatic OS carrying high MYC copy amplification (OS152 and OS186) and compared these to normal human fetal osteoblasts (hFOB)(10). In total the cell lines span lymphocyte, epithelial, and mesenchymal cancer subtypes providing a broad cellular view of MYC overexpression.

Mass spectrometry detected 3,579, 3,449, and 4,235 proteins for the P493-6, LHS, and OS MYC models respectively, and showed that overexpression of the MYC oncogene causes bidirectional changes to hundreds of proteins (**Figure 1.1**, ProteomeXchange identifier

PXD033373). While expression levels of individual proteins differed among the cell lines, gene set enrichment for each data set harmonized at the pathway level as previously noted for MYC overexpression cell surface proteomes(18). For example, metabolism and ribosome biogenesis pathways classically connected to MYC tumorigenesis were up-regulated at the systems level(6, 31). As the LHS, P493-6, and OS have distinct cellular backgrounds, the overlap of individual protein targets was more moderate. The two isogenic MYC models, P493-6 and LHS, shared a set of seven up-regulated proteins ($p \leq 0.05$, $\log_2 FC \geq 1$), and two of these proteins were also significantly up-regulated in the OS PDX cell lines. Both isogenic MYC cell lines also commonly down-regulated 15 proteins ($p \leq 0.05$, $\log_2 FC \leq -1$), and 11 of these proteins were significantly decreased in the OS PDX cell lines (**Figure 1**). Strikingly, the proteins and gene-set enrichment pathways ubiquitously suppressed by MYC in all four isogenic and PDX models converged on T1IFN and antiviral pathways (**Supplemental Table 1.S1**). For individual isogenic and PDX systems, MYC expression significantly down-regulated respective combinations of up to 28 interferon and antiviral effectors, and these represented four out of the 11 proteins commonly suppressed across all four MYC models. Moreover, the fold-changes for these proteins were some of the most dramatic in the data set, most ranging from 4- to over 200-fold reduced.

To assess changes induced by proliferative signal transduction oncogenes—the tyrosine kinases EGFR and HER2, or the down-stream effectors AKT, KRAS, BRAF, and MEK—MCF10A cells were engineered to overexpress HER2 or to express the common, constitutively active oncogenic forms of $KRAS^{G12V}$, $EGFR^{L858R}$, $BRAF^{V600E}$, $MEK^{S218D/S222D}$, or myristoylated AKT(17). The oncogenic cells and comparator control cells expressing the empty vector (EV), were characterized by label-free whole cell proteomics that detected 5,292 individual proteins for each isogenic model. The data is reported in ProteomeXchange with identifier PXD033373. Each

oncogene caused large up- and down-regulation for hundreds of proteins (**Figure 1.1**). Although these oncogenes neighbor one another in signal transduction pathways, there was no overlap at the individual protein level, suggesting differences in the specific perturbations that each drives(17, 32, 33). As with MYC, these differences aligned when viewed at the gene-set level underscoring effective functional redundancy. Commonly up-regulated pathways centered on signaling cascades (such as EGFR, PI3K, and Rho GTPase) as well as cell cycle and mitotic processes.

Most strikingly, expression of each signal transduction oncogene caused dramatic down-regulation of scores of T1IFN response and antiviral pathway proteins (between 21 and 28 proteins in each data set); these pathways were also significantly enriched by gene-set analysis for each proteomics data set (**Supplemental Table 1.S1**). In total only a set of 11 proteins were commonly suppressed ($p \leq 0.05$, $\log_2 FC \leq -1$) for all six proliferative oncogenes, and the majority of these proteins (6/11) were effectors of T1IFN and antiviral response pathways (**Figure 1.1).**

Finally, protein expression profiles for two tissue-derived PDAC cancers, KP4 and PSN1, compared to normal human pancreatic ductal epithelial (HPDE) cells were characterized by label-free whole cell proteomics. Raw data is presented in ProteomeXchange with identifier PXD033373. KP4 and PSN1 belong to the most aggressive basal (quasi-mesenchymal) subtype of PDAC tumors(34, 35). KP4 and PSN1 are driven by $KRAS^{G12D}$ and $KRAS^{G12R}$ mutations, respectively, as well as amplification of MYC (**Supplemental Figure 1.S1**)(13, 34, 36–38). Proteomics demonstrated decreased T1IFN and antiviral response machinery in the basal PDAC models and gene-set analysis identified significant interferon pathway suppression (**Supplemental Table 1.S1**). Of over 3,300 targets detected by proteomics, 54 and 69 proteins were commonly up- or down-regulated, respectively, in both PDAC cell lines. Four of these were down-regulated antiviral proteins ($p \leq 0.05$, $\log_2 FC \leq -1$), three of which were also down-regulated in the isogenic

$KRAS^{G12V}$ model. This included HLA-A, which was the only protein found commonly dysregulated across the six isogenic models for proliferative oncogenes and both PDAC cell lines.

The proteomics results are depicted by a color-coded schema to contextualize the dysregulation of three different antiviral pathways (**Figure 1.1**). These antiviral systems mitigate invading viral pathogens through designated sensor proteins that detect either dsRNA or dsDNA viral genomes or replication intermediates in the cytosol(39). One particular function of nucleic acid sensors is to initiate signaling cascades that activate transcription of T1IFN: IFNα and IFNβ (**Figure 1.1**). In this T1IFN-inducing pathway, the major cytoplasmic dsRNA sensors are DDX58 (RIG-I), MDA5 (IFIH1), and LGP2 (DHX58) and the parallel main cytoplasmic dsDNA sensors are CGAS, DDX41, and IFI16. Ligand-activated dsRNA and dsDNA sensors signal through the adaptor proteins MAVS and STING (TMEM173), respectively. Downstream these separate pathways converge on phosphorylation of TBK1, inducing phosphorylation and nuclear translocation of IRF3 and IRF7, that control the transcription of IFNα and IFNβ. IFNα and IFNβ proteins are secreted from cells and in autocrine and paracrine fashions bind the interferon receptor (IFNAR1 and IFNAR2) causing signal transduction that drives formation of the ISGF3 complex (IRF9, STAT1, and STAT2). ISGF3 activates transcription of hundreds of interferon-stimulated genes (ISGs), and these proteins coordinate the cellular antiviral defense via mitigating viral entry, replication, transcription, and translation processes(39, 40). In a second major antiviral system, OAS proteins (OAS1, OAS2, and OAS3) are sensors activated by cytosolic dsRNA to catalyze the production of 2'-5' linked oligoadenylates typically 4-8 in length that activate the latent RNASEL (**Figure 1.1C**). Activated RNASEL indiscriminately cleaves cellular RNA to obstruct the viral replication cycle(40, 41). Finally, one additional dsRNA sensor, EIF2AK2 (PKR), negatively regulates translational machinery to prevent viral protein synthesis(40) (**Figure 1.1**).

Remarkably, all seven oncogenes significantly down-regulated proteins acting in these three major antiviral response pathways (**Figure 1.1**). These repressed effectors are also well-annotated ISGs, controlled by interferon-stimulated response elements (ISRE) in their gene regulatory regions. Moreover, there were large magnitudes of suppression (most between 4- to over 200-fold) of more than 35 other ISGs including HLA, B2M, and TAP1/2 proteins involved in antigen presentation, , STAT proteins, ISG15, MX1, and IFIT3 (**Figure 1.1**)(40, 42). The pronounced and global depletion of ISGs implicated that T1IFN could be central in disseminating an ISG-suppressed phenotype in cells expressing oncogenes.

Depletion of MYC and inhibition of MAPK signaling validates their regulation over interferon and antiviral pathways in PDAC and OS tumor-derived models.

Systematic suppression of ISGs was identified for tumor-derived OS and PDAC cell lines when compared to normal cell lines. In addition to showing the phenotype in cancer-derived cells, we used siRNA knock-down of MYC and MAPK inhibitor treatments as alternative approaches to validate that depletion of oncogenes and inhibition of their signaling reverses these effects on interferon and ISG expression.

First, knock-down of endogenous MYC in the LHS parental cells (from which EV and MYC are derived) produced 1-2 orders of magnitude increases in transcript levels of IFNβ and a panel ISG (IRF7, OAS2, OAS3, DDX58, STAT1), measured by qPCR (**Supplemental Figure 1.S1**). Thus, depletion of MYC produces the opposite effect of MYC overexpression. These effects also suggest that even normal cellular concentrations of MYC regulate baseline IFNβ and ISG expression. Next, MCF10A cells expressing KRAS oncogene were treated with MEK inhibitor PD0325901 (MEKi). Inhibition of MAPK signaling increased IFNβ transcript levels nearly 10-fold and the associated ISGs became correspondingly up-regulated, validating the effects on

interferon and ISGs identified using MAPK oncogene overexpression models (**Supplemental Figure 1.S1**).

Finally, we directly confirmed that MYC and KRAS oncogenes regulate the interferon and ISG suppression phenotypes in tumor-derived PDAC and OS models using siRNA knock-down of MYC and MEKi treatment. MYC knock-down in KP4 and PSN1 cell lines produced 1-2 orders of magnitude increases in IFNβ and ISG transcript levels. Similarly, MYC knock-down in OS152 and OS186 PDX-derived cell lines caused dramatic up-regulation IFNβ and ISG transcript levels, several induced over three orders of magnitude (**Supplemental Figure 1.S1**). Additionally, KP4 and PSN1 cell lines expressing mutant KRAS were treated with MEKi. Inhibition of MAPK signaling caused 2- to over 20-fold up-regulation of IFNβ and ISG transcript levels (**Supplemental Figure 1.S1).** These isogenic knock-down and pathway inhibition experiments control for genetic complexities between PDAC and OS tumor cells vs. normal cells, clearly demonstrating that expression of MYC and KRAS oncogenes drives the ISG suppression phenotype that was identified using unbiased proteomics.

dsRNA sensing proteins are among the most dysregulated ISGs causing impaired functional response to polyI:C stimulation.

Interestingly, the proteomics data showed more dramatic effects on dsRNA than dsDNA sensing pathway proteins. Proteins that sense cytosolic dsRNA were down-regulated from 2- to over 50-fold. In contrast, the dsDNA sensors or the adaptor proteins MAVS, STING, and TBK1 were either insignificantly or only modestly changed when detected in the proteomics (**Figure 1.2**). The dsRNA sensors DDX58, MDA5, OAS proteins, and EIF2AK2 are well-annotated as ISGs. The dsDNA sensors and adaptor proteins have not been identified as strong ISGs, however one report found that cGAS was induced by T1IFN in macrophages(43). To test if cGAS is

regulated by T1IFN in the cell types used here, the cell lines were treated with 500U/mL IFNβ and the mRNA levels of a panel of well-annotated ISG—OAS2, OAS3, DDX58, and STAT1—and cGAS were quantified by qPCR. In contrast to the orders of magnitude increases in transcription of strong ISGs, cGAS was not regulated by IFNβ in these cell lines, indicating it may be a weaker or cell-type specific ISG (**Supplemental Figure 1.S2**)(40, 42, 44, 45). Therefore, consistent with the global suppression of ISGs, we hypothesized that a deactivated T1IFN state in tumor cells exerts greater impact on T1IFN-regulated dsRNA sensors than other pathway elements with weaker or absent ISRE.

Based on the significantly reduced protein levels of dsRNA sensors but similar levels of dsDNA sensors, we predicted that there would be distinct functional consequences to the dsRNA sensing compared to the dsDNA sensing signaling pathways for cells expressing oncogenes. The dsRNA and dsDNA sensing cascades that regulate production of T1IFN converge downstream of MAVS and STING at the phosphorylation at Ser172 of TBK1. Therefore, we measured activation of TBK1 in response to dsRNA or dsDNA ligands to determine the relative nucleic acid sensor function between cells expressing oncogenes and EV. To assess dsRNA sensing, cells were stimulated with the dsRNA mimetic polyinosinic-polycytidylic acid (polyI:C). Low molecular weight polyI:C was chosen as it is the optimal length for DDX58 activation, however MDA5 requires longer dsRNA ligands(46). To evaluate dsDNA sensing, cells were treated with dsDNA from salmon that was purchased pre-sheared to average 1000bp, within the length range for optimal cGAS activation(47). STING protein levels were comparable in the MCFF10A signal transduction oncogene models but below mass spectrometry detection limits in LHS and P493-6 cells, so in addition cells were treated with 2'3'-cyclic GMP-AMP (cGAMP), the cyclic dinucleotide activator of STING synthesized by cGAS, to directly examine STING function(48).

Cells expressing MYC, KRAS, and AKT oncogenes (selected to represent the 3 major oncogenic axes) and EV were stimulated with transfection agent alone or transfection agent complexed with polyI:C, dsDNA, or cGAMP, and the phosphorylation of TBK1 was quantified by immunoblot. Mass spectrometry data and immunoblots showed equivalent levels of total TBK1 indicating no change in protein expression (**Supplemental Figure 1.S3**). For the transfection agent control, there were similar levels of baseline phosphorylation of TBK1 for the MCF10A cells expressing EV, KRAS, and AKT, however substantial hypo-phosphorylation of TBK1 for LHS cells overexpressing MYC compared to EV (53% of EV levels) (**Figure 1.2, Supplemental Figure 1.S3**). When stimulated with polyI:C, cells expressing oncogenes had significantly reduced TBK1 activation when normalized to the level for EV (approximately 29%, 70%, and 57% of EV level for LHS MYC, MCF10A KRAS, and MCF10A AKT respectively) (**Figure 1.2, Supplemental Figure 1.S3**). In contrast, the cells expressing KRAS and AKT produced similar or increased levels of phospho-TBK1 compared to MCF10A EV when treated with dsDNA and cGAMP (**Figure 1.2, Supplemental Figure 1.S3**). The LHS MYC cells had reduced levels of phospho-TBK1 compared to LHS EV when stimulated with dsDNA and cGAMP (76% and 58% of EV levels respectively), however these differences were not as dramatic as the larger effect produced by polyI:C treatment, and likely residual of the hypo-phosphorylation observed at baseline (**Figure 1.3, Supplemental Figure 1.S2**). The desensitization to polyI:C stimulation demonstrated for MYC, KRAS, and AKT oncogenes implicated dysfunction in dsRNA sensing upstream of TBK1 that was consistent with the proteomics results.

Based on the impaired activation of TBK1 with dsRNA stimulation, we expected that downstream activation of T1IFN transcription would be correspondingly diminished in cells expressing driver oncogenes compared to EV. To evaluate this functional effect, all eight isogenic

oncogene models were stimulated with polyI:C and the transcriptional activation of T1IFN was quantified by qPCR using pan-IFNα and IFNβ primers. T1IFN induction was calculated as the fold-change in transcript levels for transfection agent alone treatment vs. transfection agent complexed with polyI:C treatment. To evaluate the relative dsRNA sensing responses for cells expressing oncogenes vs. EV, we normalized the fold-change value for cells expressing oncogenes to the fold-change value for the corresponding EV control (**Figure 1.2, Supplemental Figure 1.S3**). When compared to non-oncogene controls, P493-6 and LHS cells overexpressing MYC had 4- to 15-fold decreased induction of T1IFN when treated with polyI:C (**Figure 1.2, Supplemental Figure 1.S3**). MCF10A cells expressing signal transduction oncogenes were similarly desensitized to polyI:C when compared to MCF10A EV, exhibiting 10- to over 100-fold reduced transcriptional activation (**Figure 1.2, Supplemental Figure 1.S3**). Compared to MCF10A EV, cells expressing AKT oncogene showed dramatically reduced IFNβ induction, however the induction of IFNα was not statistically different (**Figure 1.2, Supplemental Figure 1.S3)**. This result might reflect compounded noise from measuring 13 IFNαs collectively. The 10-fold decrease in IFNβ induction was the dominating effect, and supports the observation that cells expressing signal transduction oncogenes have dysfunctional responses to polyI:C. Overall, cells expressing oncogenes had reduced phosphorylation of TBK1 and attenuated induction of T1IFNs when stimulated with polyI:C. Furthermore, this significant result was demonstrated using a ligand that predominantly activates DDX58, and we predict even greater desensitization to dsRNA when the full effect of other suppressed dsRNA sensors like MDA5 are measured.

Next, we evaluated a second dsRNA sensing pathway, the OAS-RNASEL system, that is regulated by the dsRNA sensors OAS1, OAS2, and OAS3. As described, OAS proteins are strongly regulated by T1IFN and are up to two orders of magnitude suppressed in the proteomics

data. We hypothesized that polyI:C stimulation would result in low activation of the OAS-RNASEL system in cells expressing oncogenes due to reduced baseline and interferon-induced OAS protein expression. To quantify RNASEL activation, cells expressing oncogenes and non-oncogene controls were treated with polyI:C, cellular RNA was extracted, and the extent of RNASEL-driven RNA cleavage was analyzed by capillary electrophoresis. A representative RNA fragmentation trace for the LHS model is shown in **Figure 1.2**. Both unstimulated LHS EV and LHS MYC cells had intact RNA as seen by the two dominant rRNA bands matching 18S and 28S subunits, and the corresponding RNA-integrity values (RIN^e) were the maximum, 10. When stimulated with polyI:C, the RNA banding pattern for LHS EV visually became more fragmented than that of the LHS MYC cells. This was quantified by the lower RIN^e number of 5.6 for LHS EV cells compared to 9.1 for LHS MYC cells. The increased RNA degradation in non-oncogene cells suggested efficient activation of the OAS/RNASEL pathway, whereas cells overexpressing MYC failed to elicit the equivalent response. Similarly, ΔRIN^e [Oncogene-EV] calculations for each oncogene vs. EV are summarized in **Figure 1.2** (RIN^e values reported in **Supplemental Figure 1.S3**) and indicated reduced activation of RNASEL in cells expressing oncogenes compared to respective EV cells.

Down-regulated ISG expression is due to diminished production of T1IFN.

T1IFN produced by cells is important for autocrine regulation of ISGs(39, 40, 49). The global basal suppression of ISGs indicated possible dysregulation of T1IFN expression and autocrine signaling. To test if secreted IFNβ could have this effect, LHS and MCF10A cells expressing EV were treated with an antibody to neutralize IFNβ activity (anti-hIFNβ) or vehicle (PBS) and transcription of a representative set of ISG was profiled by qPCR. Repression of OAS2, OAS3, DDX58, and STAT1 were recapitulated by IFNβ antibody blockade (**Figure 1.3**). In a

second approach, LHS EV cells were treated with the specific TBK1 inhibitor GSK8612 or vehicle (DMSO) to block baseline cellular production of IFNβ. Whole cell proteomics of vehicle compared to GSK8612 treatment determined that inhibition of endogenous TBK1 phenocopied the ISG perturbations of oncogenic cells (**Figure 1.3**) ProteomeXchange with identifier PXD033373). In particular, dsRNA sensor DDX58 as well as other strong ISGs such as MX1 and IFIT3 were down-regulated 3.1-, 74.6-, and 8.2-fold, respectively, at the TBK1 inhibitor concentration tested (**Figure 1.3**).

We next profiled endogenous levels of T1IFN to further examine the dysregulation of T1IFN expression and autocrine signaling. However, baseline cellular and secreted T1IFN levels for oncogene and non-oncogene LHS and MCF10A cell lines were too low to be quantified in cell lysates or conditioned media by commercial ELISA kits. Though baseline T1IFN concentrations could not be determined, treatment with exogenous hIFNβ rescued ISG expression in oncogenic cells. Oncogene and non-oncogene cells were treated with 500U/mL hIFNβ or vehicle (PBS) and transcriptional activation of OAS2, OAS3, DDX58, and STAT1 was quantified by qPCR. ISG induction was determined by calculating the transcript fold-change between hIFNβ and PBS treatments (**Figure 1.3**). ISG fold-changes between hIFNβ and PBS treatment were approximately the same for MCF10A cells expressing signal transduction oncogenes or EV (**Figure 1.3**). LHS and P493-6 cells overexpressing MYC seemingly produced even higher ISG transcriptional responses than non-oncogene controls (**Figure 1.3C**). However, in a second analysis of the same data, the transcript levels for LHS and P493-6 models were normalized to the value of PBS-treated non-oncogene cells (**Supplemental Figure 1.S4**). This demonstrated that the apparent increase in ISG transcription in oncogene cells was likely the combined effect of two to three orders of

magnitude reduced transcript levels at baseline, and a maximum threshold of IFN and ISG activation before triggering well-described negative feedback pathways(50, 51).

While whole-cell proteomics did not detect T1IFN receptor subunits, previous extracellular-enriched surface proteomics performed on these cell lines identified that IFNAR1 and IFNAR2 expression were generally unchanged in MCF10A isogenic models(17). Despite suppression of interferon-regulated components of the ISGF3 complex, cells expressing oncogenes were poised to re-activate ISG transcription in response to exogenous T1IFN. These results indicated that impaired T1IFN production perpetuates the suppressed antiviral phenotype, while the autocrine/paracrine response arm remains functional.

Finally, the functional rescue by exogenous interferon was tested. Cells expressing MYC, KRAS, and AKT oncogenes were pre-treated with either 500U/mL hIFNβ or PBS and subsequently stimulated with polyI:C. The fold-change in IFNβ transcript levels between transfection agent alone and transfection agent complexed with polyI:C treatment were calculated, and values for interferon pre-treated cells were normalized to those of the corresponding PBS controls (**Figure 1.3**). Pre-treating cells expressing oncogenes with interferon rescued the response to polyI:C 3- to 10-fold. Taken together, the phenotyping, autocrine assays, and functional rescue experiments indicated that decreased interferon production prevents autocrine stimulation of antiviral response pathways causing reduced dsRNA sensing in oncogenic cells.

Cells overexpressing oncogenes are more susceptible to SARS-CoV-2 infection.

The systematic suppression of T1IFN and antiviral defenses by oncogenes has clinical implications, including potential selective susceptibility to oncolytic and gene-therapy viruses. The cumulative impact of reduced T1IFN levels, low ISG expression, and disarmed RNA sensing was

interrogated by infecting cells with an RNA virus. We used SARS-CoV-2 because it is a positive-strand RNA virus that generates dsRNA replication intermediates(52). LHS cells overexpressing EV or MYC and MCF10A cells expressing EV and AKT oncogenes were acutely infected with SARS-CoV-2 for one hour. After infection, virus was washed out, media replaced, and cells were incubated for 24 hours to permit viral replication in cells. Cellular RNA was harvested and viral genome titers were determined by qPCR amplification of viral N (vN) and E (vE) genes (relative to cellular GUSβ). Cells expressing MYC and AKT oncogenes fostered 10- to 20-fold higher viral genome loads compared to respective EV cells treated at equal MOI (**Figure 1.4**). ACE2 and TMPRSS2 are the host receptor and protease that mediate SARS-CoV-2 cellular entry. We immunoblotted these protein levels in LHS EV and MYC cells and MCF10A EV and AKT cells. LHS MYC cells had small increases (less than two-fold) in ACE2 and TMPRSS2 levels compared to EV cells and MCF10A AKT cells had similar or decreased expression of ACE2 and TMPRSS2 compared to EV cells, indicating that expression levels of these proteins are not likely causing the dramatic increases in viral titers (**Supplemental Figure 1.S5**)(53).

To further demonstrate that deactivated antiviral defenses cause increased viral infection (and not ACE2/TMPRSS2 levels or other oncogene effects on biosynthetic or anti-apoptotic pathways), two rescue experiments were performed. In the first experiment, cells were pre-treated with 500U/mL hIFNβ for 16 hours. IFNβ pre-treatment of cells expressing MYC and AKT oncogenes decreased viral titers to non-oncogene EV levels, validating that low baseline T1IFN and corresponding ISG expression specifically cause increased viral infection (**Figure 1.4**). Priming LHS and MCF10A EV with IFNβ did not provide additional defense against viral load (**Figure 1.4**, **Supplemental Figure 1.S5**). This is possibly due to already very low levels of infection at baseline because of functional antiviral pathways in non-oncogene cells.

In a second rescue experiment, the isolated contribution of OAS-RNASEL system was assessed. Several reports indicate SARS-CoV-2 is sensitive to OAS-RNASEL antiviral defenses, including genome-wide association studies implicating the OAS gene cluster in critically ill patients (52, 54, 55). To determine the consequence of low OAS protein expression, oncogenic cell lines were engineered to stably overexpress OAS2 (pOAS2) or empty plasmid (p0) (**Supplemental Figure 1.S5**). While OAS3 is the primary activator of RNASEL during most viral infections, oncogenic cells failed to express ectopic OAS3 at levels that could be validated by immunoblot (41, 56). Alternatively, we could engineer high levels of OAS2 expression, and when OAS2 is overexpressed there is high activation of RNASEL(41, 57). In cells expressing MYC and AKT oncogenes, OAS2 knock-in partially attenuated (approximately 50%) the viral titers compared to empty plasmid control cell lines (**Figure 1.4**).

Individually, IFNβ pre-treatment or OAS2 re-expression could specifically protect cells expressing MYC and AKT oncogenes from viral infection, suggesting oncogene-driven suppression of antiviral defense pathways increases viral susceptibility. Additionally, one consideration is that SARS-CoV-2 encodes multiple viral proteins that block host activation of T1IFNs(58). Based on impaired activation of T1IFN production we characterized for cells expressing oncogenes, we hypothesize that there could be even more dramatic tumor cell selectivity for RNA viruses that do not evade the host interferon response.

1.4 Discussion

The isogenic cell line studies here represent a reductionist approach to understanding the impact of well-known driver oncogenes when expressed in immortalized cells. While this over-simplifies oncogenic transformation, these systematic experiments identify molecular and

functional changes that are directly regulated by oncogenes and build fundamental understanding that can be applied to diverse and mutationally complex tumors. We confirmed these findings in relevant PDAC and OS tumor- and PDX-derived cell lines.

We utilized unbiased proteomics to evaluate the molecular changes associated with different driver oncogenes and to identify potential phenotypic convergence with relevance to cancer biology or therapeutic strategies. Overall, expression of each oncogene caused large up- and down-perturbations in proteomes, and there was a mixture of uniquely and commonly dysregulated proteins. For the MYC oncogene expressed in B-cell, prostate, and OS models, the distinct regulation highlights dependency on cellular context. The unique set of changes generated by each signal transduction oncogene likely reflects differences in wiring and feedback loops as has previously been observed for the components in the MAPK pathway(32, 33). Despite differences at the individual target level, there was increased overlap when analyzed by gene-set analysis that groups proteins by their functional classes. Previous cell surface proteomics studies using these cell lines similarly characterized bi-directional remodeling and a mixture of unique and common proteins that harmonized when viewed by gene-set analysis(17, 18).

The most remarkable finding was that oncogenes from distinct signaling axes (MYC, HER2/EGFR, KRAS/BRAF/MEK, and AKT) suppress T1IFN autocrine signaling, which strongly reduces ISG and dsRNA sensor expression. It is interesting that though the endogenous levels of IFNβ are below detection levels by ELISA, it is clearly operating in the normal cells because neutralizing antibodies to it suppress ISG transcription, and addition of IFNβ to oncogene cells restored the antiviral expression. This likely reflects the extreme sensitivity of autocrine signaling. The numerous antitumor functions of T1IFN and antiviral effectors are well-known, and immune evasion is a hallmark of cancer(59–63). Others have found dysregulation of T1IFN and antiviral

pathways in a number of advanced and genetically complex cancers, supporting the breadth of the phenotype and its persistence in paracrine tumor microenvironments(59, 60, 64–68). Here we expand this understanding by isolating the role of driver oncogenes from other complex mutational lesions and specific cellular contexts and show each oncogene can directly suppress T1IFN and antiviral dsRNA pathways. Further, the interferon suppression signature was the most significant common effect identified using an unbiased and integrative proteomics approach for six signal transduction oncogenes and MYC. These findings emphasize that these pathways may be fundamental in tumor development and immune evasion hallmarks, and support the generality that over-activation of growth and proliferation signaling is immunosuppressive.

The proteomics results indicated that suppression of T1IFN in cells expressing oncogenes has a significant impact on T1IFN-regulated dsRNA sensors but not dsDNA sensors with weaker or absent ISRE. Tumors often carry defects in dsDNA sensing function, for example through genetic and epigenetic repression of cGAS and STING, as well as various mechanisms modulating cGAMP hydrolysis and trans signaling(69–73). Conversely, STING activation of noncanonical inflammatory pathways has been found to promote epithelial-mesenchymal transition and metastasis in cancers with high chromosomal instability that generate excessive dsDNA in the cytosol(74). It is possible that evasion or activation of dsDNA sensing pathways in tumors is largely shaped by specific tumor contexts, selective pressures, and immune editing that are not captured by reductionist models(48, 69, 70, 75–78). Our work demonstrates that separate from specific tumor or immune selective factors, oncogenes autonomously down-regulate T1IFN expression, causing direct and dramatic consequences to antiviral dsRNA sensors that are strong ISGs.

For each oncogene we systematically interrogated the functional consequences to dsRNA sensing pathways including T1IFN transcription and OAS activation, and the response to interferon. These pathways are critical to several standard cancer therapies. Ionizing radiation, genotoxic drugs, and epigenetic inhibitors require induction of T1IFN and activation of RNASEL to execute cytotoxic and immune activating effects(79–84). Genotoxic stress and DNA demethylation mount the dsRNA sensor response through up-regulated transcription of repetitive, noncoding, and retrotransposon elements that have double-stranded RNA secondary structures(85–87). In several studies, cells deficient in MAVS, DDX58, OAS proteins, or RNASEL had decreased responses to radiation and epigenetic treatments(80–83, 87–89). We demonstrated that prominent oncogenes down-regulate DDX58, MDA5, and OAS proteins, robustly deactivating dsRNA sensing pathways, which could limit the therapeutic index of radiation, genotoxic, and epigenetic agents. Indeed, the ISG gene signature stratifies radio-resistance in breast cancer and is regarded as a radiation-induced biomarker (90). Our discovery that exogenous IFNβ rescued ISG expression in oncogenic models suggests that co-treatment of ionizing radiation, genotoxic drugs and epigenetic inhibitors with T1IFN could re-sensitize these pathways for broader therapeutic reach. Several studies have reported increased efficacy using combination treatments with interferon(91–93). However, researchers have found that one mechanism of acquired radio-resistance is selection for insensitivity to interferon. Interestingly, resistant cells fail to transmit interferon signaling but depend on the constitutive expression of unphosphorylated STAT1, which they showed to be a response to chronic interferon stimulation during radiation(94, 95).

Evasion of immune surveillance is a signature of many cancers, and checkpoint inhibitors and adoptive cell therapies are strategies to promote immune cell infiltration(1, 2, 96). T-cell

recruitment requires antigen-presentation on MHC complexes, which are regulated by interferon. Tumors with low MHC or interferon expression are resistant to these therapies and a genetic screen specifically identified HLA-A, B2M, TAPBP, TAP1, TAP2, and STAT1 as essential genes for immunotherapy response(97–99). These are ISGs that were significantly down-regulated by oncogenes in our proteomics. These are important considerations for therapies that rely on native immune cell recruitment, which other investigators have shown become more effective when co-treated with interferon(100, 101). CAR-T are engineered to recognize up-regulated surface proteins and could be advantageous for targeting tumor cells that might down-regulate MHC complexes through repressed interferon.

We found that cells expressing oncogenes have increased viral vulnerability. While our experiments tested SARS-CoV-2 as proof-of-concept, the selective viral susceptibility of tumor cells could be relevant to oncolytic and gene-therapy viruses. There has been extensive research and ongoing clinical trials for viral-based cancer therapeutics that exploit tumor-intrinsic pro-proliferation and anti-apoptosis pathways and immune-privileged microenvironments(102–104). Other researchers have demonstrated the efficacy of virally targeting tumors with specific defects that down-regulate innate immune signaling, and studies using the proviral drug sunitinib implicated that inhibition of OAS-RNASEL and EIF2AK2 enhances efficacy of oncolytic virus(66, 105–109). Our experiments showed that dramatic desensitization of dsRNA sensing pathways and increased susceptibility to RNA viral infection are general effects of oncogenes that could be broadly leveraged using virotherapy. Further, our functional discoveries would suggest that a virus that does not encode proteins to evade host antiviral and interferon response pathways could be highly tumor-selective by exploiting attenuated T1IFN production in tumor cells compared to healthy tissues(110, 111).

It is significant that seven driver oncogenes suppress interferon and harmonize at phenotypic and functional levels. PDAC and OS are two highly lethal diseases, and for many other cancers low interferon and ISG expression is also indicative of aggressive and drug-resistant subtypes(10, 13, 14, 59, 60, 64, 79). We hope these molecular and functional studies help inspire therapeutic development for these currently undruggable and refractory cancers.

Acknowledgements:

We valued helpful discussions with Dr. Robert Silverman at Cleveland Clinic, Dr. George Stark at Cleveland Clinic, Dr. Davide Ruggero at UCSF, and Dr. Bruno Amati at European Institute of Oncology. We thank Jamie Byrnes, Cole Bracken, and members of the laboratory of J.A.W. for helpful discussions and support. J.A.W. was supported by generous funding from the Chan Zuckerberg Biohub Investigator Program, the Harry and Dianna Hind Professorship, NIH R35GM122451, and NCI R01CA248323. J.J.C. was supported by generous funding from NIH P41GM108538. O.S.R. was supported by generous funding from LGR ERA award, Chan Zuckerberg Biohub Investigator Program, and NIAID R01AI128214. E.A.S.C. and L.C.S. were generously funded in part by Battle Osteosarcoma and the St Baldrick's Foundation.

1.5 Materials and Methods

Generating PDX cell lines

PDX tumors were grown in NSG mice. Once large tumors formed, they were resected and minced with a razor blade and digested to make a single-cell suspension using either collagenase digestion buffer or BD tumor dissociation reagent (BD Biosciences Cat# 661563) shaking at 37ºC for 1hr. Cells were filtered through 70µm mesh and washed twice in DMEM/F12 (Gibco Cat

#21331020) supplemented with 10% FBS (Gibco) and 1% PSG (Gibco Cat# 10378016). Cells were plated in standard tissue culture conditions and allowed to expand. After several weeks, human cells were isolated from mouse stroma by FACS using human HLA-A,B,C antibody (BioLegend Cat# 11414). Cells were allowed to expand for several weeks and sorted a second time to generate a pure population. Cell lines were submitted for STR (IDEXX bioanalytics) and determined to match the PDX from which they were derived and were confirmed mycoplasma free. Cell lines were also submitted for low pass WGS to confirm that they match the patient from which they were derived and PDX.

Culturing cell lines

P493-6 cell lines were cultured in RPMI media (Cytiva, Cat# SH30027.01) with 10% tetracycline-negative fetal bovine serum (FBS) (Gemini Bio-Products, Cat# 100-108) and 1% penicillin/streptomycin (Thermo Fisher Scientific, Cat# 15-140-122). MYC expression was repressed in P493-6 cells by treatment with 1μg/mL tetracycline (Sigma Aldrich, Cat# T7660-25G) for 48 hr before downstream analyses. LHS cell lines were cultured in RPMI media with 10% FBS (Gemini Bio-Products, Cat# 100-106) and 1% penicillin/streptomycin. MCF10A cell lines were cultured in DMEM media (Cytiva, Cat# SH30022.01) with 5% horse serum (Gemini Bio-Products, Cat# 999-999 custom sera), 1% penicillin/streptomycin, 20ng/mL EGF (Thermo Fisher Scientific, Cat# PHG0311), 0.5mg/mL hydrocortisone, 100ng/mL cholera toxin (Sigma Aldrich, Cat# C8052-2MG), and 10μg/mL insulin (Sigma Aldrich, I0516-5ML). PDX cell lines and hFOB were culture in DMEM media with 10% bovine growth serum (BGS) and 1% penicillin/streptomycin. PDAC cell lines were cultured in IMDM media (UCSF Cell Culture Facility) with 10% FBS and 1% penicillin/streptomycin. HPDE-6E6/E7 cells were cultured in

Keratinocyte SFM (Thermo Scientific, Cat# 17005042) with 25mg of bovine pituitary extract (BPE) and 2.5μg of EGF. All cells were maintained at 37ºC and 5% CO_2.

Whole cell label-free proteomics

LHS, P493-6, OS, PDAC, and GSK8612 treatment

Cell lines were analyzed in biological triplicate. Cell pellets were washed in PBS and resuspended in pre-heated lysis buffer (filtered 50mM TRIS pH 8.5 containing 6M guanidinium hydrocholoride (GdnHCl) (Chem Impex, Cat# 00152), 5mM TCEP (MilliporeSigma, Cat# 5805601GM), and 10mM chloroacetamide (Sigma Aldrich, Cat# C0267-100G)). Samples were boiled at 97ºC for 10 min with interim mixing. Insoluble debris was removed by centrifugation for 10 min at 21,000g, and supernatants were diluted using filtered 50mM TRIS pH 8.5 to achieve a final GdnHCl concentration of 2M. Protein absorbance at 280nm was measured to determine lysate protein concentrations, and 1μg of Trypsin (Thermo Fisher Scientific, Cat# 90057) per 100μg of protein was added. After overnight digestion samples were desalted using C18 columns (Thermo Scientific, Cat# 60109-001 or Thermo Scientific, Cat# 89873). Eluted peptides were lyophilized. Injections of peptides for LC-MS mass spectrometry were prepared by resuspending peptides in 2% acetonitrile (Fisher Scientific, Cat# A955-4) and 0.1% formic acid (Fisher Scientific, Cat# A117-50) solution. 1.5μg of peptide was injected into an UltiMate 3000 UHPLC system (Thermo Fischer Scientific) with a pre-packed Acclaim Pepmap C18 reversed phase column (Thermo Fisher Scientific, Cat# DX164534) attached to a Q Exactive Plus mass spectrometer (Thermo Fisher Scientific). Peptides were separated using a linear gradient of 3-35% solvent B (Solvent A: 0.1% formic acid, solvent B: 80% acetonitrile, 0.1% formic acid) over 230 min at 300μL/min. Data-dependent acquisition mode using a top 20 method was utilized for analysis (dynamic exclusion 35 seconds, selection of peptides charge 2 to 4). Full MS1 spectra were gathered using resolution

of 140,000 (at 200m/z), AGC target of 3e6, maximum injection time of 120ms, and scan range 400-1800m/z). MS2 scans were collected at resolution of 17,500 (at 200m/z) and AGC target of 5e4, maximum injection time of 60ms, collision energy of 27, and isolation window and offset of 1.5 and 0.5m/z respectively. MaxQuant (Version 1.6.7) software was used to analyze chromatograms, to search Uniprot Human Reference Proteome spectral library (downloaded July 2019; 219758 entries searched in database), and to perform label-free quantitation(19). Peptides were searched using full-tryptic cleavage constraints with maximum 2 missed or non-specific cleavages. Searches were performed with precursor mass tolerance of 20 ppm and product ion mass tolerance of 0.5 Da. Cysteine carbamidomethyl was set as a fixed modification; N-terminal acetylation, methionine oxidation and N-terminal glutamate to pyroglutamate were set as variable modifications. Search results were filtered to a false discovery of 1% at both the peptide and proteins levels. The mass spectrometry proteomics data have been deposited to the ProteomeXchange Consortium via the PRIDE partner repository with the dataset identifier PXD033373(20).

MCF10A proteomics

Cell lines were analyzed in biological triplicate. $20x10^6$ cells were suspended in 200µL 6 M guanidine HCl and boiled for 5 min at 100 °C. Protein was precipitated by the addition of 1,800µL methanol and pelleted by centrifugation at 12,000g for 5 min. Pelleted protein was resuspended in lysis buffer (8M urea, 40mM 2-chloroacetamide, 10mM tris(2-carboxyethyl)phosphine, 100mM tris pH 8) and incubated for 10 min at RT before diluting to [urea] < 2M with 50 mM tris. Trypsin was added at a protein:enzyme ratio of 100:1 and incubated overnight at RT with gentle rocking. After digesting overnight, the solution was adjusted to pH < 2 and desalted with StrataX reverse phase SPE cartridge (Phenomenex, Torrence, CA). Eluted

peptides were dried under reduced pressure and quantified by bicinchoninic acid assay (PierceTM Quantitative Colorometric Peptide Assay, Thermo Fisher Scientific, Waltham, MA). Peptides were reconstituted in 0.2% formic acid to a concentration of 1μg/μL and a 2μL injection was separated over a 90 min nano-liquid chromatography method using a nanoAcquity UPLC (Waters, Milford, MA). Eluting peptides were analyzed a Q-LTQ-OT tribrid mass spectrometer (Orbitrap Fusion Lumos, Thermo Scientific, San Jose, CA) following positive mode electrospray ionization. MS1 survey scans were performed in the orbitrap (240K resolution, AGC target – 1e6, 100 ms max injection time). Tandem mass spectra of HCD-generated (25% NCE) product ions were performed in the ion trap (rapid resolution, AGC target – 4e4, 18 ms maximum injection time). Monoisotopic precursor selection and dynamic exclusion (15 s) were enabled. Thermo RAW files were searched against the Uniprot Human Reference Proteome spectral library (downloaded February, 2018; 93,798 forward sequences searched in database) with the MaxQuant (Version 1.6.0.13) quantitative software suite(19). Peptides were searched using full-tryptic cleavage constraints with maximum 2 missed or non-specific cleavages. Searches were performed with precursor mass tolerance of 50 ppm and product ion mass tolerance of 0.2 Da. Carbamidomethylation of cysteines was imposed as a fixed modification and oxidation of methionines as a variable modification. 'Match between runs' and 'label free quantification' were enabled with a match time window of 0.7 min and minimum ratio count of 1. Search results were filtered to a false discovery of 1% at both the peptide and proteins levels. The mass spectrometry proteomics data have been deposited to the ProteomeXchange Consortium via the PRIDE partner repository with the dataset identifier PXD033373(20).

Experimental Design and Statistical Rationale

Discovery proteomics for each oncogene model were analyzed in biological triplicates. MaxQuant parameters and FDR filters for peptide searches are detailed in proteomics methods above.

MaxQuant LFQ intensities were imported into Perseus v1.6.7.0 for processing and statistical analysis using standard procedures(21–23). First, technical replicates were grouped into biological replicates and the oncogene vs. non-oncogene conditions were annotated. Data were filtered for contaminants, processed for razor+unique peptides (x>1), and filtered for valid values in 60-70% of technical replicates of least one experimental condition. Missing data were imputed using a normal distribution. Technical replicates were collapsed into biological replicates by computing the mean LFQ value. We proceeded with statistical analysis of the three biological replicates using permutation based FDR t-tests (250 repetitions) to account for multiple-hypothesis testing (P493-6, LHS, PDAC, OS models) or using t-tests with Bonferroni adjustments to correct for multiple hypothesis testing (MCF10A models). Thresholds for up- and down-regulated proteins were $p \leq 0.05$ and $\log_2 FC \geq |1|$. Gene-set enrichment was performed using REACTOME bioinformatics tools(24).

Cellular treatments: Nucleic acid, cGAMP, anti-hIFNβ, hIFNβ, GSK8612, MEKi

24 hr before treatments, cells were counted and plated at equal densities.

For nucleic acid and cGAMP stimulation experiments, cells were plated and transfections were carried out in reduced-serum Opti-MEM media (UCSF Cell Culture Facility). PolyI:C (Invivogen, Cat# tlrl-picw), dsDNA harvested from salmon (Thermo Fisher Scientific, Cat# 15632011) or cGAMP (ApexBio, Cat# B8362) were transfected using PEI (Polyplus-transfection,

Cat# 115-010) at a 4:1 PEI:nucleic acid ratio. For phospho-TBK1 immunoblotting, cells were transfected with 0.5μg/mL polyI:C, 0.5μg/mL dsDNA, 1μM cGAMP, or PEI transfection agent alone for 4 hr. For T1IFN transcriptional activation experiments, cells were transfected with polyI:C (0.1μg/mL nucleic acid for P493-6 and LHS or 0.5μg/mL nucleic acid for MCF10A) or PEI transfection reagent alone for 4 hr. For RNASEL rRNA fragmentation analyses cells were treated with 0.5μg/mL polyI:C or PEI transfection reagent alone for 4 hr.

To establish an IFNβ antibody blockade, LHS EV and MCF10 EV cells were treated with 4μg/mL anti-hIFNβ (Invivogen, Cat# mabg2-hifnb-3) or PBS for 16 hr at 37ºC. For the IFN-response assay and SARS-CoV-2 pre-treatment rescue experiment, cells were treated with 500U/mL hIFNβ (Stemcell Technologies, Cat# 78113.1) or PBS for 16 hr at 37ºC.

To inhibit TBK1, LHS EV cells were dosed with 50μM GSK8612 (MedKoo, Cat# 555464) or DMSO and proteomic perturbations were determined after 48 hr at 37ºC.

For MEK inhibitor studies, cells were treated with 2μM PD0325901 (Selleck Chemicals, Cat# S1036) or DMSO vehicle and harvested for RNA extraction or immunoblot after 18 hr.

Cloning and engineering OAS2 overexpression cell lines

OAS2 protein sequence was codon optimized for homo sapiens and purchased as 2 overlapping gene blocks from Twist Biosciences. EF-1a-driven overexpression plasmid pCDH-EF1-FHC was a gift from Richard Wood (Addgene, Cat# 64874) and was used as the lentiviral backbone for transgene delivery(25). pCDH was opened by digestion with NotI (New England Biosciences, Cat# R3189S), and Gibson assembly was used to insert the overlapping gene fragments into the open backbone. Two constructs were created containing either puromycin or

hygromycin resistance cassettes because LHS MYC cells were previously engineered using hygromycin resistance, and MCF10A AKT was engineered using puromycin resistance.

Lentiviral vectors were transfected using Fugene (Promega, Cat# E2311) into HEK293T cells. Cells were maintained at 37ºC for 72 hr to permit viral production. Viral supernatants were filtered and added to plated LHS MYC and MCF10A AKT cells. To increase transduction efficiency, cells treated with lentivirus were centrifuged at 1000g for 3 hr. Cells were subsequently incubated at 37ºC for 24 hr. Then viral transduction solution was washed out with PBS and replaced with fresh media. After an additional 24 hr at 37ºC, cells were treated with 5μg/mL puromycin (Sigma Aldrich, Cat# P9620) or 200μg/mL hygromycin (Thermo Scientific, Cat# 10687010) to select for transgene expression. Media changes continued to be dosed with antibiotics for 2 weeks to select for cells with stable transgene incorporation, at which point knock-ins were validated by OAS2 western blot and qPCR amplification of the transgene transcript.

RNA extraction, cDNA preparation, and qPCR reactions

RNA was extracted and purified using either Qiagen RNeasy (Cat# 74104) or IBI Scientific Tri-isolate RNA Pure kits (Cat# IB47632) according to respective manufacturer guidelines. For qPCR assays, RNA was DNAse-treated and converted to cDNA using Quantitect Reverse-Transcription kit (Qiagen, Cat# 205311) according to manufacturer protocols. qPCR reactions were performed using SYBR Select Master Mix (Thermo Scientific, Cat# 4472908). For most transcripts of interest, primer conditions were 250nM and Tm was 60ºC, however SARS-CoV-2 viral N and E gene transcripts were assayed using 400nM primer and Tm of 58ºC. Primer sequences are reported in **Supplemental Table S1.2** (Integrated DNA Technologies). Fluorescent emissions were detected using Biorad CFX Connect qPCR instrument. Data were analyzed using ΔΔCT method(26).

OAS-RNASEL RNA fragmentation analysis

Total cellular RNA, consisting mostly of rRNA, was prepared with the RNA ScreenTape reagents (Agilent, Cat# 5067-5576, 5067-5577, 5067-5578,) according to manufacturer protocols. Capillary electrophoresis assays were performed and analyzed using the Agilent 4200 TapeStation System and software. The change in RIN^e value between unstimulated and polyI:C transfected conditions was calculated for each cell type. To compare oncogene and non-oncogene cells, this change in RIN^e value was subtracted [Oncogene – EV] and is reported as ΔRIN^e.

Authentic SARS-CoV-2 infection in BSL-3

SARS-CoV-2 from a clinical specimen at UCSF was isolated, propagated and plaqued on Huh7.5.1 cells overexpressing angiotensin-converting enzyme 2 (ACE2) and transmembrane serine protease 2 (TMPRSS2)(27). Viral titers were determined using standard plaque assays(28). All work involving live SARS-CoV-2 was performed in the CDC/USDA-approved Biosafety Level 3 (BSL-3) facility at the University of California, San Francisco in accordance with institutional biosafety requirements.

24 hours prior to SARS-CoV-2 infection, LHS and MCF10A cells were counted and plated in 24-well cell culture plates at equal densities avoiding over-seeding that could disrupt a uniform monolayer. Infection was carried out as previously described(29). Immediately before infection, one well for each cell line was trypsinized to count the number of cells per well. Cells were washed in PBS and infected with SARS-CoV-2 at MOI of 0.1 (LHS cells) or MOI 1.0 (MCF10A cells). After one hour the viral inoculum was removed, cells washed in PBS and 1ml of complete culture media added to each well. Plates were then incubated at 37°C/5% CO2 for 24 hours. After

infection, supernatants were removed and the cells washed twice with PBS before being lysed in TRIzol for total RNA extraction.

Immunoblotting

Cells were lysed with RIPA (Millipore Sigma, Cat# 20-188) containing protease inhibitor (Merck, Cat#11836170001) and phosphatase inhibitor (Sigma Aldrich, Cat# 04906845001). Protein gels were transferred to polyvinylidene difluoride (PVDF) membrane using iBlot 2 instrument and consumables (Thermo Fisher Scientific, Cat# IBI21001, IB24001). Membranes were blocked with 5% BSA for 1 hr, primary antibodies were incubated overnight at 4^{o}C, and appropriate secondary antibodies (LI-COR Biosciences, Cat# 926-32211, 926-68070) were stained for 1 hr at room temperature. Blots were imaged using LI-COR Odyssey CLx scanner and processed using Image Studio Lite. Signal for OAS2 knock-in MCF10A AKT cells was too low to quantify by fluorescence and was instead imaged using HRP chemiluminescence (Cell Signaling Technology, Cat# 7076S and 7074S).

The following antibodies were used at recommended manufacturer dilutions: phospho(Ser172)-TBK1 (Cell Signaling Technology, Cat# 5483T), TBK1(Cell Signaling Technology, Cat# 3504T), ACE2 (Cell Signaling Technology, Cat# 4355T), TMPRSS2 (Invitrogen, Cat# MA5-35756), OAS2 (Thermo Fisher Scientific, Cat# TA802770), MYC (Cell Signaling Technology, Cat# 9402S), and ACTINβ (Cell Signaling Technology, Cat# 3700S, 4970S).

siRNA transfections

For siRNA experiments, negative control siRNA (Thermo Scientific, Cat# AM4611/ Thermo Scientific, Cat# 4390843) or target siRNA (MYC/GAPDH) (Cell Signaling Technology,

Cat# 6341S/Thermo Scientific, Cat# 4390849) were transfected with lipofectamine (Thermo Scientific, L3000-008) per standard protocols (no P3000 reagent was used for RNA transfection). The final concentration was 20nM siRNA, except for OS152 and OS186 cell lines, which were respectively treated with 40nM and 80nM negative control/MYC/GAPDH siRNA. Downstream qPCR analyses were performed 48 hr post-transfection.

1.6 Main Figures

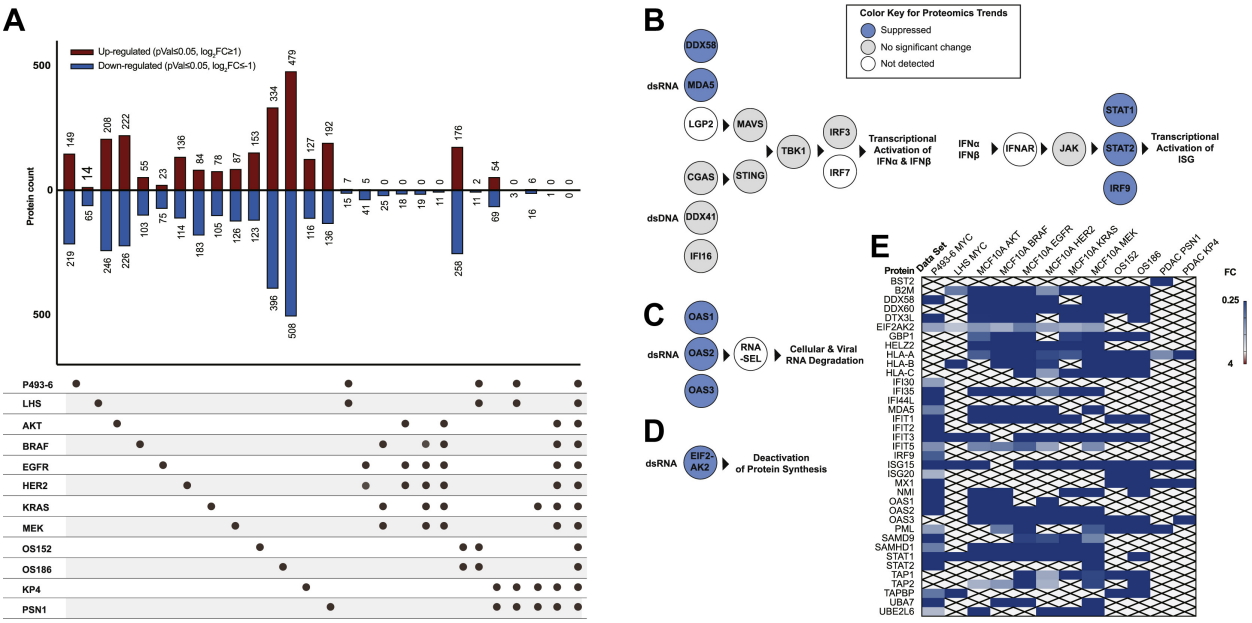

Figure 1.1 Expression of oncogenes causes bidirectional remodeling of cellular proteome and reveals strong down-regulation of IFN-inducible antiviral pathways.

All mass spectrometry data represent three biological replicates for each cell line. T-test significance was corrected for multiple hypothesis testing as described in Methods. A. Upset plot summarizing intersections of proteomics results. Thresholds for up- and down-regulation were $p \leq 0.05$, $log2FC \geq |1|$. B-D. Schema of antiviral pathways are colored to represent general trends in proteomics. Proteins that were suppressed in MYC or signal transduction oncogene models are dark blue, were not dramatically changed in MYC or signal transduction oncogene models are

grey, and were not detected in any data set are white. B. dsRNA and dsDNA sensors drive cascades controlling transcription of IFNα and IFNβ. Secreted IFNα and IFNβ stimulate autocrine and paracrine signaling by binding interferon receptors. This activates JAK/STAT signaling leading to formation of the ISGF3 complex that regulates transcription of hundreds of ISGs. C. dsRNA sensors OAS1-3 catalyze the synthesis of 2'-5' oligoadenylate effectors, ligands to latent RNASEL. Activated RNASEL indiscriminately cleaves cellular and viral RNA. D. dsRNA sensor EIF2AK2 (PKR) deactivates EIF2A to halt protein synthesis. E. Heatmap demonstrating decreased protein expression of over 35 ISGs (with $p \leq 0.05$).

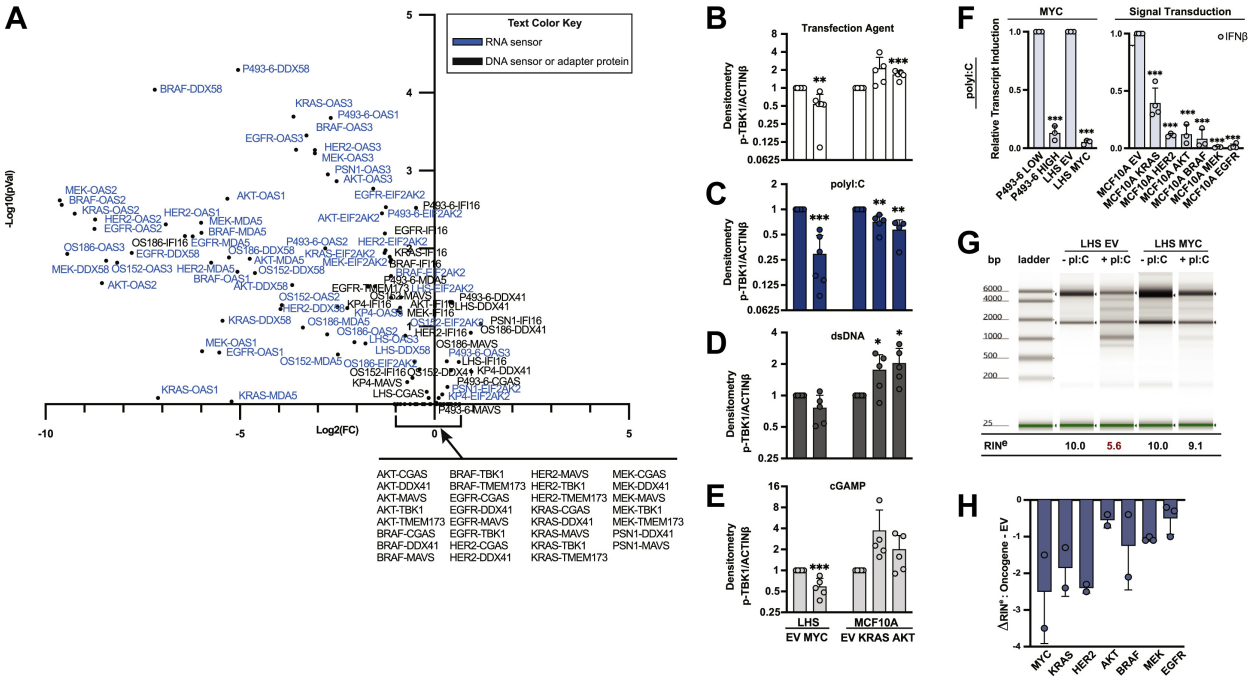

Figure 1.2 Oncogenes disproportionately down-regulate dsRNA sensing compared to dsDNA sensing pathways at proteomic and functional level.

A. Volcano plot depicts dsRNA sensor, dsDNA sensor, and adaptor protein fold-changes and p-values for oncogene vs. non-oncogene cells. Each data point is labelled by the protein and the associated tumor model. dsRNA sensors are labeled in blue text. B-E. Cells with or without oncogenes were treated with transfection agent alone (B) or complexed with polyI:C (C), salmon dsDNA (D), or cGAMP (E). Phosphorylation at Ser172 of TBK1 was immunoblotted. Densities were normalized to the value for respective EV cells for each treatment. Bar graphs represent mean and standard deviation for five biological replicates. Statistics were calculated using Student's t-test between EV and oncogene. F. Cells with or without oncogenes were treated with transfection agent alone or complexed with polyI:C. Transcript level of IFNβ relative to GUSβ reference gene was quantified by qPCR. Extent of IFNβ induction was calculated as the fold-change in IFNβ mRNA between polyI:C treatment and transfection agent alone. Reported data are normalized to

induction value of EV. Bar graphs represent mean and standard deviation of at least three biological replicates. Statistics were calculated using Student's t-test between EV and oncogene. G-H. Cells with or without oncogenes were treated with transfection agent alone or complexed with polyI:C and activation of RNASEL was quantified by capillary electrophoresis. G. Representative capillary electrophoresis experiment for LHS EV/LHS MYC cells. Cleavage of RNA was quantified by RINe values. H. The reported ΔRINe in bar graphs is the difference between RINe (Oncogene) – RINe (EV). Bar graph reports mean and standard deviation of at least two biological replicates. RINe values are tabulated in Supplemental Figure 1.S3.

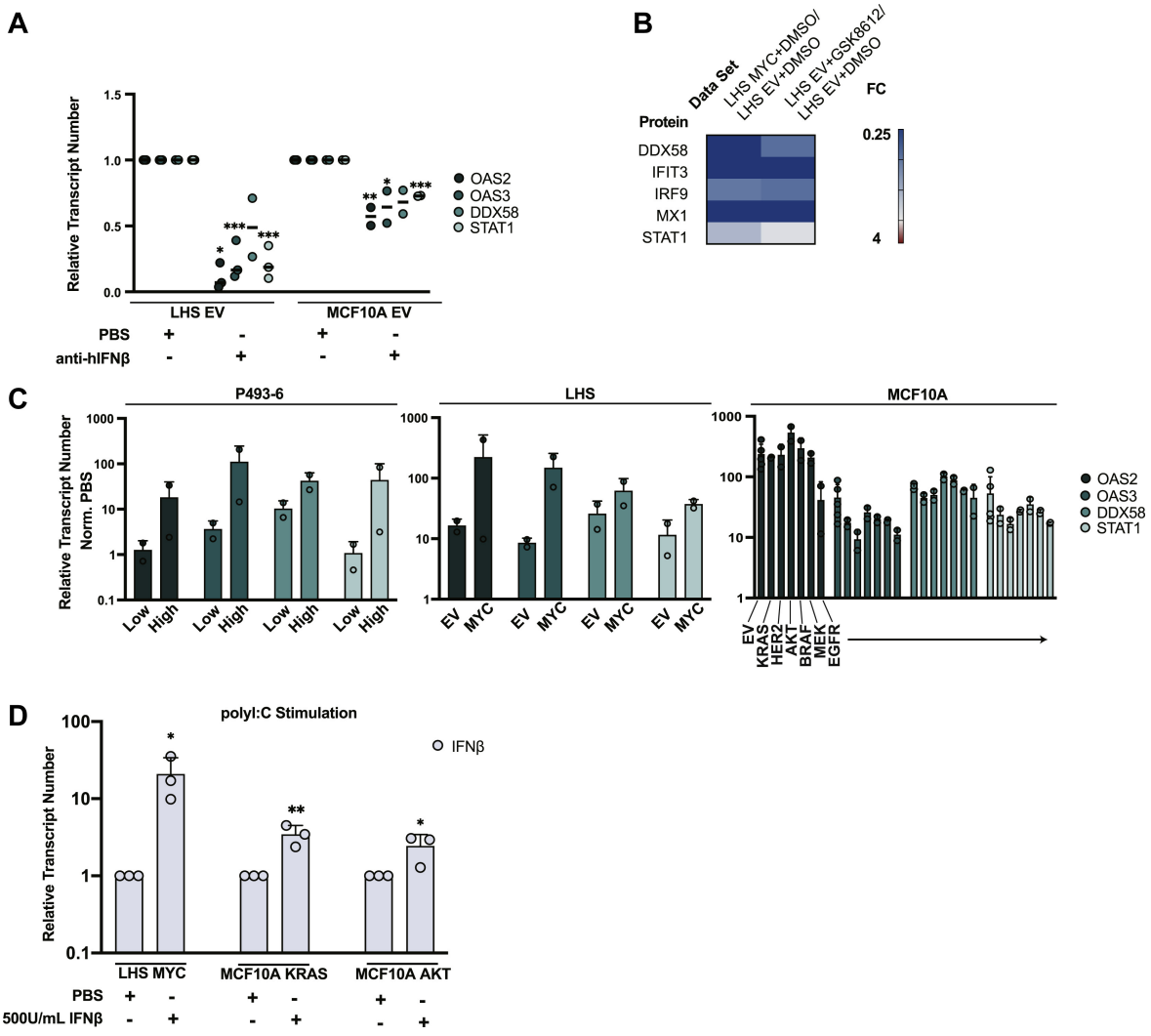

Figure 1.3 Reduced autocrine activity of IFNβ produces a state of low ISG expression.

A. LHS EV and MCF10A EV cells were treated with anti-hIFNβ or PBS. Transcript levels of ISGs relative to GUSβ reference gene were quantified by qPCR. Values were normalized to PBS treatment. Data represent two or three biological replicates. Statistics were calculated using Student's t-test between PBS and anti-hIFNβ treatment. **B.** LHS EV cells were treated with 50μM GSK8612 or vehicle (DMSO) and characterized by label-free proteomics. Heatmap compares fold-change values for a set of ISGs (with $p \leq 0.05$) for (left column) LHS MYC vs. LHS EV and (right column) LHS EV + GSK8612 vs. LHS EV + DMSO. Heatmap represents two biological replicates. **C.** Isogenic oncogene models were stimulated with 500U/mL hIFNβ or PBS. mRNA levels of ISG relative to GUSβ reference gene were quantified by qPCR. Bar graphs summarize fold-change between PBS and IFNβ treatment for each cell line, and report mean and standard deviation of biological duplicates. **D**. Cells expressing MYC, KRAS, and AKT oncogenes were pre-treated with 500U/mL hIFNβ or PBS and subsequently stimulated with transfection agent alone or complexed with polyI:C. Transcript level of IFNβ relative to GUSβ reference gene was quantified by qPCR. Extent of IFNβ induction was calculated as the fold-change in IFNβ mRNA between polyI:C treatment and transfection agent alone, and induction values were normalized to the PBS treatment. Bar graphs represent mean and standard deviation for three biological replicates. Statistics were calculated using Student's t-test between PBS and hIFNβ treatments.

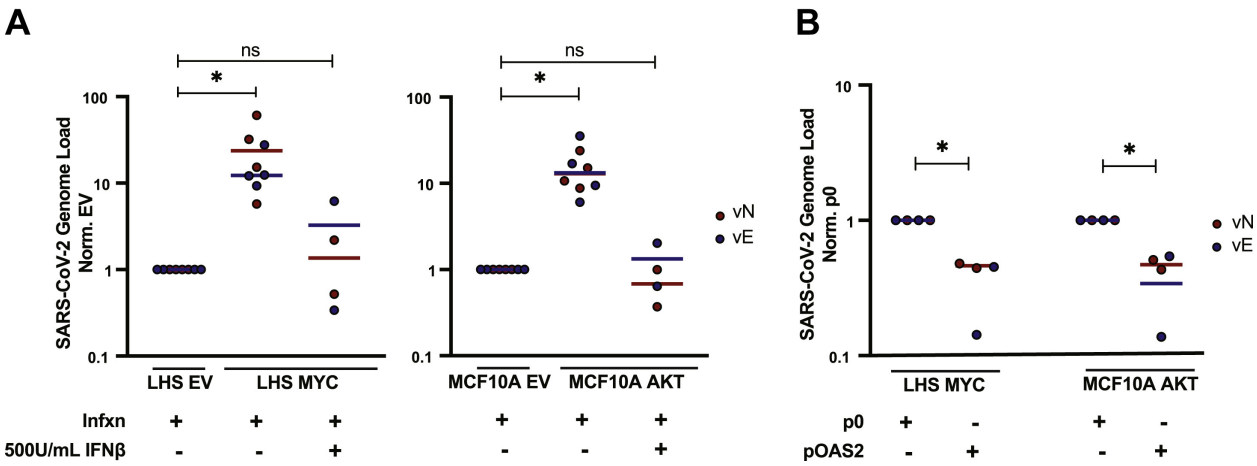

Figure 1.4 Oncogene transformed cells are more easily infected with the RNA virus but become more resistant when primed with IFNβ or engineered to re-express OAS2.

A. LHS EV/LHS MYC cells and MCF10A EV/MCF10A AKT cells with or without 500U/mL IFNβ pre-treatment were infected (infxn) with SARS-CoV-2 (MOI 0.1 and 1.0 for LHS and MCF10A respectively – choice in MOI for each cell type was determined in preliminary experiments in **Supplemental Figure S1.5B**). Cellular RNA was harvested and viral genome load was quantified by qPCR amplification of viral N (vN) and E (vE) genes relative to cellular GUSβ reference gene. Transcript values were normalized to EV value. Data report two to four biological replicates. Statistics were calculated using Student's t-test between EV and oncogene or between EV and oncogene with IFNβ pre-treatment. **B.** LHS MYC and AKT cells were engineered to stably overexpress OAS2 (pOAS2) or empty plasmid (p0). pOAS2 and p0 cells were infected with SARS-CoV-2. Cellular RNA was harvested and viral genome load was quantified. Transcript values were normalized to p0 cell lines. Data represent two biological replicates. Statistics were calculated using Student's t-test between cells expressing p0 and pOAS2.

1.7 Supplemental Figures

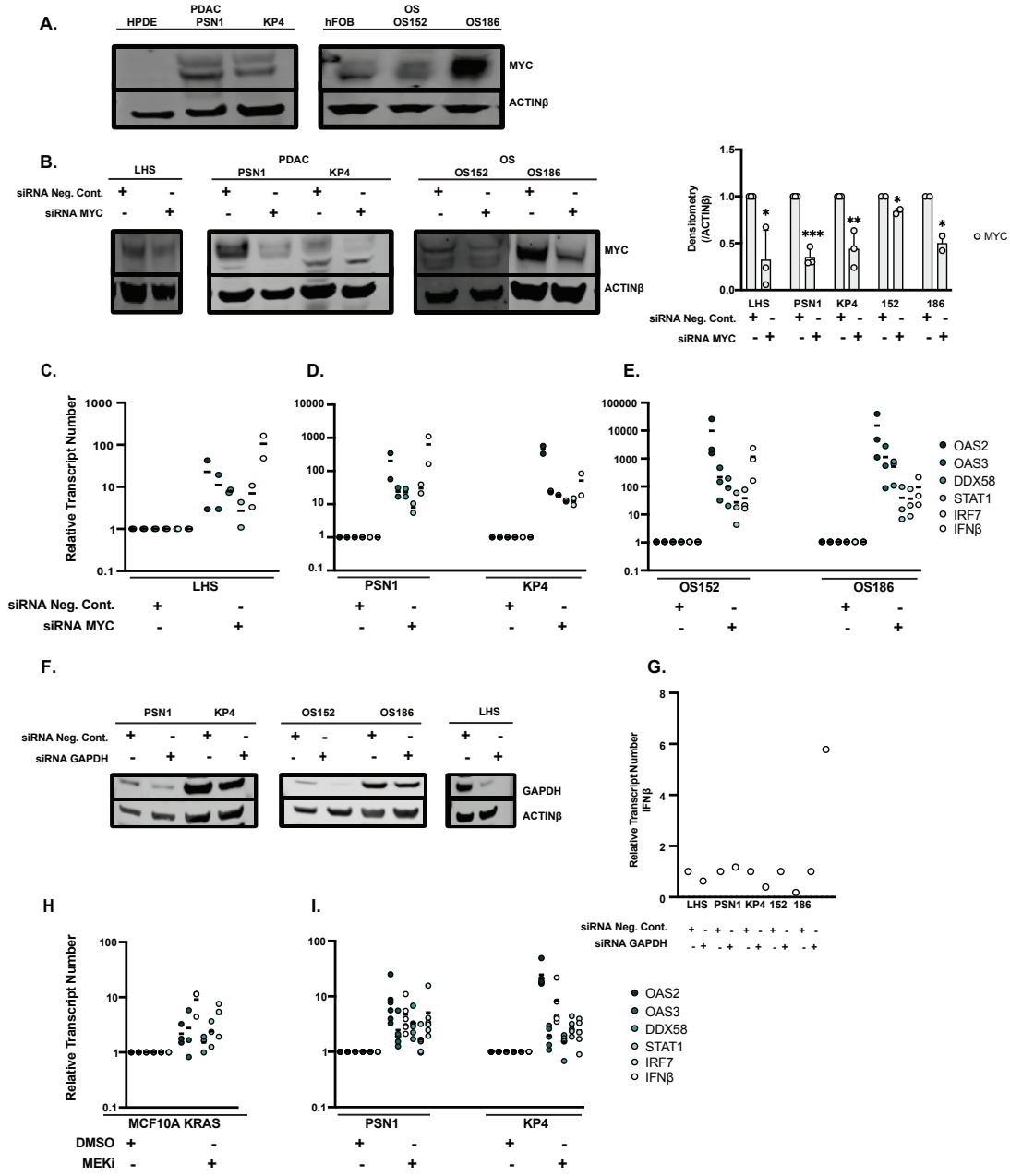

Figure 1.S 1 Knock-down and pathway inhibitors validate MYC and KRAS oncogenes suppress ISGs in cancer-derived cell lines.

A. Immunoblots demonstrating increased MYC expression in PDAC cell lines and OS PDX-derived cell lines in comparison to respective HPDE and hFOB normal cells. **B.** LHS parental, PDAC, and OS cell lines were transfected with negative control siRNA or MYC siRNA. Knock-down efficiency was determined by immunoblot. Densities normalized to negative control siRNA

are summarized in bar graphs. Data represent mean and standard deviation of at least two biological replicates. Statistics were calculated using Student's t-test between negative control siRNA and MYC siRNA. **C-E.** LHS parental (**C**), PDAC (**D**), and OS (**E**) cell lines were treated with negative control or MYC siRNA. Transcript levels of ISGs and IFNβ relative to GUSβ reference gene was quantified by qPCR. Data represent biological duplicates. **F-G.** As an additional control to verify that siRNA treatments do not stimulate ISG expression, the cell types indicated were transfected with negative control siRNA or GAPDH siRNA. **F.** Knock-down efficiency was quantified by immunoblot. **G.** No dramatic change in IFNβ transcript levels were induced by GAPDH siRNA treatment. **H-I.** MCF10A KRAS (**H**) and PDAC (**I**) cell lines were treated with 2μM MEKi for 18 hours. Transcript levels of ISGs and IFNβ relative to GUSβ reference gene was quantified by qPCR. Data represent at least three biological replicates.

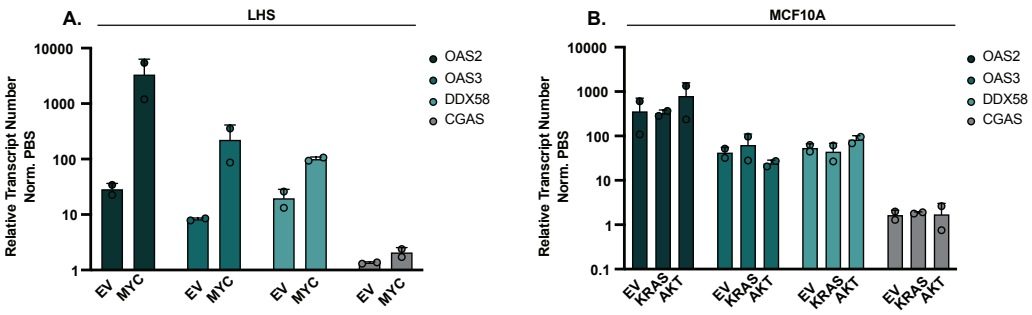

Figure 1.S 2 cGAS is not induced by IFNβ in these cell lines.

A-B. LHS EV/MYC cells (**A**) and MCF10A EV/KRAS/AKT cells (**B**) were treated with 500U/mL hIFNβ or PBS for 16 hours. mRNA levels of OAS2, OAS3, DDX58, STAT1, and CGAS relative to GUSβ reference gene were quantified by qPCR. Bar graphs report mean and standard deviation of biological duplicates.

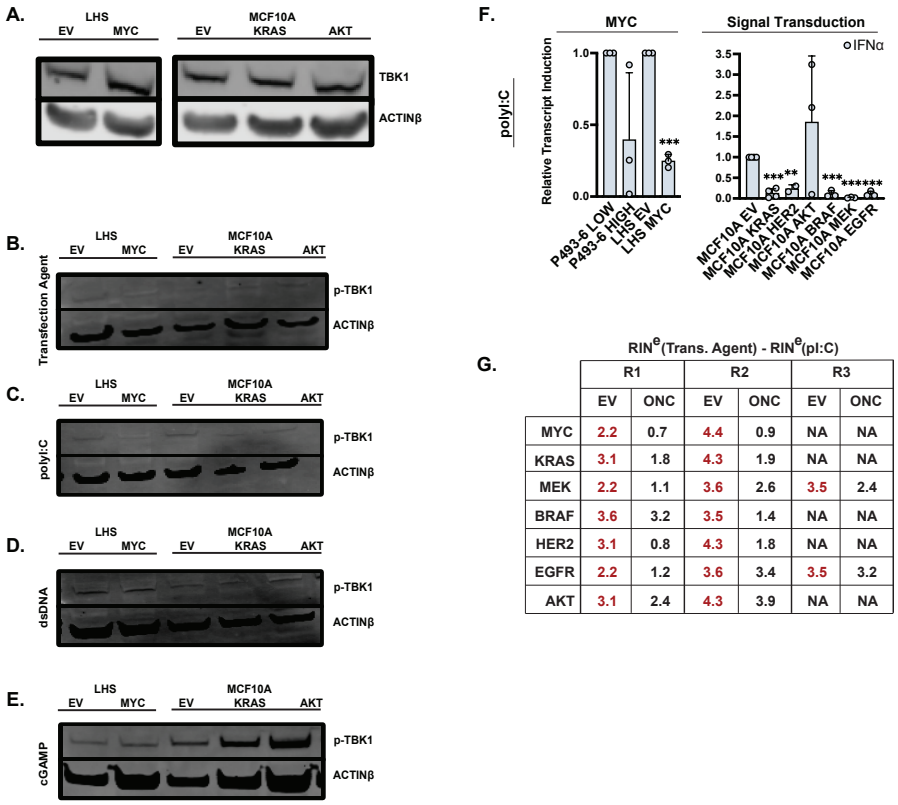

G.

RIN^e(Trans. Agent) - RIN^e(pI:C)

	R1		R2		R3	
	EV	ONC	EV	ONC	EV	ONC
MYC	2.2	0.7	4.4	0.9	NA	NA
KRAS	3.1	1.8	4.3	1.9	NA	NA
MEK	2.2	1.1	3.6	2.6	3.5	2.4
BRAF	3.6	3.2	3.5	1.4	NA	NA
HER2	3.1	0.8	4.3	1.8	NA	NA
EGFR	2.2	1.2	3.6	3.4	3.5	3.2
AKT	3.1	2.4	4.3	3.9	NA	NA

Figure 1.S 3 Cells expressing oncogenes are desensitized to dsRNA ligands.

A. Baseline total TBK1 expression was immunoblotted in LHS EV/LHS MYC and MCF10A EV/MCF10A KRAS/MCF10A AKT cells. **B-E.** Cells with or without oncogenes were treated with transfection agent alone (**B**) or complexed with polyI:C (**C**), salmon dsDNA (**D**), or cGAMP (**E**). Phosphorylation at Ser172 of TBK1 was immunoblotted. **F**. Cells with or without oncogenes were treated with transfection agent alone or complexed with polyI:C. Transcript level of IFNα relative to GUSβ reference gene was quantified by qPCR. Extent of IFNα induction was calculated as the fold change in IFNα mRNA between polyI:C treatment and transfection agent alone. Data are normalized to the induction value of EV. Bar graphs represent mean and standard deviation of at least two biological replicates. Statistics were calculated using Student's t-test between EV and oncogene. **G.** Baseline-corrected RIN^e values (transfection agent treatment - polyI:C treatment) for LHS and MCF10A oncogene models. R1, R2, and R3 are biological replicates.

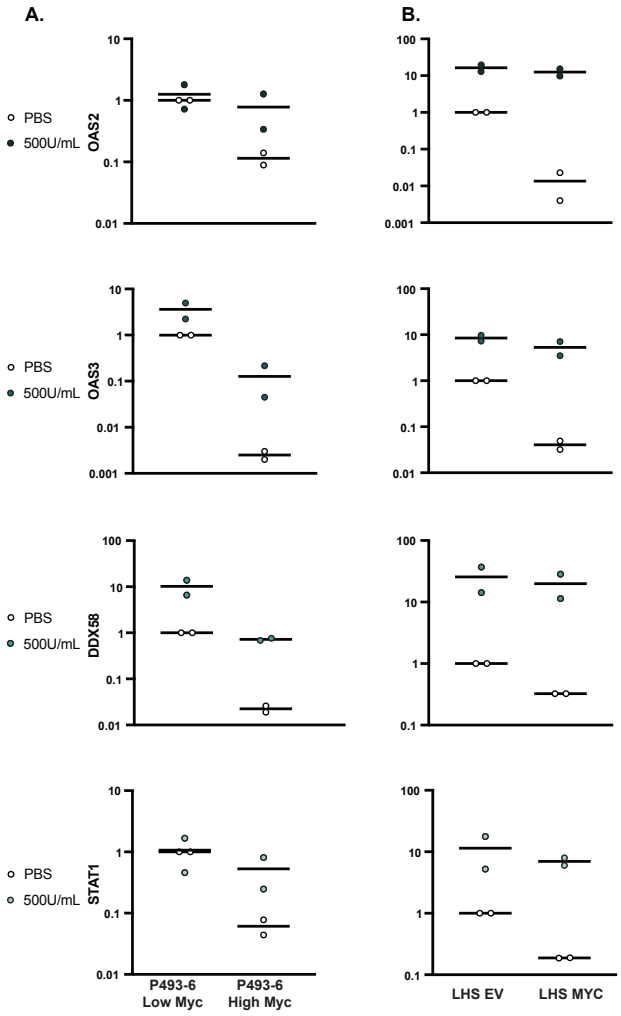

Figure 1.S 4 Cells overexpressing MYC have dramatically lower baseline expression of ISGs.

A-B. Data (same as in **Figure 4C**) for P493-6 (**A**) and LHS (**B**) MYC overexpression models were re-analyzed using different normalization: transcript values were normalized to the value of non-oncogene (P493-6 Low Myc or LHS EV) treated with PBS.

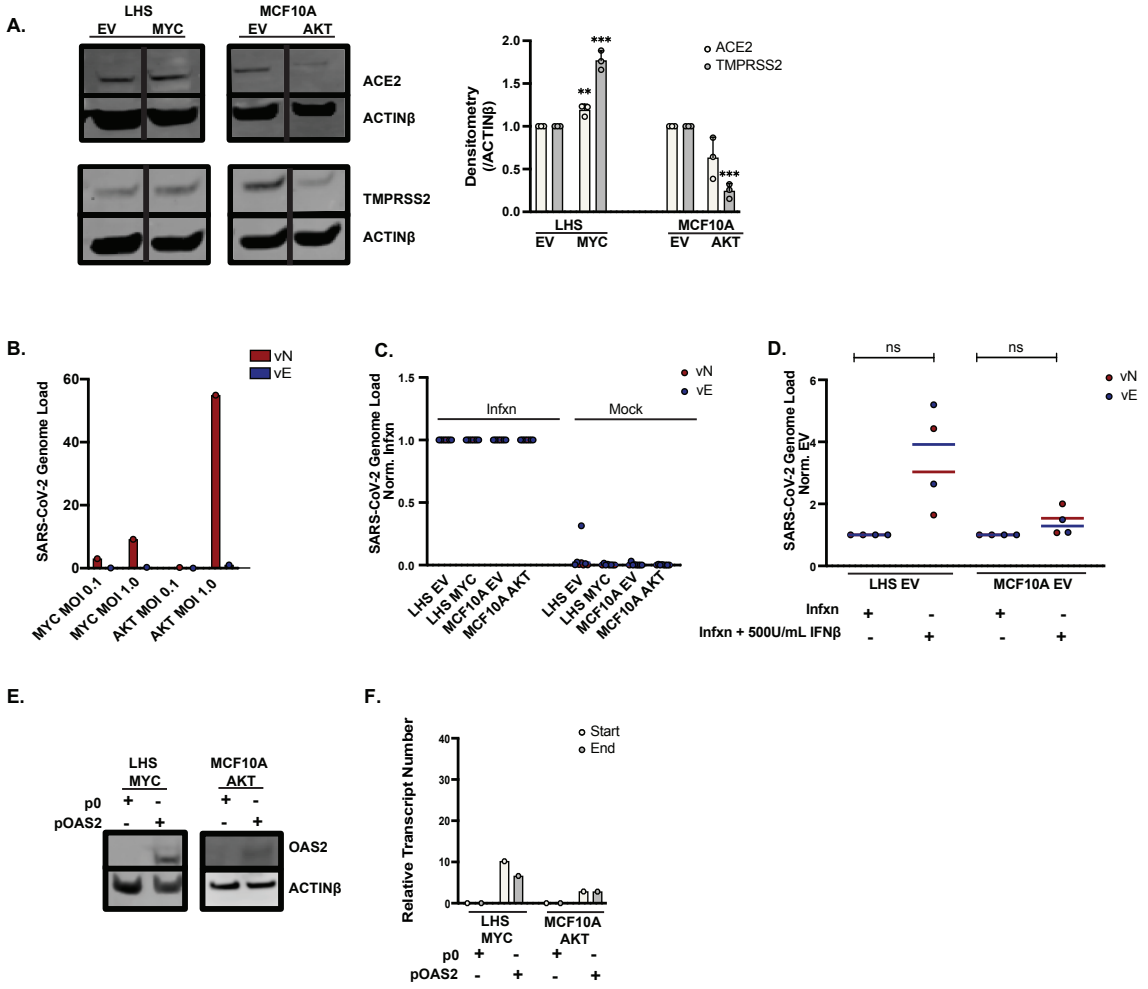

Figure 1.S 5 Controls and validations for SARS-CoV-2 assays.

A. ACE2 and TMPRSS2 were immunoblotted. Densities normalized to non-oncogene cells are summarized. Bar graphs report mean and standard deviation of three biological replicates. Statistics were calculated using Student's t-test between EV and oncogene. **B.** MOIs were chosen based on experimental pre-work. LHS MYC cells had substantial viral load at MOI 0.1. In contrast, MCF10A AKT cells required 10x the amount of virus for comparable signal and were therefore treated at MOI 1.0 (viral N (vN) and E (vE) genes relative to GUSβ host reference gene). **C**. Each SARS-CoV-2 infection experiment contained mock infection controls. qPCR CT values were >37 for no infection (mock) controls. The highest CT value for an infected cell (with the lowest amount of infection) was <32. **D.** Non-oncogene LHS EV and MCF10A EV cells with or without 500U/mL IFNβ pre-treatment were infected with SARS-CoV-2. Cellular RNA was harvested and viral genome load was quantified by qPCR amplification of vN and vE genes relative to cellular GUSβ reference gene. Transcript values were normalized to untreated conditions. Data represent biological duplicates and statistics were calculated using Student's t-test between conditions. **E-F.**

Cells expressing MYC and AKT oncogenes were engineered to stably overexpress OAS2 (pOAS2) or empty plasmid (p0). Cell lines were validated by western blot (**E**) and qPCR amplification of each end of the OAS2 transgene (relative to GUSβ reference gene) (**F**).

Table 1.S 1 Gene-set enrichment analysis shows type 1 interferon pathways are suppressed.

Gene set enrichment was performed using REACTOME bioinformatics tools. FDR for Interferon alpha/beta signaling pathway was tabulated for each oncogenic model.

Proteomics Data Set	REACTOME FDR Interferon alpha/beta signaling
P493-6	8.44E-15
LHS	4.22E-15
AKT	2.55E-15
BRAF	3.55E-15
EGFR	3.29E-15
HER2	2.78E-15
KRAS	4.44E-15
MEK	4.55E-15
OS152	9.1E-15
OS186	9.4E-15
KP4	8.22E-15
PSN1	1.19E-14

Table 1.S 2 Sequences of primers used in qPCR amplification (1–8).

Transcript	qPCR Primers (5'-3')
IFNβ[1]	**F:** AAACTCATGAGCAGTCTGCA **R:** AGGAGATCTTCAGTTTCGGAGG
pan-IFNα[1]	**F:** GTGAGGAAATACTTCCAAAGAATCAC **R:** TCTCATGATTTCTGCTCTGACAA
OAS2[6]	**F:** ACCCGAACAGTTCCCCCTGGT **R:** ACAAGGGTACCATCGGAGTTGCC
OAS3[6]	**F:** TGCTGCCAGCCTTTGACGCC **R:** TCGCCCGCATTGCTGTAGCTG
DDX58[7]	**F:** TGTGGGCAATGTCATCAAA **R:** GAAGCACTTGCTACCTCTTGC
STAT1[2]	**F:** CTAGTGGAGTGGAAGCGGAG **R:** CACCACAAACGAGCTCTGAA
IRF7[3]	**F:** CCACGCTATACCATCTACCTGG **R:** GCTGCTATCCAGGGAAGACACA
CGAS[8]	**F:** CGGGAGCTACTATGAGCACG **R:** GCCATGTTTCTTCTTGGAAACCA
SARS-CoV-2 N[5]	**F:** CACATTGGCACCCGCAATC **R:** GAGGAACGAGAAGAGGCTTG
SARS-CoV-2 E[5]	**F:** ACAGGTACGTTAATAGTTAATAGCGT **R:** ATATTGCAGCAGTACGCACACA
GUSβ[4]	**F:** CTCATTTGGAATTTTGCCGATT **R:** CCGAGTGAAGATCCCCTTTTTA

1.8 References

1. D. Hanahan, R. A. Weinberg, Hallmarks of Cancer: The Next Generation. Cell 144, 646–674 (2011).

2. Y. A. Fouad, C. Aanei, Revisiting the hallmarks of cancer. Am. J. Cancer Res. 7, 1016–1036 (2017).

3. G. Ciriello, et al., Emerging landscape of oncogenic signatures across human cancers. Nat. Genet. 45, 1127–1133 (2013).

4. B. Vogelstein, et al., Cancer Genome Landscapes. Science 339, 1546–1558 (2013).

5. F. Sanchez-Vega, et al., Oncogenic Signaling Pathways in The Cancer Genome Atlas. Cell 173, 321-337.e10 (2018).

6. J. van Riggelen, A. Yetil, D. W. Felsher, MYC as a regulator of ribosome biogenesis and protein synthesis. Nat. Rev. Cancer 10, 301–309 (2010).

7. C. V. Dang, MYC on the Path to Cancer. Cell 149, 22–35 (2012).

8. R. Taub, et al., Translocation of the c-myc gene into the immunoglobulin heavy chain locus in human Burkitt lymphoma and murine plasmacytoma cells. Proc. Natl. Acad. Sci. 79, 7837–7841 (1982).

9. C. M. Koh, et al., MYC and Prostate Cancer. Genes Cancer 1, 617–628 (2010).

10. L. C. Sayles, et al., Genome-Informed Targeted Therapy for Osteosarcoma. Cancer Discov., CD-17-1152 (2018).

11. W. Feng, et al., Myc is a prognostic biomarker and potential therapeutic target in osteosarcoma. Ther. Adv. Med. Oncol. 12, 175883592092205 (2020).

12. A. K. Murugan, M. Grieco, N. Tsuchida, RAS mutations in human cancers: Roles in precision medicine. Semin. Cancer Biol. 59, 23–35 (2019).

13. D. P. Ryan, T. S. Hong, N. Bardeesy, Pancreatic Adenocarcinoma. N. Engl. J. Med. 371, 1039–1049 (2014).

14. M. D. Muzumdar, et al., Survival of pancreatic cancer cells lacking KRAS function. Nat. Commun. 8, 1090 (2017).

15. J. Á. F. Vara, et al., PI3K/Akt signalling pathway and cancer. Cancer Treat. Rev. 30, 193–204 (2004).

16. M. Song, A. M. Bode, Z. Dong, M.-H. Lee, AKT as a Therapeutic Target for Cancer. Cancer Res. 79, 1019–1031 (2019).

17. K. K. Leung, et al., Broad and thematic remodeling of the surfaceome and glycoproteome on isogenic cells transformed with driving proliferative oncogenes. Proc. Natl. Acad. Sci. 117, 7764–7775 (2020).

18. W. Chen, et al., Large remodeling of the Myc-induced cell surface proteome in B cells and prostate cells creates new opportunities for immunotherapy. Proc. Natl. Acad. Sci. 118, e2018861118 (2021).

19. J. Cox, M. Mann, MaxQuant enables high peptide identification rates, individualized p.p.b.-range mass accuracies and proteome-wide protein quantification. Nat. Biotechnol. 26, 1367–1372 (2008).

20. Y. Perez-Riverol, et al., The PRIDE database and related tools and resources in 2019: improving support for quantification data. Nucleic Acids Res. 47, D442–D450 (2019).

21. S. Tyanova, et al., The Perseus computational platform for comprehensive analysis of (prote)omics data. Nat. Methods 13, 731–740 (2016).

22. S. Tyanova, J. Cox, “Perseus: A Bioinformatics Platform for Integrative Analysis of Proteomics Data in Cancer Research” in Cancer Systems Biology, Methods in Molecular Biology., L. von Stechow, Ed. (Springer New York, 2018), pp. 133–148.

23. J. Cox, et al., Accurate Proteome-wide Label-free Quantification by Delayed Normalization and Maximal Peptide Ratio Extraction, Termed MaxLFQ. Mol. Cell. Proteomics 13, 2513–2526 (2014).

24. A. Fabregat, et al., Reactome pathway analysis: a high-performance in-memory approach. BMC Bioinformatics 18, 142 (2017).

25. M. J. Yousefzadeh, et al., Mechanism of Suppression of Chromosomal Instability by DNA Polymerase POLQ. PLoS Genet. 10, e1004654 (2014).

26. K. J. Livak, T. D. Schmittgen, Analysis of Relative Gene Expression Data Using Real-Time Quantitative PCR and the 2−ΔΔCT Method. Methods 25, 402–408 (2001).

27. R. Wang, et al., Genetic Screens Identify Host Factors for SARS-CoV-2 and Common Cold Coronaviruses. Cell 184, 106-119.e14 (2021).

28. A. N. Honko, et al., “Rapid Quantification and Neutralization Assays for Novel Coronavirus SARS-CoV-2 Using Avicel RC-591 Semi-Solid Overlay” (LIFE SCIENCES, 2020) https:/doi.org/10.20944/preprints202005.0264.v1 (May 14, 2021).

29. QCRG Structural Biology Consortium, et al., Bi-paratopic and multivalent VH domains block ACE2 binding and neutralize SARS-CoV-2. Nat. Chem. Biol. 17, 113–121 (2021).

30. A. Pajic, et al., Cell cycle activation by c-myc in a burkitt lymphoma model cell line. Int. J. Cancer 87, 787–793 (2000).

31. Y. Dong, R. Tu, H. Liu, G. Qing, Regulation of cancer cell metabolism: oncogenic MYC in the driver's seat. Signal Transduct. Target. Ther. 5, 124 (2020).

32. S. L. Campbell, R. Khosravi-Far, K. L. Rossman, G. J. Clark, C. J. Der, Increasing complexity of Ras signaling. Oncogene 17, 1395–1413 (1998).

33. P. J. Roberts, C. J. Der, Targeting the Raf-MEK-ERK mitogen-activated protein kinase cascade for the treatment of cancer. Oncogene 26, 3291–3310 (2007).

34. E. A. Collisson, et al., Subtypes of pancreatic ductal adenocarcinoma and their differing responses to therapy. Nat. Med. 17, 500–503 (2011).

35. R. Janky, et al., Prognostic relevance of molecular subtypes and master regulators in pancreatic ductal adenocarcinoma. BMC Cancer 16, 632 (2016).

36. M. Wirth, S. Mahboobi, O. H. Krämer, G. Schneider, Concepts to Target MYC in Pancreatic Cancer. Mol. Cancer Ther. 15, 1792–1798 (2016).

37. N. M. Sodir, et al., MYC Instructs and Maintains Pancreatic Adenocarcinoma Phenotype. Cancer Discov. 10, 588–607 (2020).

38. H. Yamada, T. Yoshida, H. Sakamoto, M. Terada, T. Sugimura, Establishment of a human pancreatic adenocarcinoma cell line (PSN-1) with amplifications of both c-myc and activated c-Ki-ras by a point mutation. Biochem. Biophys. Res. Commun. 140, 167–173 (1986).

39. R. B. Seth, L. Sun, Z. J. Chen, Antiviral innate immunity pathways. Cell Res. 16, 141–147 (2006).

40. A. J. Sadler, B. R. G. Williams, Interferon-inducible antiviral effectors. Nat. Rev. Immunol. 8, 559–568 (2008).

41. A. G. Hovanessian, J. Justesen, The human 2′-5′oligoadenylate synthetase family: Unique interferon-inducible enzymes catalyzing 2′-5′ instead of 3′-5′ phosphodiester bond formation. Biochimie 89, 779–788 (2007).

42. W. M. Schneider, M. D. Chevillotte, C. M. Rice, Interferon-Stimulated Genes: A Complex Web of Host Defenses. Annu. Rev. Immunol. 32, 513–545 (2014).

43. F. Ma, et al., Positive Feedback Regulation of Type I IFN Production by the IFN-Inducible DNA Sensor cGAS. J. Immunol. 194, 1545–1554 (2015).

44. C. Vazquez, S. M. Horner, MAVS Coordination of Antiviral Innate Immunity. J. Virol. 89, 6974–6977 (2015).

45. W. Zhao, Negative regulation of TBK1-mediated antiviral immunity. FEBS Lett. 587, 542–548 (2013).

46. H. Kato, et al., Length-dependent recognition of double-stranded ribonucleic acids by retinoic acid–inducible gene-I and melanoma differentiation–associated gene 5. J. Exp. Med. 205, 1601–1610 (2008).

47. S. Luecke, et al., CGAS is activated by DNA in a length-dependent manner. EMBO Rep. 18, 1707–1715 (2017).

48. X. Cai, Y.-H. Chiu, Z. J. Chen, The cGAS-cGAMP-STING Pathway of Cytosolic DNA Sensing and Signaling. Mol. Cell 54, 289–296 (2014).

49. C. A. Jefferies, Regulating IRFs in IFN Driven Disease. Front. Immunol. 10, 325 (2019).

50. L. B. Ivashkiv, L. T. Donlin, Regulation of type I interferon responses. Nat. Rev. Immunol. 14, 36–49 (2014).

51. R. A. Porritt, P. J. Hertzog, Dynamic control of type I IFN signalling by an integrated network of negative regulators. Trends Immunol. 36, 150–160 (2015).

52. Y. Li, et al., SARS-CoV-2 induces double-stranded RNA-mediated innate immune responses in respiratory epithelial-derived cells and cardiomyocytes. Proc. Natl. Acad. Sci. 118, e2022643118 (2021).

53. M. Hoffmann, et al., SARS-CoV-2 Cell Entry Depends on ACE2 and TMPRSS2 and Is Blocked by a Clinically Proven Protease Inhibitor. Cell 181, 271-280.e8 (2020).

54. S. Zhou, et al., A Neanderthal OAS1 isoform protects individuals of European ancestry against COVID-19 susceptibility and severity. Nat. Med. (2021) https:/doi.org/10.1038/s41591-021-01281-1 (April 9, 2021).

55. H. Zeberg, S. Pääbo, A genomic region associated with protection against severe COVID-19 is inherited from Neandertals. Proc. Natl. Acad. Sci. 118, e2026309118 (2021).

56. Y. Li, et al., Activation of RNase L is dependent on OAS3 expression during infection with diverse human viruses. Proc. Natl. Acad. Sci. 113, 2241–2246 (2016).

57. M. Zhao, et al., Porcine 2′, 5′-oligoadenylate synthetase 2 inhibits porcine reproductive and respiratory syndrome virus replication in vitro. Microb. Pathog. 111, 14–21 (2017).

58. X. Lei, et al., Activation and evasion of type I interferon responses by SARS-CoV-2. Nat. Commun. 11, 3810 (2020).

59. K. L. Owen, et al., Prostate cancer cell-intrinsic interferon signaling regulates dormancy and metastatic outgrowth in bone. EMBO Rep. 21 (2020).

60. B. N. Bidwell, et al., Silencing of Irf7 pathways in breast cancer cells promotes bone metastasis through immune escape. Nat. Med. 18, 1224–1231 (2012).

61. K. P. Kotredes, A. M. Gamero, Interferons as inducers of apoptosis in malignant cells. J. Interferon Cytokine Res. Off. J. Int. Soc. Interferon Cytokine Res. 33, 162–170 (2013).

62. Y. V. Katlinskaya, et al., Suppression of Type I Interferon Signaling Overcomes Oncogene-Induced Senescence and Mediates Melanoma Development and Progression. Cell Rep. 15, 171–180 (2016).

63. L. Martin-Hijano, B. Sainz, The Interactions Between Cancer Stem Cells and the Innate Interferon Signaling Pathway. Front. Immunol. 11, 526 (2020).

64. A. Miar, et al., Hypoxia Induces Transcriptional and Translational Downregulation of the Type I IFN Pathway in Multiple Cancer Cell Types. Cancer Res. 80, 5245–5256 (2020).

65. V. Monsurrò, et al., Anti-viral state segregates two molecular phenotypes of pancreatic adenocarcinoma: potential relevance for adenoviral gene therapy. J. Transl. Med. 8, 10 (2010).

66. Q. Li, M. A. Tainsky, Epigenetic Silencing of IRF7 and/or IRF5 in Lung Cancer Cells Leads to Increased Sensitivity to Oncolytic Viruses. PLoS ONE 6, e28683 (2011).

67. W. Liao, et al., KRAS-IRF2 Axis Drives Immune Suppression and Immune Therapy Resistance in Colorectal Cancer. Cancer Cell 35, 559-572.e7 (2019).

68. N. Sivaram, et al., Tumor-intrinsic PIK3CA represses tumor immunogenicity in a model of pancreatic cancer. J. Clin. Invest. 129, 3264–3276 (2019).

69. S. F. Bakhoum, L. C. Cantley, The Multifaceted Role of Chromosomal Instability in Cancer and Its Microenvironment. Cell 174, 1347–1360 (2018).

70. S.-Y. Wu, et al., MYC suppresses STING-dependent innate immunity by transcriptionally upregulating DNMT1 in triple-negative breast cancer. J. Immunother. Cancer 9, e002528 (2021).

71. S. Kitajima, et al., Suppression of STING Associated with LKB1 Loss in KRAS-Driven Lung Cancer. Cancer Discov. 9, 34–45 (2019).

72. J. Li, et al., Metastasis and Immune Evasion from Extracellular cGAMP Hydrolysis. Cancer Discov. 11, 1212–1227 (2021).

73. H. Konno, et al., Suppression of STING signaling through epigenetic silencing and missense mutation impedes DNA damage mediated cytokine production. Oncogene 37, 2037–2051 (2018).

74. S. F. Bakhoum, et al., Chromosomal instability drives metastasis through a cytosolic DNA response. Nature 553, 467–472 (2018).

75. E. E. Parkes, et al., The clinical and molecular significance associated with STING signaling in breast cancer. Npj Breast Cancer 7, 81 (2021).

76. T. Li, Z. J. Chen, The cGAS–cGAMP–STING pathway connects DNA damage to inflammation, senescence, and cancer. J. Exp. Med. 215, 1287–1299 (2018).

77. J. A. Carozza, et al., Extracellular cGAMP is a cancer-cell-produced immunotransmitter involved in radiation-induced anticancer immunity. Nat. Cancer 1, 184–196 (2020).

78. P. Kotsantis, E. Petermann, S. J. Boulton, Mechanisms of Oncogene-Induced Replication Stress: Jigsaw Falling into Place. Cancer Discov. 8, 537–555 (2018).

79. A. Sistigu, et al., Cancer cell–autonomous contribution of type I interferon signaling to the efficacy of chemotherapy. Nat. Med. 20, 1301–1309 (2014).

80. D. R. E. Ranoa, et al., Cancer therapies activate RIG-I-like receptor pathway through endogenous non-coding RNAs. Oncotarget 7, 26496–26515 (2016).

81. M. L. Stone, et al., Epigenetic therapy activates type I interferon signaling in murine ovarian cancer to reduce immunosuppression and tumor burden. Proc. Natl. Acad. Sci. 114, E10981–E10990 (2017).

82. S. Banerjee, et al., OAS-RNase L innate immune pathway mediates the cytotoxicity of a DNA-demethylating drug. Proc. Natl. Acad. Sci. 116, 5071–5076 (2019).

83. A. A. de Cubas, et al., DNA hypomethylation promotes transposable element expression and activation of immune signaling in renal cell cancer. JCI Insight 5, e137569 (2020).

84. J. Y. H. Lim, S. A. Gerber, S. P. Murphy, E. M. Lord, Type I interferons induced by radiation therapy mediate recruitment and effector function of CD8+ T cells. Cancer Immunol. Immunother. 63, 259–271 (2014).

85. C. M. Rudin, C. B. Thompson, Transcriptional activation of short interspersed elements by DNA-damaging agents. Genes. Chromosomes Cancer 30, 64–71 (2001).

86. K. I. Leonova, et al., p53 cooperates with DNA methylation and a suicidal interferon response to maintain epigenetic silencing of repeats and noncoding RNAs. Proc. Natl. Acad. Sci. 110, E89–E98 (2013).

87. K. B. Chiappinelli, et al., Inhibiting DNA Methylation Causes an Interferon Response in Cancer via dsRNA Including Endogenous Retroviruses. Cell 162, 974–986 (2015).

88. G. Liang, F. A. Gonzales, P. A. Jones, T. F. Orntoft, T. Thykjaer, Analysis of gene induction in human fibroblasts and bladder cancer cells exposed to the methylation inhibitor 5-aza-2'-deoxycytidine. Cancer Res. 62, 961–966 (2002).

89. H. Li, et al., Immune regulation by low doses of the DNA methyltransferase inhibitor 5-azacitidine in common human epithelial cancers. Oncotarget 5, 587–598 (2014).

90. S. A. Amundson, et al., Human In vivo Radiation-Induced Biomarkers: Gene Expression Changes in Radiotherapy Patients. Cancer Res. 64, 6368–6371 (2004).

91. M. Buoncervello, et al., IFN-α potentiates the direct and immune-mediated antitumor effects of epigenetic drugs on both metastatic and stem cells of colorectal cancer. Oncotarget 7, 26361–26373 (2016).

92. A. Blaauboer, et al., Interferon-beta enhances sensitivity to gemcitabine in pancreatic cancer. BMC Cancer 20, 913 (2020).

93. R. S. A. Goedegebuure, C. Vonk, L. P. Kooij, S. Derks, V. L. J. L. Thijssen, Combining Radiation Therapy With Interferons: Back to the Future. Int. J. Radiat. Oncol. 108, 56–69 (2020).

94. R. R. Weichselbaum, et al., An interferon-related gene signature for DNA damage resistance is a predictive marker for chemotherapy and radiation for breast cancer. Proc. Natl. Acad. Sci. 105, 18490–18495 (2008).

95. N. N. Khodarev, et al., Signal Transducer and Activator of Transcription 1 Regulates Both Cytotoxic and Prosurvival Functions in Tumor Cells. Cancer Res. 67, 9214–9220 (2007).

96. I. Mellman, G. Coukos, G. Dranoff, Cancer immunotherapy comes of age. Nature 480, 480–489 (2011).

97. F. Garrido, N. Aptsiauri, E. M. Doorduijn, A. M. Garcia Lora, T. van Hall, The urgent need to recover MHC class I in cancers for effective immunotherapy. Curr. Opin. Immunol. 39, 44–51 (2016).

98. D. Dersh, J. Hollý, J. W. Yewdell, A few good peptides: MHC class I-based cancer immunosurveillance and immunoevasion. Nat. Rev. Immunol. 21, 116–128 (2021).

99. S. J. Patel, et al., Identification of essential genes for cancer immunotherapy. Nature 548, 537–542 (2017).

100. D. Romero, Interferon enhances immune-checkpoint inhibition. Nat. Rev. Clin. Oncol. 16, 6–6 (2019).

101. J. Guo, et al., Empowering therapeutic antibodies with IFN-α for cancer immunotherapy. PLOS ONE 14, e0219829 (2019).

102. N. Macedo, D. M. Miller, R. Haq, H. L. Kaufman, Clinical landscape of oncolytic virus research in 2020. J. Immunother. Cancer 8, e001486 (2020).

103. M. Mondal, J. Guo, P. He, D. Zhou, Recent advances of oncolytic virus in cancer therapy. Hum. Vaccines Immunother. 16, 2389–2402 (2020).

104. H. L. Kaufman, F. J. Kohlhapp, A. Zloza, Oncolytic viruses: a new class of immunotherapy drugs. Nat. Rev. Drug Discov. 14, 642–662 (2015).

105. S. Naik, S. J. Russell, Engineering oncolytic viruses to exploit tumor specific defects in innate immune signaling pathways. Expert Opin. Biol. Ther. 9, 1163–1176 (2009).

106. O. V. Matveeva, P. M. Chumakov, Defects in interferon pathways as potential biomarkers of sensitivity to oncolytic viruses. Rev. Med. Virol. 28 (2018).

107. S. Marozin, et al., Inhibition of the IFN-β Response in Hepatocellular Carcinoma by Alternative Spliced Isoform of IFN Regulatory Factor-3. Mol. Ther. 16, 1789–1797 (2008).

108. B. K. Jha, B. Dong, C. T. Nguyen, I. Polyakova, R. H. Silverman, Suppression of Antiviral Innate Immunity by Sunitinib Enhances Oncolytic Virotherapy. Mol. Ther. 21, 1749–1757 (2013).

109. D. F. Stojdl, et al., The Murine Double-Stranded RNA-Dependent Protein Kinase PKR Is Required for Resistance to Vesicular Stomatitis Virus. J. Virol. 74, 9580–9585 (2000).

110. D. F. Stojdl, et al., VSV strains with defects in their ability to shutdown innate immunity are potent systemic anti-cancer agents. Cancer Cell 4, 263–275 (2003).

111. M. Ahmed, S. D. Cramer, D. S. Lyles, Sensitivity of prostate tumors to wild type and M protein mutant vesicular stomatitis viruses. Virology 330, 34–49 (2004).

1.9 Supplemental References

1. X. Yu, et al., Chromatin remodeling: demethylating H3K4me3 of type I IFNs gene by Rbp2 through interacting with Piasy for transcriptional attenuation. FASEB J. 32, 552–567 (2018).

2. A. Litvinchuk, et al., Complement C3aR Inactivation Attenuates Tau Pathology and Reverses an Immune Network Deregulated in Tauopathy Models and Alzheimer's Disease. Neuron 100, 1337-1353.e5 (2018).

3. Y. Wu, et al., Function of HNRNPC in breast cancer cells by controlling the dsRNA-induced interferon response. EMBO J. 37 (2018).

4. J. Tratwal, B. Follin, A. Ekblond, J. Kastrup, M. Haack-Sørensen, Identification of a common reference gene pair for qPCR in human mesenchymal stromal cells from different tissue sources treated with VEGF. BMC Mol. Biol. 15, 11 (2014).

5. V. M. Corman, et al., Detection of 2019 novel coronavirus (2019-nCoV) by real-time RT-PCR. Euro Surveill. Bull. Eur. Sur Mal. Transm. Eur. Commun. Dis. Bull. 25 (2020).

6. G. M. de Freitas Almeida, et al., Differential upregulation of human 2′5′ OAS genes on systemic sclerosis: Detection of increased basal levels of OASL and OAS 2 genes through a qPCR based assay. Autoimmunity 47, 119–126 (2014).

7. P. K. Singh, S. Singh, D. Farr, A. Kumar, Interferon-stimulated gene 15 (ISG15) restricts Zika virus replication in primary human corneal epithelial cells. Ocul. Surf. 17, 551–559 (2019).

8. S. Cui, et al., Nuclear cGAS Functions Non-canonically to Enhance Antiviral Immunity via Recruiting Methyltransferase Prmt5. Cell Rep. 33, 108490 (2020).

Chapter 2

Discovery of VH domains that allosterically inhibit human ENPP1, a target critical for immune suppression in cancer

2.1 Abstract

Ectodomain phosphatase/phosphodiesterase-1 (ENPP1) is an extracellular enzyme that is overexpressed on cancer cells and functions as an innate immune checkpoint by hydrolyzing cyclic guanosine monophosphate adenosine monophosphate (cGAMP), an immune-stimulant. There are small molecule ENPP1 inhibitors that are in early phase clinical trials, however biologic inhibitors of ENPP1 have not yet been generated. A significant therapeutic advantage of biologics is that they can be recombinantly engineered into multi-functional formats for greater tissue selectivity and efficacy as immunotherapies. Here we utilized phage and yeast display coupled with *in cellulo* evolution to generate variable heavy (VH) single-domain antibodies against ENPP1. We discovered a VH that allosterically inhibited the hydrolysis of cGAMP and ATP. We solved a 3.2 Å-resolution cryo-electron microscopy (cryo-EM) structure for the VH inhibitor complexed with ENPP1 that confirmed its novel allosteric binding pose. Finally, we engineered the VH into multi-specific formats, including a bispecific fusion with an anti-PD-L1 checkpoint inhibitor that showed potent and selective cellular activity. Our studies demonstrate that anti-ENPP1 VH allosteric binders can be modularly engineered into cell selective, multi-functional, and potent inhibitors that

are non-competitive with cGAMP levels, and could have important benefits for immunotherapeutic development.

2.2 Introduction

Ectodomain phosphatase/phosphodiesterase-1 (ENPP1) is an extracellular enzyme that promotes immune evasion in the context of cancer progression and metastasis. ENPP1 is an immune checkpoint that modulates innate and adaptive immune pathways by hydrolyzing extracellular cyclic guanosine monophosphate adenosine monophosphate (cGAMP) and ATP(1–4). cGAMP is produced by cyclic GMP-AMP synthase (cGAS) in response to the detection of nucleic acid in the cytosol, which occurs after viral infection but also in tumor cells. Cells export and import cGAMP, triggering intercellular activation of type 1 interferons that coordinates a pleiotropic immune response and recruitment of immune cells(1, 3–7). Simultaneously, cGAMP acts as negative regulator of metastasis by suppressing epithelial-mesenchymal transition pathways in tumor cells and promoting antitumor responses in immune cells(4–6, 8, 9). The tumor microenvironment (TME) can have high concentrations of extracellular cGAMP, and ENPP1 is frequently up-regulated on tumor cells to evade *trans* cGAMP signaling, potentiating immune evasion and metastasis(1, 3–8).

Accordingly, there is significant interest in inhibiting ENPP1 to overcome therapeutic challenges for cancers that exclude lymphocytes from the TME (immune 'cold' tumors) (1–3, 6, 10–14). Immunotherapies such as checkpoint inhibitors that target CTLA-4 or PD-1/PD-L1 and ionizing radiation require tumor infiltrating lymphocytes (TILs) and are ineffective against immune 'cold' tumors(15–20). Small molecule inhibitors of ENPP1 have set therapeutic precedent for blocking the hydrolysis of endogenous cGAMP in the TME to sensitize tumor cells to

immunotherapy and radiation(1–3, 6, 10–14). Stimulator of interferon genes (STING) and toll-like receptor (TLR) activators similarly aim to inflame 'cold' tumors through type 1 interferon signaling but require direct intra-tumoral administration to prevent cytokine-mediated toxicities in healthy tissues(21–26). Extending the half-life of endogenous cGAMP via ENPP1 inhibition is an alternative strategy. However, there is still evidence of hyperactive immune responses when ENPP1 is targeted systemically underscoring the need to optimize the selectivity of ENPP1 inhibitors for tumor cells(3).

ENPP1 is expressed and secreted by normal tissues and controls multiple physiological pathways creating concerns for off-tumor toxicities and obstacles for on-tumor drug delivery(27–29). ENPP1 metabolizes nucleotide substrates and is a central regulator of purinergic signaling and inorganic phosphate levels(29, 30). Genetic deletions of ENPP1 in mice and variants of ENPP1 discovered in genome-wide association studies have connected ENPP1 activity to musculoskeletal mineralization and cardiovascular calcification diseases(27, 30–35). ENPP1 levels have also been associated with insulin resistance, plasma cell survival, cell motility, and pre-mature aging emphasizing its multi-functional biology(27, 30, 36–39). Additionally, ENPP1 on healthy tissues and in plasma sequesters systemically administered inhibitors and interferes with the delivery of drug to target tumor cells, affecting therapeutic potency and minimum dose concentrations. Therefore, therapeutic ENPP1 inhibitors require optimal selectivity for tumor cells and ideally would not be competitive with high levels of ATP and cGAMP in the TME, properties that can be difficult to design using a small molecule approach.

Biologics such as antibodies are a class of therapeutics that are ideal for recombinant engineering into multivalent formats and have strong pharmacokinetic profiles. In contrast to small molecules, an antibody-based inhibitor of ENPP1 could be optimized for tumor cell selectivity by

reformatting into multivalent constructs that recognize a second tumor-specific antigen. Importantly, such antibodies are immune handles for antibody-dependent cellular cytotoxicity (ADCC) responses by effector cells, and for T cell-directed killing when formatted as a T cell-engager. Therefore, an antibody-based inhibitor of ENPP1 could synergize cGAMP activation with targeted immunotherapy, amplifying on-target selectivity and efficacy.

Here, we describe the first reported antibody campaign to generate biologics targeting the enzymatic activity of ENPP1. Using this approach, we isolated high affinity binders to ENPP1 including a variable heavy (VH) domain that allosterically inhibits cGAMP and ATP hydrolysis. We formatted the inhibitor into bi-paratopic and bispecific molecules with potent cellular activities. Our most effective inhibitor was a bispecific construct with the clinically approved anit-PD-L1 checkpoint inhibitor Envafolimab. This bispecific format combined two therapies into a single molecule rendering it more selective for tumor cells harboring high PD-L1 together with ENPP1 than individual monotherapies. Finally, we solved a 3.2 Å-resolution cryo-electron microscopy (cryo-EM) structure of the VH inhibitor in complex with ENPP1, elucidating the allosteric mechanism of inhibition and providing insights for structure-guided designs of next-generation therapeutics.

2.3 Results

Single-domain VH-phage display library generated high affinity binders to native ENPP1 on PDX-derived osteosarcoma (OS) cells.

ENPP1 is a type 2 membrane protein with a nuclease domain, phosphodiesterase domain (PDE), and two somatomedin domains (SMB1 and SMB2) orientated toward the extracellular space (**Figure 2.1**)(40–43). On the cell membrane, ENPP1 forms a homo-dimer but is also secreted

as an enzymatically active monomer(43). To express antigen for phage display, the ectodomain of human ENPP1 was modified by truncating the SMB1 and SMB2 domains (ΔSMB) and mutating the catalytic threonine to alanine (T256A). For bead-based phage display selections, the C-terminus of the ENPP1 antigen was fused to an Fc domain (ENPP1-Fc) with a C-terminal AviTag via a linker containing a tobacco etch virus (TEV) protease site (**Figure 2.1**). The biotinylated antigen was immobilized on streptavidin beads for iterative rounds of phage display.

We used our synthetic single-domain VH library based on a stabilized and fully human trastuzamab scaffold(44). VH domains have three complementary determining regions (CDRs) and generally have weaker affinities than Fabs having six CDRs. However, the smaller size of the VH domain (15kDa) could have significant advantages over a Fab (60kDa) to bind cryptic or sterically challenging sites. Moreover, VH binders can be affinity matured or linked into multivalent formats as a single chain to significantly improve their affinities(44).

We performed parallel VH-phage selections using two different elution strategies to generate binders globally to ENPP1 and specifically to inhibitory epitopes. In the first standard selection, the bound VH-phage were released using TEV protease treatment to capture any VH binding to the ENPP1 ectodomain (**Figure 2.1**). In the second substrate-specific selection, the bound VH-phage were eluted using excess ATP to isolate clones that are competitive with substrate binding or are trapping the enzyme in an inactive conformation (**Figure 2.1**). Four rounds of selection were performed by increasing both positive and negative selection stringencies as indicated (**Figure 2.1**).

The TEV and ATP elution strategies isolated non-overlapping sets of VH clones that were triaged to a panel of four VH candidates based on affinity and cellular staining (TEV elution: VH24 and VH38, ATP elution: VH27 and VH31; CDR sequences: **Supplemental Figure 2.S1**). First,

the VH were expressed as bivalent VH-Fc constructs and their binding constants were measured to be in the single-digit nanomolar range using biolayer interferometry (**Figure 2.1**). On-cell binding was assayed using a patient-derived xenograft (PDX)-derived osteosarcoma (OS) cell line with high ENPP1 expression (OS384)(45, 46). For a paired isogenic comparison, OS384 cells were engineered with CRISPR knockout (KO) of ENPP1 or safe-guide (SG) control. VH-Fc constructs containing VH24, 27, 31, and 38 all recognized epitopes on ENPP1 in its native dimeric form on the PDX-derived OS384 cells. VH31-Fc and VH38-Fc were exceptionally strong on-cell binders with 7.5-fold and 2.5-fold greater staining of SG over KO cell lines. VH24-Fc and VH27-Fc had lower SG over KO staining ratios of 1.3 and 1.5 despite all the binders having similar affinities and dissociation kinetics (**Figure 2.1, Supplemental Figure 2.S1**). It is possible that the epitopes recognized by VH24-Fc and VH27-Fc are less accessible when native ENPP1 is dimerized on the cell membrane compared to the modified ENPP1-Fc antigen. Several factors that might contribute to steric effects specific to the native context are the presence of SMB1 and SMB2 domains (truncated in the ENPP1-Fc antigen), the orientation of ENPP1 as an N-terminal dimer on the membrane (vs. ENPP1-Fc as a C-terminal dimer), or obstructions from other protein interactors on the membrane such as the insulin receptor(36, 37).

Next, we expressed catalytically active (T256) WT ENPP1-Fc and performed luciferase-based functional assays monitoring ATP or cGAMP hydrolysis to identify VH candidates in the panel that could inhibit ENPP1. VH27-Fc was the only molecule found to functionally inhibit recombinant ENPP1 with Michaelis-Menten K_i values for ATP and cGAMP of 220nM (95% confidence interval (CI_{95}) 160 to 300 nM) and 130 nM (CI_{95} 97 to 160 nM), respectively (**Figure 2.1**). Interestingly, V_{app} in the presence of VH27-Fc did not reach the V_{max} of the enzyme as substrate concentration was increased, indicating that VH27-Fc was non-competitive with

substrate and inhibits ENPP1 by an allosteric mechanism. This was interesting because VH27 was isolated by elution with excess ATP, yet it was neither directly nor conformationally competitive with substrate therefore its discovery may have been serendipitous.

Finally, to confirm that VH27-Fc could also inhibit native soluble ENPP1 we tested the inhibitor in donor human plasma. VH27-Fc inhibited the hydrolysis of cGAMP *ex vivo* with IC_{50} values of approximately 3.8 and 3.9 uM assayed over 90 minutes and 24 hours, respectively (**Figure 2.1**). Others have reported small molecule ENPP1 inhibitors with IC_{50} values that are higher when tested using plasma or plated cells than the value measured with recombinant enzyme(2, 12). The shift in potency reflects non-specific protein binding in more biologically complex samples. Differences in antigen avidity and epitope accessibility are additional variables that will affect the efficacy of VH27-Fc.

Yeast display of VH27 yielded a more thermostable mutant with improved K_D, K_i, and IC_{50}.

Single-chain VH are well-suited for affinity maturation to evolve even stronger binders. Having validated VH27 as an ENPP1 inhibitor in recombinant enzyme and plasma assays, we aimed to improve its binding kinetics and stability using autonomous hypermutation yeast surface display (AHEAD)(47). As previously described, the AHEAD yeast strain utilizes an orthogonal error-prone polymerase that exclusively replicates and mutagenizes an orthogonal plasmid encoding chosen genes without affecting genomic DNA (OrthoRep system)(47, 48). We incorporated the VH27 gene into this plasmid with a HA tag to quantify expression. In iterative rounds of selection, yeast cells continuously-diversifying VH27 sequences were stained with both fluorescently-labeled antigen and anti-HA antibody and analyzed by fluorescence-activated cell sorting (FACS) (**Figure 2.2, Supplemental Figure 2.S2**).

After five rounds of *in cellulo* diversification and FACS sorting with the AHEAD process, several VH27 mutants emerged and were detected with next-generation sequencing (NGS) read abundances over 1%. Interestingly, T75I and A89V were top ranked mutations located in the VH framework (**Figure 2.2**). Residue T75I is in a scaffold loop directly adjacent the tyrosine-rich CDR H1; this preference for isoleucine could indicate hydrophobic interactions with aromatic CDR H1 residues (based on VH scaffold in PDB 7JWB)(44). The T75I substitution decreased the dissociation rate supporting the hypothesis that it might be extending effects to the CDR configuration. The A89V mutation enhanced the association rate, which can be related to gains in stability that increase the effective concentration of folded protein. Residue A89V is in spatial proximity to the VH domain C-terminus and might affect compaction and stability (based on VH scaffold in PDB 7JWB)(44).

We then built a consensus mutant (VH27/T75I/A89V) that had improved association and dissociation rates, and produced a bivalent VH-Fc with a sub-nanomolar K_D (**Figure 2.2, Supplemental Figure 2.S2**). These gains corresponded to lower K_i values for ATP and cGAMP hydrolysis, 120 nM (CI_{95} 83 to 160 nM) and 43 nM (CI_{95} 30 to 57 nM), respectively (**Figure 2.2**). VH27/T75I/A89V-Fc was also a three-fold stronger inhibitor of *ex vivo* human plasma cGAMP degradation with IC_{50} values between 1.2 uM and 1.4 uM for three donors (**Figure 2.2**). Additionally, we tested the inhibitor for cross-reactivity with mouse ENPP1 (mENPP1), which has approximately 80% overall homology to human ENPP1(42). VH27/T75I/A89V-Fc inhibited the hydrolysis of ATP and cGAMP by recombinant mENPP1 monomer and blocked cGAMP degradation by native mENPP1 in *ex vivo* C57BL/6J mouse plasma (**Supplemental Figure 2.S2**).

Aligned with our hypothesis that these scaffold changes might impact domain stability, we determined that the double mutant had enhanced biophysical properties. The thermal melting temperature for single-domain VH27 was dramatically increased from 48°C to 63°C with the T75I/A89V mutations under non-reducing conditions (**Figure 2.2**). When the VH disulfide was reduced with BME, the double mutant was still significantly more stable than WT VH27, with melting temperatures of 50°C and 45°C, respectively (**Figure 2.2**). Finally, incorporation of the two mutations decreased the level of aggregation observed by size exclusion chromatography (SEC) when expressed in the VH-Fc format (**Figure 2.2**). While aggregated WT VH27-Fc produced some non-specific cellular stickiness, VH27/T75I/A89V-Fc showed dramatically less background staining on OS384 KO cells (**Supplemental Figure 2.S1, Supplemental Figure 2.S3**). We used VH27/T75I/A89V for the rest of the experiments and refer to it as VH27.2 for brevity.

Bi-paratopic and bispecific VH constructs improved cellular inhibition by increasing membrane localization.

We tested if the VH inhibitor could be engineered into multivalent formats to enhance tumor cell specificity. As examples, we built bi-paratopic and bispecific tetravalent Fc constructs that append a second recognition arm onto the C-terminus of the Fc (**Figure 2.3**). These Fc formats are symmetric and do not require specialized 'knob-into-hole' expression or assembly pipelines; the multi-valent constructs could be produced in high yields in mammalian cell culture and are biophysically stable (**Supplemental Figure 2.S3**).

To generate a bi-paratopic inhibitor, we performed epitope binning for the VH-Fc panel and found that each could simultaneously engage ENPP1 in the presence of VH27-Fc, indicating the epitopes were non-overlapping and compatible to combine with VH27-Fc (**Figure 2.3**). We

created the VH27.2 bi-paratopic inhibitor using VH31 because it displayed the best cellular staining of OS384; we hypothesized that the VH31 arm would increase the local concentration of inhibitor on ENPP1 on the membrane (**Figure 2.1**). Biolayer interferometry verified that the tetravalent bi-paratopic molecule had a sub-nanomolar binding constant to ENPP1 *in vitro*, and its IC_{50} in plasma was measured to be between 0.96 uM and 1.2 uM for three donors (**Figure 2.3**). Next, we stained OS384 SG and KO cells and demonstrated that valency with VH31 increased the specific binding by 69%, with SG over KO ratios of 1.6 and 2.7 for VH27.2-Fc and bi-paratopic inhibitor, respectively (**Figure 2.3, Supplemental Figure 2.S3**). Finally, EC_{50} values for cellular binding on MDA-MB-231 cells were determined for VH27.2-Fc, VH31-Fc, and bi-paratopic inhibitor. The EC_{50} values for VH27.2-Fc and VH31-Fc were 36 and 0.65 uM, respectively. Compared to VH27.2-Fc, the bi-paratopic molecule decreased EC_{50} by over 40% to a value of 21 uM (**Figure 2.3**).

The inhibitory potency of the bi-paratopic inhibitor and VH27.2-Fc were compared in MDA-MB-231 cellular assays using two substrates of ENPP1, cGAMP (**Figure 2.3**) and p-Nitrophenyl thymidine 5'-monophosphate (pNP-TMP) (**Figure 2.3**). While pNP-TMP is a synthetic substrate hydrolyzed by other extracellular phosphodiesterase enzymes, it provides a direct colorimetric read-out enabling higher throughput and lower noise than a cGAMP ELISA. These cellular assays demonstrated equivalent trends for cGAMP and pNP-TMP substrates. VH27.2-Fc inhibited cellular ENPP1 with IC_{50} values between 0.73 and 0.78 uM, which was lower than the IC_{50} value for soluble ENPP1 in plasma (**Figure 2.2, Figure 2.3**). This is consistent with there being higher avidity for the homo-dimeric membrane species compared to the secreted monomer, which should increase the ability to specifically target the membrane bound form of

ENPP1. The bi-paratopic inhibitor was approximately twice as potent as VH27.2-Fc with a cellular IC_{50} value between 0.30 to 0.40 uM (**Figure 2.3**).

Compared to the parent VH27/T75I/A89V-Fc inhibitor, the bi-paratopic inhibitor greatly improved the IC_{50} against membrane-bound ENPP1 but only moderately decreased the IC_{50} in plasma. These results are consistent with previous flow cytometry data that demonstrated VH27.2-Fc had a lower capacity to bind native ENPP1 in membrane environments. Valency with the highly accessible VH31 epitope therefore distinctly rescued cellular binding (**Figure 2.1, Figure 2.3**). Interestingly, there was a hook effect for the highest concentration of bi-paratopic molecule in the cell-based assays that was not observed in plasma (**Figure 2.3**). Single domain VH27 inhibited ENPP1 activity and the inhibitors blocked monomeric ENPP1 in plasma indicating the hook effect is not produced through dimeric cross-linking. There may be steric limitations when the VH31 epitope becomes saturated on both subunits of the ENPP1 homo-dimer.

Finally, we generated a bispecific ENPP1 inhibitor using the clinically approved PD-L1 checkpoint inhibiting nanobody, Envafolimab (**Figure 2.3**)(49, 50). As discussed, several reports have shown that co-treating small molecule ENPP1 inhibitors with an immune checkpoint blockade significantly enhances tumor regression(11, 13, 14). Bispecific biologics combine these two synergizing therapies into a single molecule. Further, overexpressed PD-L1 on various cancers will increase the local concentration of VH27.2 on tumor cell membranes to augment potency and tumor selectivity.

We constructed the bispecific VH27.2-Envafolimab inhibitor and confirmed its binding to both ENPP1-Fc and PD-L1-Fc antigens (**Figure 2.3**). The bispecific also retained its inhibitory function in *ex vivo* human plasma assays (**Figure 2.3**). PD-L1 is highly expressed on MDA-MB-231 cells so we tested binding of the bispecific format on these cells for comparison with VH27.2-

Fc. The bispecific inhibitor exhibited dramatically enhanced cellular staining, with its EC_{50} value decreased to single-digit nanomolar (**Figure 2.3**). The orders of magnitude increase in cellular localization corresponded in seven- to ten-fold improvements in the cellular IC_{50} values compared to that of the VH27.2-Fc. The IC_{50} for the bispecific inhibitor was measured to be 0.11 and 0.07 uM when MDA-MB-231 cells were incubated with cGAMP and pNP-TMP substrates, respectively (**Figure 2.3**). As observed for the bi-paratopic inhibitor, there was distinct improvement in the inhibition of membrane ENPP1 but not the secreted form in plasma samples. This further validated that engineering multi-specific recognition of a second tumor epitope or antigen can improve cellular localization to optimize potency. As a result, co-targeting PD-L1 yielded our most effective molecule by driving significantly higher inhibitor concentrations on the tumor cell membrane.

We hypothesized that specific tumor localization of Envafolimab would similarly benefit from dual-targeting ENPP1. OS384 PDX-derived cells have very high PD-L1 levels and therefore we stained SG ($ENPP1^{+}$/$PD\text{-}L1^{+}$) and KO ($ENPP1^{-}$/$PD\text{-}L1^{+}$) cell lines with the bispecific inhibitor. The bispecific inhibitor demonstrated 69% greater binding to OS384 SG cells that are double-positive for ENPP1 and PD-L1 compared to OS384 ENPP1 KO cells that only express PD-L1 but not ENPP1 (**Figure 2.3**). These results underscore the advantages of bispecific biologics for optimizing tumor selectivity compared to the individual monotherapies, which will limit off-tumor drug sequestration and toxicities.

Reformatted VH domains function as immunotherapy scaffolds and next-generation protein degraders.

ADCC is a fundamental mechanism of clinically approved therapeutic antibodies(51–53). In addition to inhibiting ENPP1, constructs containing Fc domains engage Fc receptors such as

CD16 on NK cells and macrophages to activate ADCC(54, 55). As expected, the bivalent and tetravalent Fc inhibitors were high affinity binders of CD16, whereas the single-domain VH27.2 did not bind to Fc receptor (**Figure 2.4**).

VH domains can be engineered into bispecific T cell-engagers (BiTEs) that incorporate a CD3 recognition arm. We generated a BiTE by linking the single-domain VH27.2 with OKT3, a well-established anti-CD3 scFv (**Figure 2.4**)(56, 57). In activated T cells, nuclear factor of activated T cells (NFAT) is a family of transcription factors that regulate the expression of cytokines and growth factors for immune responses. Jurkat T cells that express GFP under the control of a NFAT response element (NFAT-GFP reporter) were robustly activated after a 20 hr incubation with 10 nM BiTE and ENPP1-Fc immobilized on streptavidin magnetic beads. There was no NFAT response when Jurkat cells were cultured without the BiTE or without ENPP1-coupled beads, demonstrating the high specificity of T cell activation by the VH27.2 BiTE (**Figure 2.4, Supplemental Figure 2.S3**).

The therapeutic space for biologics and immunotherapies continues to expand and the VH from our panel can be directly ported into novel formats. For example, protein degraders are a new class of bispecific molecules with degradation-inducing arms(58–60). AbTACs incorporate an IgG arm that recruits the membrane-bound E3 ligase RNF43 to ubiquitinate lysine residues on the cytosolic domain of a target protein and designate it for lysosomal degradation(58). KineTACs are fusions with a cytokine or chemokine that bind internalizing receptors and mediate lysosomal degradation of the target protein(59). While only one VH in our panel recognized a functional epitope on ENPP1, it is possible that any VH can be constructed into an AbTAC or KineTAC to hijack degradation pathways and inactivate ENPP1.

There are three lysine residues in the cytosolic domain of ENPP1 suggesting it could be a viable target for RNF43 ubiquitination. We constructed 'knob-into-hole' bispecific VH-IgG AbTACs for VH24, VH27.2, VH31, and VH38 (**Figure 2.4**). Whereas bispecific molecules with two Fab arms require complicated expression and assembly protocols to prevent light chain mismatching, the VH lacks a light chain permitting facile co-expression of 'knob' and 'hole' pieces in a single mammalian transfection. These were purified using a His tag introduced on the 'knob' arm to exclude contaminating 'hole-hole' homo-dimers.

Degradation by formation of a tertiary complex of E3 ligase, bispecific degrader, and target protein is epitope dependent(59, 61). We treated MDA-MB-231 cells, which express RNF43 and have been used for RNF43-mediated degradation of target proteins previously, with the AbTACs and discovered that the VH27.2 AbTAC was the most potent ENPP1 degrader(58, 61). 44% of ENPP1 was degraded after 24 hr incubation with 500 nM VH27.2 AbTAC. Treatment with 500 nM VH27.2-Fc did not decrease ENPP1 levels, validating that the AbTAC is inducing protein degradation as opposed to internalization (**Figure 2.4, Supplemental Figure 2.S3**). It is not uncommon for AbTACs show this level of maximal degradation (D_{max}) as it is a composite of synthesis and degradation rates(58, 59, 61). The AbTAC still retains function as an inhibitor, so we believe degradation will be additive.

Cryo-EM structure of VH27.2 in complex with ENPP1 elucidated the allosteric binding pose.

To reveal the epitope and mechanism of allosteric inhibition we solved a 3.2 Å-global resolution cryo-EM structure of VH27.2 in complex with T256A ENPP1-Fc. Not surprisingly, the density for the Fc domains was not observed due to the flexible hinge and linker. The cryoEM structure showed the expected 2:1 VH:ENPP1 homo-dimer stoichiometry, with a VH bound to each ENPP1 ectodomain configured in a head-to-head dimer (**Figure 2.5, Supplemental Figure**

2.S4). The VH-ENPP1 structure was aligned to the crystal structure of full length ENPP1 ectodomain with SMB domains (PDB 6wfj) and the global RMSD was 0.972 (**Supplemental Figure 2.S4**)(42). Overlaying these structures, it was apparent that the VH CDR H3 bound close to the SMB domains but without clashing. Notably, there would be insufficient space to accommodate a light chain indicating our original motivation to use small VH domains to target cryptic epitopes was imperative. The VH-ENPP1 structure was also aligned to the mouse ENPP1 crystal structure (PDB 4gtw) (**Supplemental Figure 2.S4**)(40). While overall homology between mouse and human is approximately 80%, the catalytic domain shares close to 90% homology(42). As expected, key interface interactions were preserved explaining species cross-reactivity between human and mouse ENPP1.

All three VH CDRs engaged ENPP1 with impressive shape-complementarity, binding a region close to the active site, but not occluding the site or interacting with the residues in the nucleotide binding pocket (**Figure 2.5**)(40, 41). Density fit to an AMP ligand was observed in the active site (likely left from purification since no AMP was supplied exogenously), demonstrating that VH27.2 and AMP can bind simultaneously. Substrates like ATP and cGAMP bind in the same nucleotide pocket as AMP, the product of catalysis. This suggests that these substrates would also be able to bind to the ENPP1-VH complex, consistent with the observed non-competitive hydrolysis inhibition. The VH was skewed toward the guanosine-adjacent site, and overlaying the VH-ENPP1 structure with the crystal structure of mouse ENPP1 complexed with 3'-5'-linked pApG (a cGAMP hydrolysis linear intermediate) (PDB 6AEK) exhibited that the VH would clash with the guanosine base(41). However, a previous report found that the guanosine base has a degree of mobility within the pocket, such that mutations to these guanosine-adjacent resides did not completely disrupt cGAMP binding and hydrolysis(3). Based on this positional flexibility, the

VH overlap with these residues would not necessarily prevent cGAMP binding, as is supported by our Michaelis-Menten characterizations.

We performed epitope analysis by alanine scanning residues that formed specific interactions between VH CDRs and ENPP1 (**Figure 2.5**). These structure-function characterizations identified two hot spots on VH27.2 that contribute to the binding and allosteric inhibition of ENPP1: (1) CDR H1 Y30 and Y31 and (2) CDR H3 Y102, W104, and Y105.

The VH CDR H1 loop is internally structured through pi-stacking of Y31 and Y30, which are both within range of cation-pi interactions with ENPP1 K528. Furthermore, VH Y31 pi-stacks with ENPP1 H380 (**Figure 2.5**). VH27.2-Fc binding to ENPP1 was abolished when Y31 or Y30 were mutated to alanine (**Figure 2.5**). WT VH27.2-Fc did not bind to ENPP1 H380A however retained affinity for ENPP1 K528A, indicating H380 is the essential contact and its aromatic interaction with VH Y31 is energetically indispensable (**Figure 2.5**). Together, ENPP1 H380, VH Y31, VH Y30, and ENPP1 K528 connect an extensive aromatic-cation network that greatly contributes to VH affinity.

The pi-stacking between VH Y31 and ENPP1 H380, a residue in the catalytic core of ENPP1 that coordinates Zn^{2+}, may contribute to the allosteric inhibition and three-fold selectivity for cGAMP inhibition over ATP (**Figure 2.5**). Because the hydrolytic activity of ENPP1 is highly dependent on Zn^{2+} coordination of substrates, we hypothesize that VH Y31 pi-stacking with H380 could exert an inhibitory effect. Although lack of binding between VH27.2-Fc Y31A and ENPP1 prevented enzymatic inhibition assays, we note that the mouse ENPP1 histidine (mENPP1 H362) corresponding to human ENPP1 H380 was previously discovered to be essential for cGAMP but not ATP degradation, and mutant mENPP1 H362A was unable to coordinate Zn^{2+} for productive cGAMP hydrolysis(3). There was Zn^{2+} density in the VH-ENPP1 complex with AMP in the

nucleotide pocket, therefore the pi stacking network involving H380 may lower the pKa of the histidine residue without completely diminishing its affinity for Zn^{2+} like was observed for the more extreme histidine-to-alanine mutation. Another possibility is that VH engagement at this site may perturb reaction geometry or conformational trajectory during catalysis.

Structure-guided mutagenesis uncovered a second hot spot, CDR H3, that is critical to binding affinity as well as inhibition of ATP hydrolysis specifically. VH CDR H3 residues Y102, W104, and Y105 pi-stack with each other to form a hydrophobic pocket that makes several contacts with ENPP1 residues: weak polar interaction between VH Y102 and ENPP1 S377 sidechain; hydrogen bonding between VH W104 and ENPP1 G342 backbone; pi-stacking between VH W104 and ENPP1 F346; and cation-pi interaction between VH Y105 and ENPP1 R395, requiring the R395 sidechain to break its salt bridge with ENPP1 E347 and rotate compared to its register in non-VH-bound ENPP1 (PDB 6wjf) to prevent clashing with Y105 (**Figure 2.5**). The major energetic contributions to binding of these three aromatic residues were validated by alanine-scanning. VH27.2-Fc W104A did not bind to ENPP1, and VH27.2-Fc Y102A and Y105A had weakened affinity towards ENPP1 by two orders of magnitude (**Figure 2.5, Supplemental Figure 2.S4**).

Remarkably, 500 nM VH27.2-Fc Y102A failed to inhibit ATP hydrolysis by ENPP1, but still inhibited cGAMP and pNP-TMP hydrolysis (**Figure 2.5**). Comparing VH27.2-Fc Y102A to WT, the Michaelis-Menten K_i for cGAMP increased approximately five-fold to 220 nM (CI_{95} 170 to 290 nM). However the K_i for ATP was greater than 4.5 uM (CI_{95} 2.8 to 11 uM), indicating the Y102A mutation conferred extraordinary substrate selectivity (**Supplemental Figure 2.S4**). This ATP-specific effect for the VH27.2-Fc Y102A mutant could implicate the weak polar interaction with ENPP1 S377, or alternatively that the tyrosine residue supports the structural integrity of the

hydrophobic pocket with VH W104 and Y105. To decouple these effects, we generated a phenylalanine mutant for Y102 and found it rescued the affinity and inhibition of ATP hydrolysis (**Figure 2.5**). These results indicated that the polar contact is dispensable but the hydrophobic interactions are critical for shaping the CDR conformation. Similarly, VH27.2-Fc Y105F and W104F mutants restored affinity compared to the respective alanine mutants, confirming the importance of this hydrophobic filling at the ENPP1 interface (**Figure 2.5**).

Intriguingly, the VH27.2-Fc W104F mutation recapitulated the substrate bias of the Y102A mutation, where VH27.2-Fc W104F was much less potent towards inhibition of ATP hydrolysis compared to cGAMP or pNP-TMP hydrolysis (**Figure 2.5**). The K_i value for cGAMP was 270 nM (CI_{95} 240 to 300 nM) but the K_i value for ATP was 2.3 uM (CI_{95} 1.2 to 10 uM) (**Supplemental Figure 2.S4**). While WT VH27.2-Fc was 2.7-fold selective for inhibiting cGAMP hydrolysis over ATP hydrolysis, VH-Fc Y102A and W104F were ~20.6- and ~8.5-fold selective, respectively (**Figure 2.5**). Even though WT, Y102A, and W104F VH-Fc had dramatically different binding affinities (K_D = 0.7, 111, and 14.2 nM, respectively) there was no correlation (R^2=0.17) between VH-Fc affinity and the K_i value for cGAMP. In contrast, there was strong correlation (R^2=0.85) when comparing VH-Fc affinity and the K_i value for ATP, indicating destabilization of CDR H3 disproportionately de-tuned the potency for ATP (**Figure 2.5, Supplemental Figure 2.S4**). Mechanistically, the W104F mutation disrupts the hydrogen bond to ENPP1 G342 backbone carbonyl. Phenylalanine is also unable to fill the hydrophobic hole from the tryptophan and might weaken the aromatic interaction with ENPP1 F346. WT VH27.2-Fc had reduced affinity for ENPP1 F346A mutant, validating that the pi-stacking between ENPP1 F346 and VH W104 is an important energetic component (**Figure 2.5**).

Comprehensively, these mutagenesis results suggested that VH W104 is imperative for the ATP inhibitory mechanism, and the hydrophobic filling of Y102 and Y105 support the correct conformation of W104. Further, VH-Fc Y102A and W104F mutations minimally affected the K_i for cGAMP, implying that CDR H1 engagement with ENPP1 H380 has a dominant role in the inhibitory mechanism for cGAMP. Therefore, structure-activity analysis revealed that the VH CDRs engage distinct sites on ENPP1 that separately modulate the hydrolysis of cGAMP or ATP. These discoveries may inspire designs of new small molecule and biologic inhibitors that interrogate the same allosteric epitopes as our VH domain.

2.4 Discussion

Using display technologies and protein engineering we generated first-in-class biologics and immunotherapies targeting ENPP1, including an allosteric VH inhibitor with cellular IC_{50} as low as 70-110 nM in a bispecific format. The cryo-EM structure verified that the VH epitope is non-competitive with substrate and functional analyses revealed novel mechanisms of inhibition at CDRs H1 and H3. The structure and cellular binding data confirmed that the inhibitory epitope is sterically challenging, substantiating our rationale to use a single-domain library to produce binders and inhibitors. The VH domains were recombinantly engineered into various stable formats combining nanobodies, scFv, and IgG arms, exemplifying their utility and modularity for building diverse, multi-specific molecules. As examples we constructed biologics that combine ENPP1 inhibition with 1) PD-L1 blockade, 2) ADCC function, 3) T cell activation, and 4) targeted ENPP1 protein degradation. These novel anti-ENPP1 VH can readily be repurposed into other next-generation biologics and immunotherapies as they are developed.

As potent small molecule inhibitors for ENPP1 begin to show exciting translational results, biologics provide a complementary mode of inhibition with different strengths(2). First, drug localization to tumor cells is important for minimizing potential off-tumor toxicities, including bone and heart calcification and adverse immune activation. Additionally, strategies to optimize delivery of the inhibitor to tumor cells mitigates the impact of soluble ENPP1 in plasma that could sequester drug and decrease therapeutic potency. It can be challenging to engineer small molecule therapeutics for greater tumor selectivity since they typically distribute systemically. In contrast, we recombinantly expressed the VH inhibitor as a bispecific molecule dual-targeting high PD-L1 expression on MDA-MB-231 and OS384 cells. This bispecific approach robustly increased the concentration of inhibitor on the cell membrane and significantly improved the cellular IC_{50} without changing the IC_{50} in human plasma. Co-targeting other up-regulated biomarkers on the tumor membrane, such as HER2 or EGFR, can similarly bias tumor cell localization to address various cancer types.

Second, studies have indicated that combining ENPP1 inhibitors with checkpoint inhibitors or ionizing radiation increases their therapeutic index against immune 'cold' tumors(11, 13, 14). It is difficult to build drug-like large bifunctional small molecules. In contrast, straightforward protein engineering approaches allowed construction of a bispecific with VH27.2 and Envafolimab to synergize dual therapies into a single molecule. The bispecific format was more selective for $ENPP1^{+}$/$PD\text{-}L1^{+}$ tumor cells than the monotherapies as separate agents. ENPP1 is also an anti-metastatic target that could be therapeutically leveraged(4–6, 8, 9). For example, OS is a cancer that becomes fatal when the disease progresses to metastasis(62). We showed that our VH inhibitor binds to PDX-derived OS cells with up-regulated ENPP1. As HER2 is also overexpressed in OS, a bifunctional molecule combining ENPP1 inhibitor with second clinical antibody such as

trastuzamab could be another opportunity to dual-target mesenchymal transition pathways and malignant signaling to treat this aggressive cancer.

Finally, ENPP1 biologic inhibitors containing Fc domains or formatted into BiTEs are also antigen-directed immunotherapies. NK cells and macrophages recruited to the TME by cGAMP *trans* signaling will target tumor cells bound with the Fc effector active forms for ADCC. Similarly, we demonstrated that the ENPP1 inhibitor in BiTE format robustly activated T cells. Additionally, VH domains are exceptionally useful because of their stable expression as chimeric antigen receptor-T cells (CAR-Ts). We hypothesize that layering immune cell trafficking with antigen-directed killing could potentiate the therapeutic efficacy of biologic inhibitors of ENPP1 compared to small molecules that have only a single mechanism of action. As the VH inhibitor is cross-reactive with mouse ENPP1, these immunotherapeutic synergies will be evaluated using immunocompetent mice in future studies.

One consideration for ENPP1-directed immunotherapies is that secreted ENPP1 may have a decoy effect preventing immune cells from engaging tumor-bound ENPP1. However, the VH inhibitor was more potent in cell-based assays than in plasma assays suggesting avidity is a factor that intrinsically biases binding to membrane ENPP1 over the monomeric soluble species. Based on our data for the anti-ENPP1/PD-L1 bispecific molecule, bispecific CAR or BiTE modalities might be effective solutions to enhance selectivity to tumor cells.

Inhibition via targeted degradation is another therapeutic approach enabled by the panel of anti-ENPP1 VH. The VH27.2 AbTAC most effectively mediated the ubiquitination of ENPP1 by RNF43. This AbTAC is unique due to the additive effects of functional inhibition and degradation. Previously, AbTACs recognizing multiple known sites on EGFR suggested that epitopes closer to the membrane induced greater degradation, probably due to the relatively short ectodomain of

RNF43(61). Consistently, the cryo-EM structure verified that VH27.2 binds a membrane-proximal epitope on the phosphodiesterase domain. Optimizing AbTAC flexibility, valency, and tertiary complex orientation through basic reformatting can enhance degradation levels, as can co-opting more abundant E3 ligases or cytokine/chemokine receptors (KineTACs)(59, 61). Additionally, KineTACs could be promising for degrading soluble ENPP1 in the TME as the technology does not require a cytosolic domain on the target protein(59). We have focused on inhibiting ENPP1 biochemical activity, however ENPP1 is known to negatively regulate insulin signaling through direct binding to the insulin receptor(36, 37, 40). It is possible that degrading ENPP1 to eliminate this interaction could have therapeutic relevance to insulin resistance and Type 2 diabetes.

We solved the cryo-EM structure of the VH-ENPP1 complex and used mutagenesis to validate interactions and investigate the inhibitory mechanism. There was a significant pi-stacking network engaging CDR H1 Y31 and Y30 and ENPP1 H380 that we predict is affecting catalysis. Based on the substantial role of CDR H3 in blocking ATP but not cGAMP hydrolysis, we suspect that the CDR H1 interaction with H380 is significant to the mechanism of inhibition for cGAMP degradation, as would be consistent with previous reports(3). Excitingly, the structure-function analysis demonstrated that minor perturbations to the VH CDR H3 residues could modulate ENPP1 substrate preferences through a novel mechanism. Y102A and W104F mutants were poor inhibitors of ATP hydrolysis but only slightly affected the K_i of cGAMP relative to WT VH27.2-Fc. With further affinity maturation and optimization the cGAMP-selective VH mutants will be valuable reagents for studying cGAMP biology in cancer and other diseases. The discovery of separate allosteric pockets that decouple ATP and cGAMP hydrolytic mechanisms can aid future designs of small molecule and biologic inhibitors with greater potencies and specialized activities.

Acknowledgements:

We thank Professor Brian Kobilka (Stanford) for generosity with cryo-EM resources and expertise. We thank members of the Wells Lab for their support. We specifically thank K. Schaeffer (UCSF) for her guidance on preparation of the complex for cryo-EM and T. Owens (UCSF) for assistance with mass photometry characterizations. We thank C. Le (UCSF) for her help purifying binders and S. Remesh (UCSF) and K. Leung (UCSF) for their valuable discussions. J.A.W. thanks the NCI P41 CA196276, the Harry and Dianna Hind Professorship, and Bristol Myers Squibb for generous funding. C.C.L. thanks the NCI R01CA260415 for generous funding. E.A.S.C. and E.P.Y. were generously funded by the St. Baldrick's Foundation Fellowship. J.A.C., H.W., and L.L. thank the NIH R01 CA258427 and the Arc Institute for funding. J.A.C. thanks NIH 5F31CA239510 for funding. Part of this work was performed in the Stanford ChEM-H Macromolecular Structure Knowledge Center.

2.5 Materials and Methods

Cell culture

PDX-derived OS384 cells were engineered with plasmid containing safe-guide RNA (SG) or ENPP1 guide RNA (KO). Cells were cultured in DMEM containing 10% FBS, 1x glutamine, and 1% pen/strep at 37^{O}C and 5% CO_2. Jurkat cells expressing NFAT-GFP reporter were cultured in RPMI containing 10% FBS, 1% pen/strep, and 2 mg/mL Geneticin at 37^{O}C and 5% CO2. MDA-MB-231 cells were cultured in DMEM containing 10% FBS and 1% pen/strep at 37C and 5% CO_2. The OS384 PDX-derived and MDA-MB-231 cell lines were validated by STR testing and NFAT-GFP Jurkat cell line was purchased from Thermo.

Mammalian expression of proteins (ENPP1-Fc, VH-Fc, BiTE, AbTAC)

HEK-293 EXPI (Expi293) cells were cultured in Expi293 media (Gibco) at 37^{O}C and 8% humidity with orbital shaking at 250 rpm. ENPP1-Fc or VH-Fc were cloned into pFUSE vector (Invivogen) with upstream IL-2 secretion signal. Cells were transfected at 3M/mL density using Expifectamine Transfection kit (Gibco) according to manufacturer protocols. To biotinylate the AviTag of ENPP1-Fc Expi293 cells expressing BirA were used and 0.05 mM biotin was included in the media at the time of transfection. 72-120h after addition of enhancers the supernatant was harvested (30min, 4000g) and filtered using 0.45 micron filters. Proteins were purified with Protein A affinity chromatography or Nickel resin and buffer exchanged into PBS using appropriate MW spin filters (Amicon). Protein purity was assessed using SDS-page and proteins were stored at -80^{O}C.

Bacterial expression of proteins (single-domain VH)

VH were expressed in E. Coli C43(DE3) Pro+ pTUM+ using optimized autoinduction media. Bacterial pellets were lysed with B-PER (Thermo) containing protease inhibitors (Millipore Sigma) and lysates were purified using Protein A affinity chromatography and buffer exchanged into PBS using 3 or 10 MW spin filters (Amicon). Protein purity was assessed using SDS-page and proteins were stored at -80^{O}C.

Phage Selection with VH-phage library

Phage display using a VH-phagemid library was performed according to previously established protocols(44).

For the standard selection, biotinylated antigen or biotinylated Fc were immobilized to streptavidin-coated magnetic beads (Promega). For each round, the phage library

was first cleared by incubating with Fc to remove non-specific binders, and subsequently the positive selection was performed using the antigen. Phage binding antigen were washed three times and eluted by treatment with 2 ug/mL tobacco etch virus (TEV) protease. XL-1 blue E. Coli were infected with eluted phage and the allowed to propagate overnight. In total four rounds of selection were performed with increasing antigen and clear stringency, as shown in **Figure 1C**. All steps were carried out in TBS buffer containing 0.02% TWEEN-20, 0.2% BSA, 200uM zinc chloride, 2mM calcium chloride, and 75mM sodium chloride. After four rounds, single XL-1 blue colonies were picked and evaluated by ELISA and sanger sequencing.

For the substrate competitive selection, the procedure above was performed but instead of TEV treatment the bound phage were eluted by incubating with 10mM ATP for 30 minutes at room temperature, as shown in **Figure 1D**.

VH maturation via autonomous hypermutation yeast surface display

VH27 was integrated into the AHEAD yeast strain (yAW301) as previously reported(47). VH27 was first subcloned into the pAW240 integration plasmid, linearized via restriction digest, and transformed into chemically competent yAW301 using Frozen-EZ Yeast Transformation II kit (Zymo). After 3 days of growth on selective SC-HLUWMC dropout media (US Biologics) single colonies were grown to saturation in SC-HLUWMC supplemented with 2% glucose. Incorporation of VH27 was validated by sanger sequencing. VH27 was autonomously diversified by passaging transformed yAW301 through 2-3 1000x fold dilutions in SC-HLUW with 2% glucose. For FACS experiments, VH27 expression was induced in yeast by switching to SC-HLUW with 2% galactose for 48 hrs. Yeast were labeled with biotinylated ENPP1-Fc for 1-2 hrs, with round 1 starting at 65 nM and every subsequent round at half the previous concentration. To prevent ligand depletion and allow binding reactions to reach equilibrium, yeast cell counts,

reaction volumes, and incubation times were further adjusted. After washing, yeast were stained with 1000x dilution of anti-HA-AF488 (Thermo) and streptavidin-647 (Thermo), washed again, and subjected to FACS using an Aria II instrument. During each round ~2e7 cells were stained and used to sort out 200-2,000 cells. To avoid selection of mutants with mutations in VH27's HA-tag (fused to VH27 in order to measure display level by anti-HA-AF488) a strict floor on HA signal was set such that only the top ~15% of clones on the HA signal axis were sorted for ENPP1-Fc labeling. Omitting HA-tag mutants was important since these falsely appear as improved ENPP1 binders because they disable the HA-tag display level signal to which the ENPP1-Fc signal is normalized. Cells were sorted into 3 mL of SC-HLUW with 2% glucose, grown to saturation (~3 days), and then subjected to the next round.

Biolayer Interferometry (BLI)

BLI data was collected using an OctetRED384 (ForteBio) instrument. To analyze the association and dissociation kinetics of purified binders, streptavidin biosensor tips (Sartorius) were loaded with antigen, blocked with 5 uM biotin, dipped into protein analyte in solution for 600 seconds (association), and finally dipped into buffer for 900 seconds (dissociation). For epitope binning experiments, biosensor loaded with ENPP1-Fc was blocked with 5 uM biotin, dipped into solution containing 25 nM binder 1 until saturation (600 seconds), and then immediately dipped into solution containing 25 nM binder 1 and 25 nM binder 2 (600 seconds). Experiments for ENPP1 antigen were performed using TBS buffer containing 0.02% TWEEN-20, 0.2% BSA, 200uM zinc chloride, 2mM calcium chloride, and 75mM sodium chloride. All other antigens were assayed using PBS containing 0.02% TWEEN-20 and 0.2% BSA. Data were analyzed using ForteBio Octet analysis software and kinetic parameters were determined based on a 1:1 monovalent binding model.

Flow Cytometry

Cells were lifted with versene, washed PBS, and resuspended in PBS with 3% BSA. Cells were stained with binder at indicated concentrations in PBS with 3% BSA for 1 hr at 4^{O}C. Cells were washed twice with PBS with 3% BSA. Cells were then incubated with ProtA-647 secondary (Thermo) at 1:1000 dilution in PBS with 3% BSA for 30 min at 4^{O}C. Cells were washed three times in PBS with 3% BSA cells and resuspended in PBS for flow cytometry analysis using a Beckman Coulter Cytoflex Flow Cytometer. Data were processed with FlowJo v10.8.1 software, and EC_{50} curves were calculated using GraphPad PRISM 7.0 'Sigmoidal, 4PL'non-linear fit with Hill coefficient set to greater than 1.

Recombinant hENPP1 and mENPP1 Inhibition Assays

WT ENPP1-Fc was cloned and used for recombinant enzyme activity assays. The Michaelis-Menten reaction conditions used were 5 nM WT ENPP1-Fc, 300 nM inhibitor (or PBS), and a titration of 500, 50, 5, or 0.5uM ATP (Thermo) or cGAMP (Invivogen). The reaction buffer was TBS containing 0.02% TWEEN-20, 0.2% BSA, 200 uM zinc chloride, 2 mM calcium chloride, and 75 mM sodium chloride. Every 2 min for a total of 8 min the reactions were quenched by heating to 95^{O}C for 10min. Cell-Titer Glo (Promega) or AMP-Glo (Promega) were performed according to manufacturer protocol to determine amount of ATP remaining or AMP produced from cGAMP hydrolysis. The initial velocity was determined by averaging the velocities calculated over 4-8 min (ATP) and 2-8min (cGAMP) at each substrate concentration. The Michaelis-Menten K_i was analyzed using GraphPad PRISM 7.0 'Enzyme kinetics-Noncompetitive inhibition' model.

To assess single-point inhibition values for alanine and phenylalanine mutants, 5nM WT ENPP1-Fc (or catalytically dead control), 500 nM inhibitor (or PBS), and substrate (ATP = 2.5

mM, cGAMP = 1 mM, pNP-TMP= 1mM) were incubated in reaction buffer at 25^{O}C for 30 min, quenched by heating to 95^{O}C for 10min, and assayed by Cell-Titer Glo (ATP), AMP-Glo (cGAMP), or absorbance at 405 nm (pNP-TMP).

Mouse ENPP1 (mENPP1) was purified as previously described(2, 40). 10 nM mENPP1 and 500 nM VH27/T75I/A98I-Fc/Fc isotype/PBS was incubated with 2.5 mM ATP or 1 mM cGAMP in reaction buffer at 25^{O}C for 30 min. Reactions were quenched by heating at 95^{O}C for 10min and ENPP1 activity was measured by Cell-Titer Glo (ATP) or AMP Glo (cGAMP).

Human and Mouse Recovered Plasma IC_{50} Assay

Recovered human plasma (sodium heparin anti-coagulant) from three donors was purchased from ZenBio (Donor 1:031620A, Donor 2:PL070720AC, Donor 3:PL070720X). Plasma from three male C57BL/6J mice was prepared with sodium heparin anti-coagulant as previously described(2). Final reactions were 10 uL and contained 65% plasma, 1mM cGAMP, and inhibitor or control molecule at indicated concentration. A reaction without cGAMP was used as a control to subtract baseline AMP signal. Reactions were incubated for 90 min (or 24 hr when specified). Samples were diluted 10-fold in PBS and either measured immediately or quenched and stored for later analysis by centrifuging in a 10 MW spin filter. AMP produced through cGAMP hydrolysis was measured using AMP-Glo assay. Values were corrected by subtracting the background signal of plasma without supplemented cGAMP and data were normalized to the PBS condition. IC_{50} value for each donor was analyzed using GraphPad PRISM 7.0 'Dose-response-Inhibition (four parameters)'.

Differential Scanning Fluorimetry (DSF)

Purified VH protein was diluted to 1 uM in PBS buffer containing 4x Sypro Orange (Invitrogen). BME was supplemented to 6.25% final dilution for samples assayed in reducing conditions. Samples were heated from 30^{O}C to 95^{O}C with 0.3C/30 second ramp rate and fluorescent emissions at 490 nm and 575 nm were continuously recorded. Roche LC480 LightCycler and associated software were used for data collection and T_m calculations. Two to four technical replicates were analyzed for N=4 independent replicates.

Size Exclusion Chromatography (SEC)

SEC was performed using an Agilent HPLC 1260 Infinity II LC System and either AdvanceBio column (300A, 2.7 um, Agilent) or TSKgel SuperSW mAb HTP column (4 um, Tosoh Biosciences). Fluorescence was detected using excitation 285 nm and emission 340 nm.

Extracellular cGAMP IC_{50} ELISA

MDA-MB-231 cells were plated at 2K cell/well 24 hr before cell treatments. Assay was performed in serum-free DMEM/F-12 media that contains zinc sulfate. Cells were washed with media and resuspended in media containing the inhibitor (or Fc isotype or PBS) and allowed to incubate for 5 min before cGAMP was added at a final concentration of 50 uM. cGAMP was also added to a well containing only media without cells as a maximum concentration control. Cells were placed at 37^{O}C, 5% CO_2 for 12 hr. To harvest, 2 uL of media was diluted 50-fold in PBS and centrifuged in a 10 MW spin filter. To assay cGAMP remaining in the media by cGAMP ELISA (Cayman Chemical), the sample was diluted another 75x using Immunoassay Buffer-C (Cayman Chemical) and the ELISA was performed according to the manufacturer protocol. The level of cGAMP remaining in each sample was normalized to the range between the PBS control (full

enzymatic activity) and cGAMP in media without cells (no enzymatic activity). Data were analyzed using GraphPad PRISM 7.0 'Dose-response-Inhibition (four parameters)'. For the bi-paratopic molecule the 3 uM concentration was excluded from the IC_{50} calculation.

Extracellular pNP-TMP IC_{50} Assay

MDA-MB-231 cells were plated at 2K cell/well 36 hr before cell treatments. Assay was performed in serum-free and phenol red-free DMEM/F-12 media. Cells were washed with media and resuspended in media containing the inhibitor (or Fc isotype or PBS) and incubated for 10 min. pNP-TMP substrate (Sigma Aldrich) was added at a final concentration of 200uM. Cells were placed at 37^{O}C and 5% CO_2 for 5 hr and absorbance at 405 nm was measured. Data were normalized using the PBS treatment. Data were analyzed using GraphPad PRISM 7.0 'Dose-response-Inhibition (four parameters)'. For the bi-paratopic molecule the 3 uM concentration was excluded from the IC_{50} calculation.

NFAT-GFP Jurkat Assay

Jurkat cells expressing NFAT-GFP reporter were used to measure T cell activation with BiTE treatments. Streptavadin coated magnetic beads (Promega) were incubated with 0, 10, or 100 nM ENPP1-Fc antigen for 30 min at room temperature followed by three washes. In each assay well, 50K Jurkat NFAT-GFP cells were plated in serum-free RPMI and treated with 20 uL of beads and 10 nM BiTE. Conditions with no beads and without BiTE (PBS) were included for controls. After incubating for 20 hr at 37^{O}C and 5% CO_2 magnetic beads were removed and cellular GFP expression was analyzed by flow cytometry.

AbTAC

8K MDA-MB-231 cells were plated in 48-well culture plates and incubated at 37^{O}C for 24 hr. Cells were treated with the indicated concentration of AbTAC or control molecule in serum-free DMEM/F12 media and incubated at 37^{O}C for 24 hr. Cells were washed with PBS and lysates were harvested with RIPA (Sigma Aldrich) containing protease inhibitor. Samples for gel electrophoresis were prepared by boiling lysate in NuPAGE loading dye containing BME. Proteins were transferred from the gel to a PVDF membrane using iBlot reagenets and instrument (Thermo). Membranes were blocked and subsequently stained with anti-ENPP1 antibody (Abcam 223268) and anti-Actin antibody (Santa Cruz Biotechnologies) at 1:1000 dilutions at 4^{O}C overnight. Membranes were then stained with LICOR secondary antibodies (Goat anti-Rat 680 and Goat anti-Mouse 800) at 1:5000 dilutions for 1 hr at room temperature and imaged using the LICOR Odyssey instrument.

Structural sample preparation, data collection, and processing

T256A ENPP1-Fc and 10x VH27/T75I/A89V were incubated at 4°C for 1 hr. The complex was injected onto an Äkta Pure system (GE Healthcare) and the peak was isolated by SEC using a Superdex 200 Increase 10/300 GL column (**Supplemental Figure 2.S4**). Presence of both VH and antigen in the eluted peak was confirmed by SDS-PAGE gel (**Supplemental Figure 2.S4**). Stoichiometry of the complex was characterized by Refeyn mass photometry (**Supplemental Figure 2.S4**).

For cryo-EM grids preparation, 2 mg/ml T256A ENPP1-Fc was mixed with 10X VH27/T75I/A89V and the mixture was directly applied to glow-discharged 300 mesh gold grids (Quantifoil R1.2/1.3) and vitrified using a FEI Vitrobot Mark IV (Thermo Fisher Scientific). Data were collected on a Titan Krios (SLAC/Stanford) operated at 300 keV using a Gatan K3 direct

electron detector in counting mode, with 0.8677 Å pixel size. A total of 4426 movies were obtained. Each stack movie was recorded for a total of 2.5 s with 0.05 s per frame. The dose rate was 1.14 electrons/Å^2/subframe, resulting in an accumulated dose of 57 electrons per Å^2. The data were collected using SerialEM(63).

Data processing was done in cryosparc(64). Dose-fractionated movies were subjected to beam-induced motion correction followed by CTF parameters estimation. After that, 3414 movies with CTF fit better than 4Å were selected. Particle autopicking, 2D classification, and 3D refinements were performed in cryosparc. The autopicked particles were first subjected to 2D classification, 2D classes that look like protein complex were selected for ab initio reconstruction and heterogenous refinement. The best 3D class (highest estimated resolution and good orientation distribution) were selected and the particles are subjected to non-uniform refinement(65). This generated a 3.2A resolution map for AMP bound ENPP1-VH complex.

Table 2. 1 The following parameters were used for data collection and processing:

	VH-T256A ENPP1 complex
Data collection/processing	
Magnification	130,000
Voltage (kV)	300
Electron exposure (e–/Å^2)	57

Defocus range (μm)	0.7-2
Pixel size (Å)	0.8677
Symmetry imposed	C2
Initial particle images (no.)	
Final particle images (no.)	
Map resolution (Å)	3.2
FSC threshold	0.143
Map resolution range (Å)	
Refinement	
Initial model used (PDB code)	
Model resolution (Å)	3.2
FSC threshold	0.143
Model resolution range (Å)	2.9-3.4
Map sharpening *B* factor ($Å^2$)	
Model composition	
Non-hydrogen atoms	8739
Protein residues	1122
Ligands	1
B factors ($Å^2$)	
Protein	60.76
Ligand	78.28
R.m.s. deviations	
Bond lengths (Å)	0.004
Bond angles (°)	0.566
Validation	
MolProbity score	1.72
Clashscore	8.03
Poor rotamers (%)	0
Ramachandran plot	
Favored (%)	95.93
Allowed (%)	4.07
Disallowed (%)	0

2.6 Main Figures

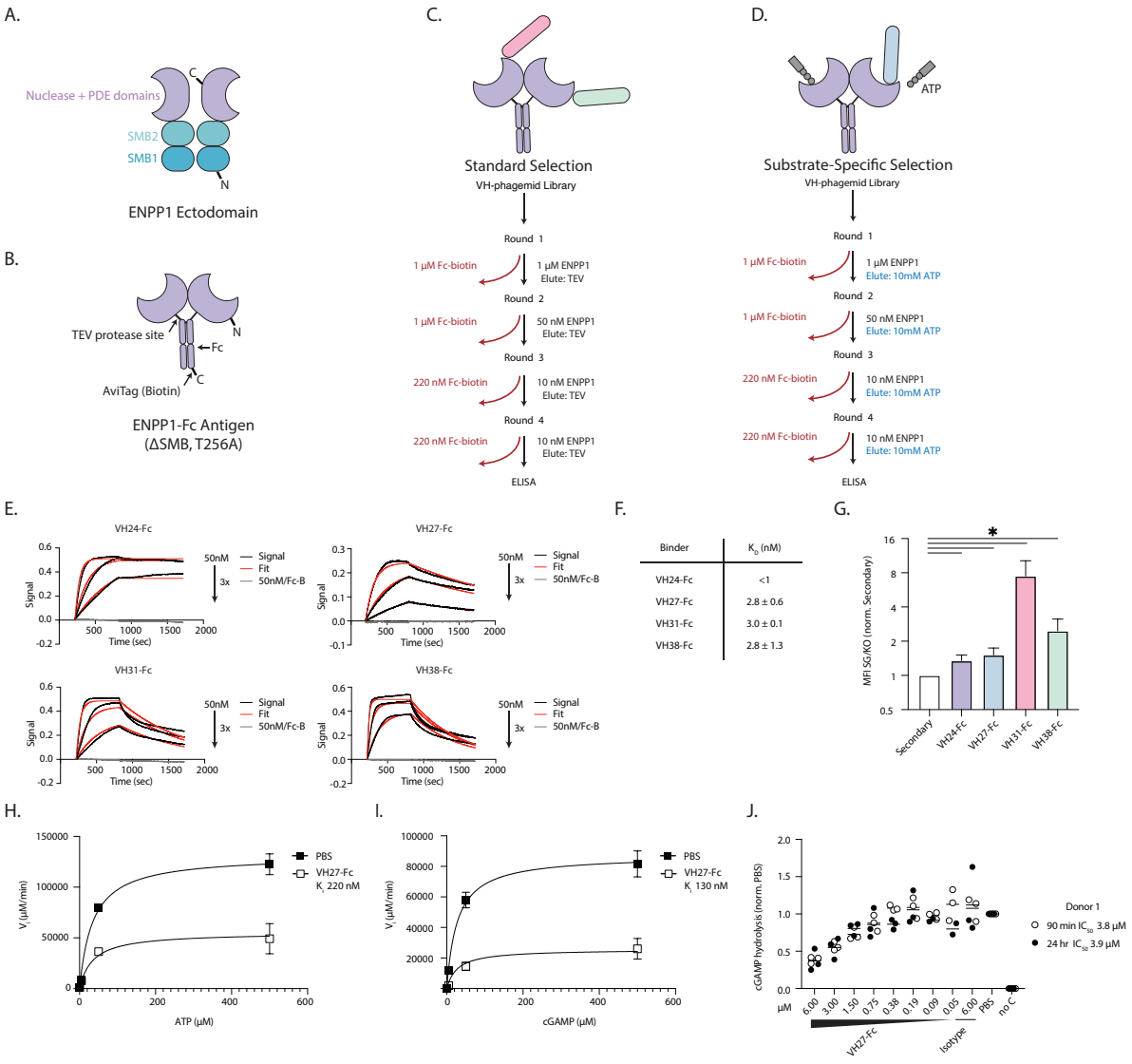

Figure 2. 1 Phage-display generated high affinity VH domains recognizing native ENPP1 on PDX-derived osteosarcoma cells, and VH27 inhibited ATP and cGAMP hydrolysis.

A. Structure of extracellular domain of human ENPP1. **B.** Recombinant ENPP1 C-terminal Fc fusion antigen for phage-display. ENPP1 ectodomain was modified by truncating SMB1 and SMB2 domains and mutating the catalytic threonine to alanine. Fc-fusion included an Avi tag for biotinylation and a TEV protease site. **C,D.** Schema of phage-display selection rounds. VH-phagemid library underwent four rounds of negative (Fc-biotin) and positive (ENPP1-Fc) selection with increasing stringency. To elute, bound phage were released by TEV protease treatment **(C)** or eluted using 10mM ATP substrate **(D)**. **E.** Representative biolayer interferometry signals and fits for each VH-Fc binding ENPP-Fc antigen or Fc-biotin control (no signal). **F.** Table of K_D

values measured by biolayer interferometry for VH-Fc panel (N=2). **G.** On-cell binding was tested using PDX-derived OS384 cell line engineered with ENPP1 knockout (KO) or safe-guide (SG). KO and SG cells were stained with 50nM of binder and median fluorescent signal was analyzed by flow cytometry. The bar graph reports the mean and SEM of the fold-change (SG/KO) in signal (N=3 or 4 independent replicates). Statistics were calculated using one-tailed Student's t-test. **H, I.** Michaelis-Menten kinetics were determined for VH27-Fc inhibitor using recombinant Fc-ENPP1 and ATP **(H)** or cGAMP **(I)** substrates (N=3, mean and standard deviation). **J.** VH27-Fc inhibited secreted ENPP1 in *ex vivo* plasma supplemented with 1mM cGAMP over 90 min and 24 hr time courses. Fc isotype treatment and condition with no cGAMP added (No cGAMP) were included as controls (N=3 for Donor 1).

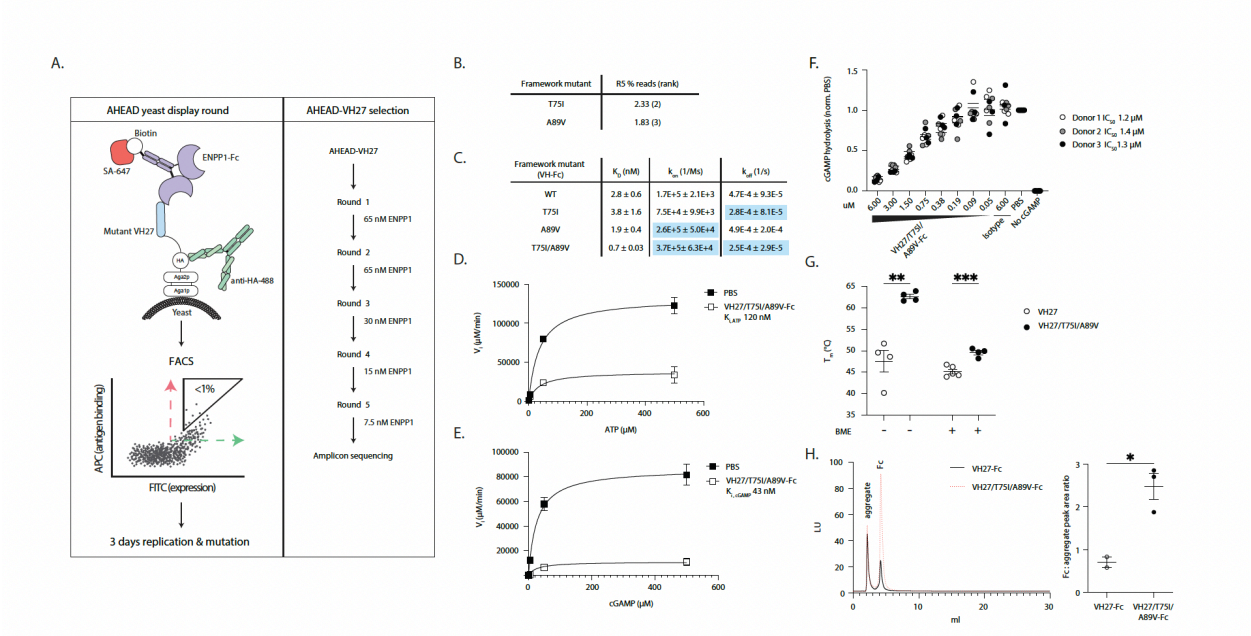

Figure 2. 2 Affinity maturation of VH27 improved affinity, stability, and inhibitory potency.

A. Yeast display coupled with *in cellulo* continuous diversification was performed using the AHEAD hypermutation yeast strain. Yeast populations expressing mutated VH27 were stained with ENPP1-Fc and anti-HA antibody and FACS sorted for optimal antigen binding and stable expression. Five selection rounds of increasing antigen stringency were performed and the final population was amplicon sequenced by NGS. **B.** T75I and A89V framework mutations were ranked 2 and 3 respectively, with read frequencies over 1%. **C.** VH27/T75I-Fc mutant had improved dissociation rate and VH27/A89V-Fc mutant had enhanced association rate. The VH27/T75I/A89V-Fc double mutant retained both kinetic gains and had sub-nanomolar K_D (N=2, mean and standard deviation). **D,E.** Michaelis-Menten kinetic analysis for VH27/T75I/A89V- for ATP (**D**) and cGAMP (**E**) (N=3, mean and standard deviation). **F.** Dose titration of VH27/T75I/A89V-Fc or indicated control molecules were tested for *ex vivo* ENPP1 inhibition in human plasma supplemented with 1 mM cGAMP for 90 min. Fc isotype treatment and condition with no cGAMP added (No cGAMP) were included as controls (N=3 for each donor). **G.** Differential scanning fluorimetry was used to measure melting temperature of VH27 (WT) versus the double mutant (VH27/T75I/A89V) as single-domain VHs in non-reducing and reducing (6.25% BME) conditions. Bar graph reports mean and SEM for N=4 or 5 biological replicates and statistics were calculated using two-tailed Student's t-test. **H.** SEC traces were analyzed for peak area ratios between aggregate peak and Fc peak (N= 2 or 3). Bar graph reports mean and SEM for N=2 or 3 biological replicates and statistics were calculated using two-tailed Student's t-test.

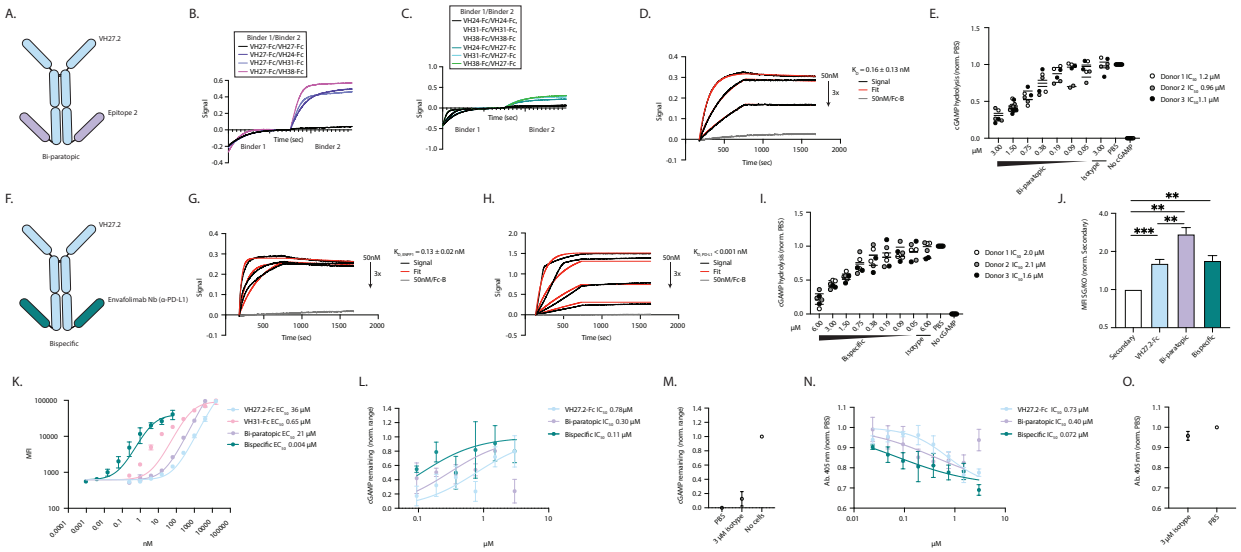

Figure 2. 3 VH27.2 was ported into bi-paratopic and bispecific formats driving improved localization to tumor cells and stronger inhibition of ENPP1 on cell membranes.

A. Structure of bi-paratopic tetravalent Fc inhibitor recognizing inhibitory VH27.2 epitope and a second non-overlapping epitope on ENPP1. **B,C.** Biolayer interferometry was used to map the epitopes of the VH panel with respect to the VH27 epitope. VH24-Fc, VH31-Fc, and VH38-Fc could bind ENPP1 after VH27-Fc was pre-loaded on the sensor (**B**), and VH27-Fc could bind ENPP1 after VH24-Fc, VH31-Fc, or VH38-Fc were pre-loaded on the sensor (**C**). **D.** Representative biolayer interferometry signals and fits for bi-paratopic VH27.2-VH31 inhibitor binding ENPP1-Fc antigen or Fc-biotin control (no signal). K_D was measured to be sub-nanomolar (N=2, mean and standard deviation). **E.** Bi-paratopic molecule inhibited ENPP1 in human plasma (1mM cGAMP, 90 min). Fc isotype treatment and condition with no cGAMP added (No cGAMP) were included as controls (N=2 for each donor). **F.** Structure of bispecific tetravalent Fc ENPP1 inhibitor combined with the PD-L1 checkpoint inhibitor Envafolimab. **G,H.** Representative biolayer interferometry signals and fits for bispecific inhibitor binding ENPP1-Fc antigen (**G**) or PDL1-Fc antigen (**H**), with no signal observed for Fc-biotin controls. K_D values were measured to be sub-nanomolar for both ENPP1 and PDL1 (N=2, mean and standard deviation). **I.** Bispecific molecule inhibited ENPP1 in human plasma (1mM cGAMP, 90 min). Fc isotype treatment and condition with no cGAMP added (No cGAMP) were included as controls (N=2 for each donor). **J.** OS384 KO and SG cells were stained with 50nM of binder and median fluorescent signal was analyzed by flow cytometry. The bar graph reports the mean and SEM of the fold-change (SG/KO) in signal (at least N=5 biological replicates). Statistics were calculated using one-tailed Student's t-test. **K.** MDA-MB-231 cells were stained with a titration for VH27.2-Fc, VH31-Fc, bi-paratopic VH27.2-VH31, and bispecific VH27.2-Envafolimab and EC_{50} values were fitted. Data represent mean and SEM for N=2 biological replicates. **L.** MDA-MB-231 cells were treated with 50 uM cGAMP and the indicated concentration of VH27.2-Fc, bi-paratopic inhibitor, or bispecific inhibitor. After 12 hr cell media was harvested and remaining cGAMP was measured using a cGAMP ELISA. Data were normalized to the range between the cGAMP in media treated without cells and cells treated with PBS shown in **M**. Fc isotype treated at 3 uM was included as a control and data are reported in **M**. **N.** MDA-MB-231 cells were treated with 200 uM pNP-TMP and the

indicated concentration of VH27.2-Fc, bi-paratopic inhibitor, or bispecific inhibitor. After 5 hr absorbance at 405nM was measured. Data were normalized to the PBS condition presented in **O**. Fc isotype treated at 3 uM was included as a control and data are reported in **O**. Data in **L-O** represent mean and SEM for N = 3-5 biological replicates.

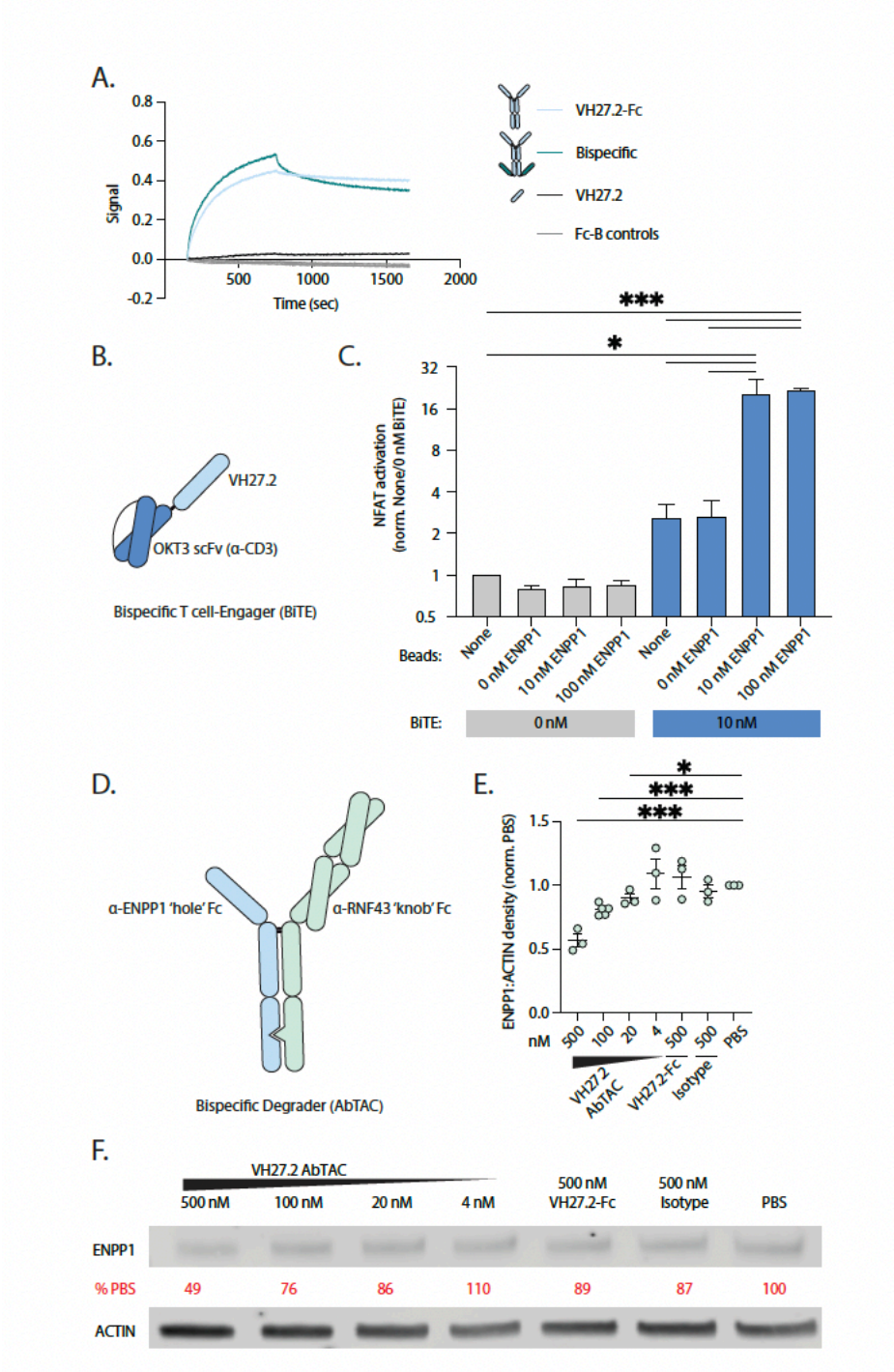

Figure 2. 4 Recombinant engineering of VH inhibitor into immunotherapies and targeted protein degraders.

A. Representative biolayer interferometry signals for 50 nM bivalent VH27.2-Fc, tetravalent bispecific Fc, and single domain VH27.2 (no Fc) binding to CD16-Fc antigen or Fc-biotin control (N=2). **B.** Structure of bispecific T cell engager (BiTE) combining VH27.2 with arm recognizing CD3 (OKT3 scFv) in a linked tandem format. **C.** Jurkat cells expressing NFAT-GFP reporter were

incubated with beads coated with 0, 10, or 100nM Fc-ENPP1 or a no bead control, and were treated with 10 nM BiTE or PBS control. After 20 hr GFP expression driven by NFAT activation was measured by flow cytometry. Data were normalized to the no bead/no BiTE condition. Bar graph reports mean and SEM for N=3 biological replicates. Statistics were calculated using two-tailed Student's t-test. **D.** Structure of 'knob-into-hole' bispecific AbTAC degrader combining anti-ENPP1VH with RNF43-recruiting IgG arm. **E, F.** MDA-MB-231 cells were treated with PBS or a dose titration (500, 100, 20, 4 nM) of VH27.2 AbTAC and ENPP1 levels were measured by immunoblot. Cells were also treated with 500 nM VH27.2-Fc and Fc isotype controls. ENPP1 densities were normalized to Actin loading control. The percent of ENPP1 remaining relative to the PBS treatment was calculated. The graph summarizes the mean and SEM for N=3-5 biological replicates (**E**) and a representative immunoblot for one experiment is shown (**F**).

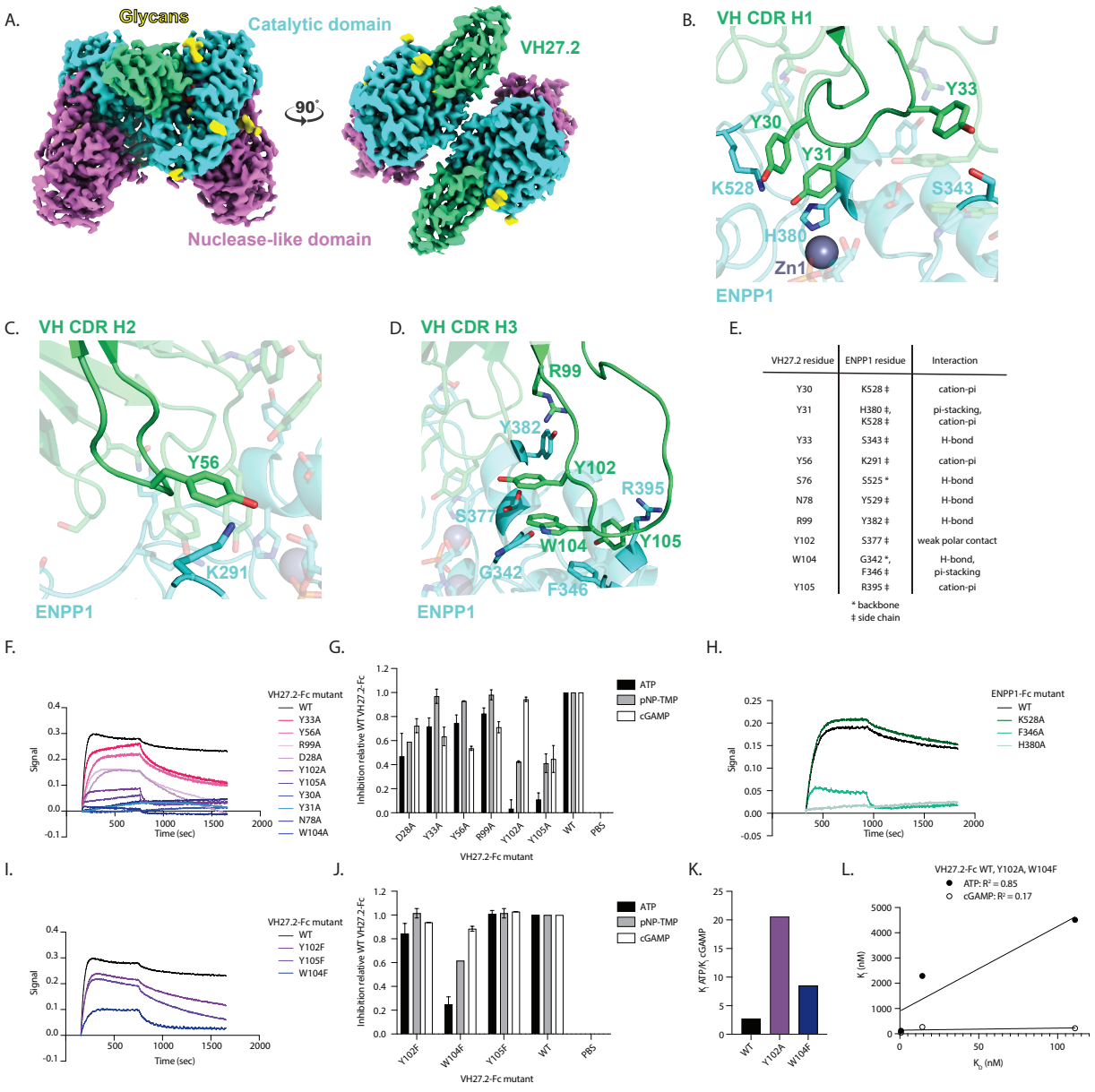

Figure 2. 5 Cryo-EM reveals VH binding ENPP1 proximal to the catalytic site.

A. Cryo-EM 3D reconstruction of VH27.2 bound to ENPP1 ectodomain. **B.** View of the CDR H1 epitope. **C.** View of the CDR H2 epitope. **D.** View of the CDR H3 epitope. **E.** Table summarizing interactions between VH and ENPP1 residues. **F.** Biolayer interferometry comparing binding kinetics of VH27.2-Fc alanine mutants at 25 nM. Traces are representative of two experiments. **G.** Inhibitory potencies of VH27.2-Fc alanine mutants relative to WT VH27.2-Fc treated at 500 nM for ATP, pNP-TMP, and cGAMP substrates. Bar graph reports mean and SEM for two biological replicates. **H.** Biolayer interferometry comparing affinity of VH27.2-Fc to WT, K528A, F346A, and H380A ENPP1. Traces are representative of two independent experiments. **I.** Biolayer

interferometry comparing binding kinetics of VH27.2-Fc phenylalanine mutants at 25nM. Traces are representative of two independent experiments. **J.** Inhibitory potencies of VH27.2-Fc phenylalanine mutants relative to WT VH27.2-Fc treated at 500 nM for ATP, pNP-TMP, and cGAMP substrates. Bar graph reports mean and SEM for two independent replicates. **K.** ATP/cGAMP K_i fold-change value for WT, Y102A, and W104F VH27.2 -Fc. **L.** Linear regression and R^2 values correlating K_D and K_i values for ATP and cGAMP substrates for WT, Y102A, and W104F VH27.2-Fc mutants.

2.7 Supplemental Figures

A.

Binder	H1	H2	H3
VH24	AIYYYDI	RISPYSGSTY	AHWDGYGYVDDWVAI
VH27	DIYYSYYI	RISPSYGSTS	FAYPWYVADDAL
VH31	DIYYSEI	RISPYYGSTS	FDPYHYFSDYYGI
VH38	AIYSYEI	RISPYSSSTY	FWGPWFSSAL

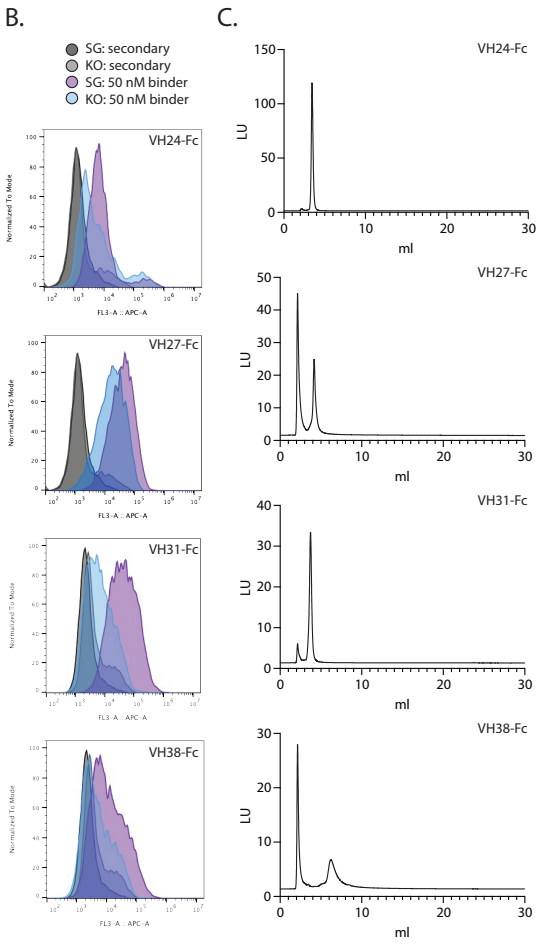

Figure 2.S 1 Sequences, cellular binding, and stability of VH panel.

A. CDR H1-3 sequences for VH panel. B. Representative flow cytometry histograms used to generate bar graph summarizing fold-changes for binding to OS384 SG and KO in Figure 1G. C. SEC traces for VH24-Fc, VH27-Fc, VH31-Fc, and VH38-Fc.

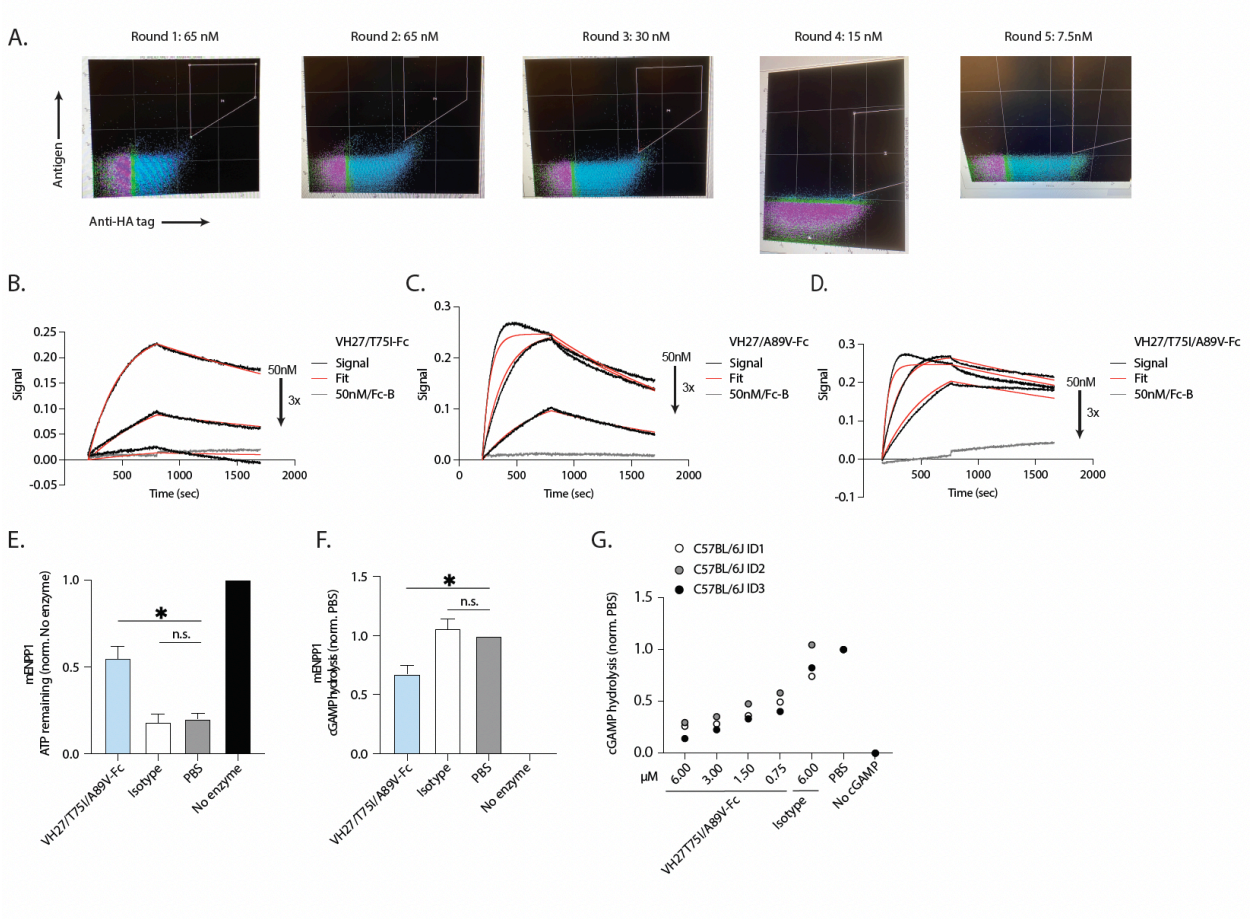

Figure 2.S 2 AHEAD yeast display campaign to affinity mature VH27.

A. FACS gating used for sorting less than 1% AHEAD yeast cell population based on expression (HA tag) and antigen binding. In round 4 the fluorophores were switched (SA-488 and anti-HA-647). **B-D.** Biolayer interferometry signals and fits to determine K_D, $k_{association}$, and $k_{dissociation}$ for VH27-Fc with scaffold mutations T75I (**B**), A89V (**C**), and T75I/A89V (**D**). Data are representative of two experiments. **E,F.** Mouse ENPP1 (mENPP1) was treated with 500 nM VH27/T75I/A89V-Fc, Fc isotype, or PBS to evaluate cross-reactivity for ATP (**E**) and cGAMP (**F**) substrates (N=3 biological replicates for each substrate). Bar graph reports mean and SEM and statistics were calculated using two-tailed Student's t-test. **G.** Dose titration of VH27/T75I/A89V-Fc or indicated controls were tested for *ex vivo* ENPP1 inhibition in C57BL/6J mouse plasma supplemented with 1 mM cGAMP for 90 min (N=3 mice, 1 experiment per mouse).

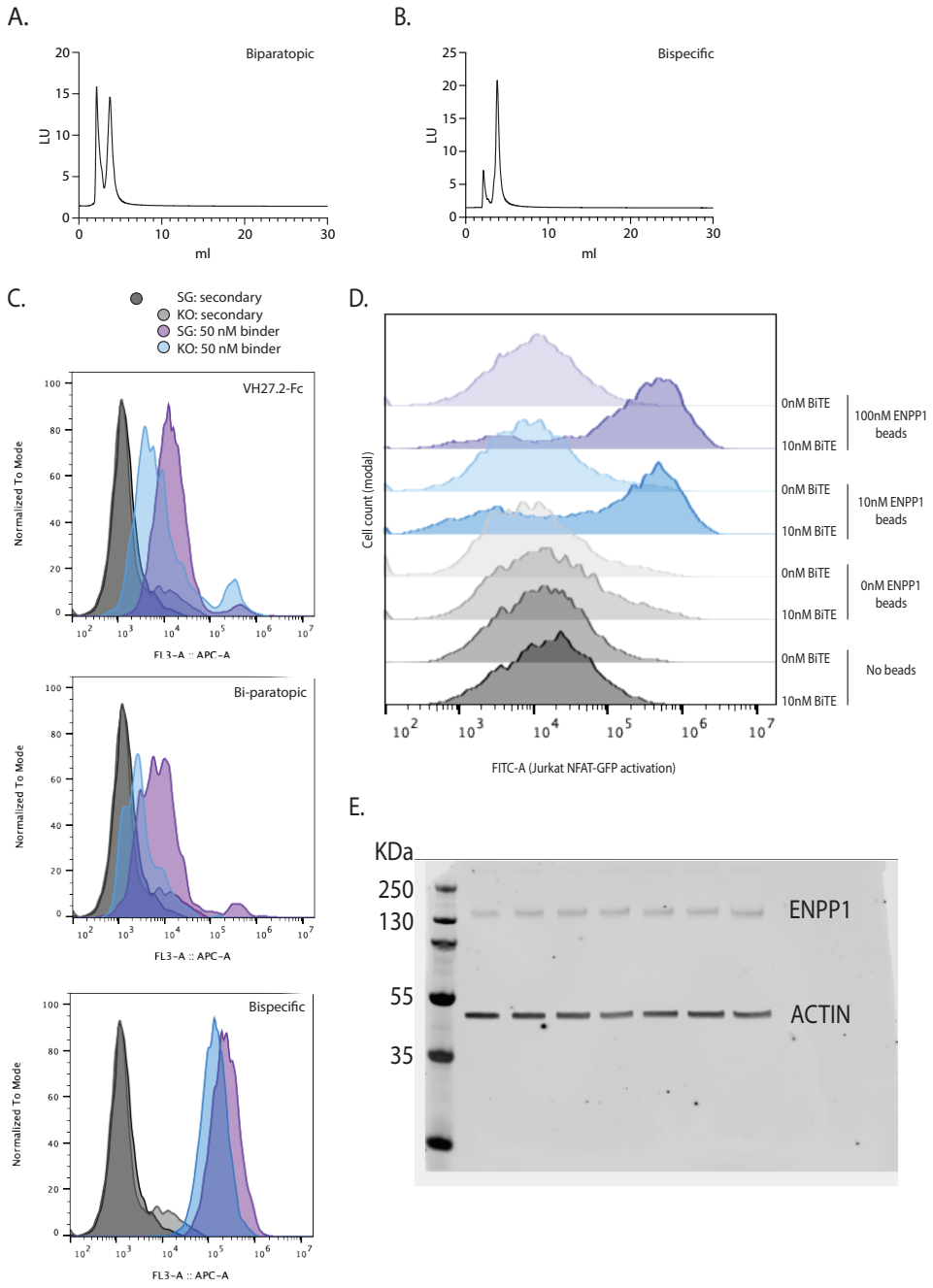

Figure 2.S 3 Additional data for multivalent constructs.

A,B. SEC traces for bi-paratopic inhibitor (**A**) and bispecific inhibitor (**B**). **C.** Representative flow cytometry histograms used to generate bar graph summarizing fold-changes for binding to OS384 SG and KO in **Figure 3J**. **D.** Representative flow cytometry histograms for NFAT-GFP Jurkat activation assays when treated with indicated concentrations of ENPP1-coupled beads or no beads and 10 nM BiTE or PBS. **E.** Unformatted immunoblot with visible ladder used for image in **Figure 4F**.

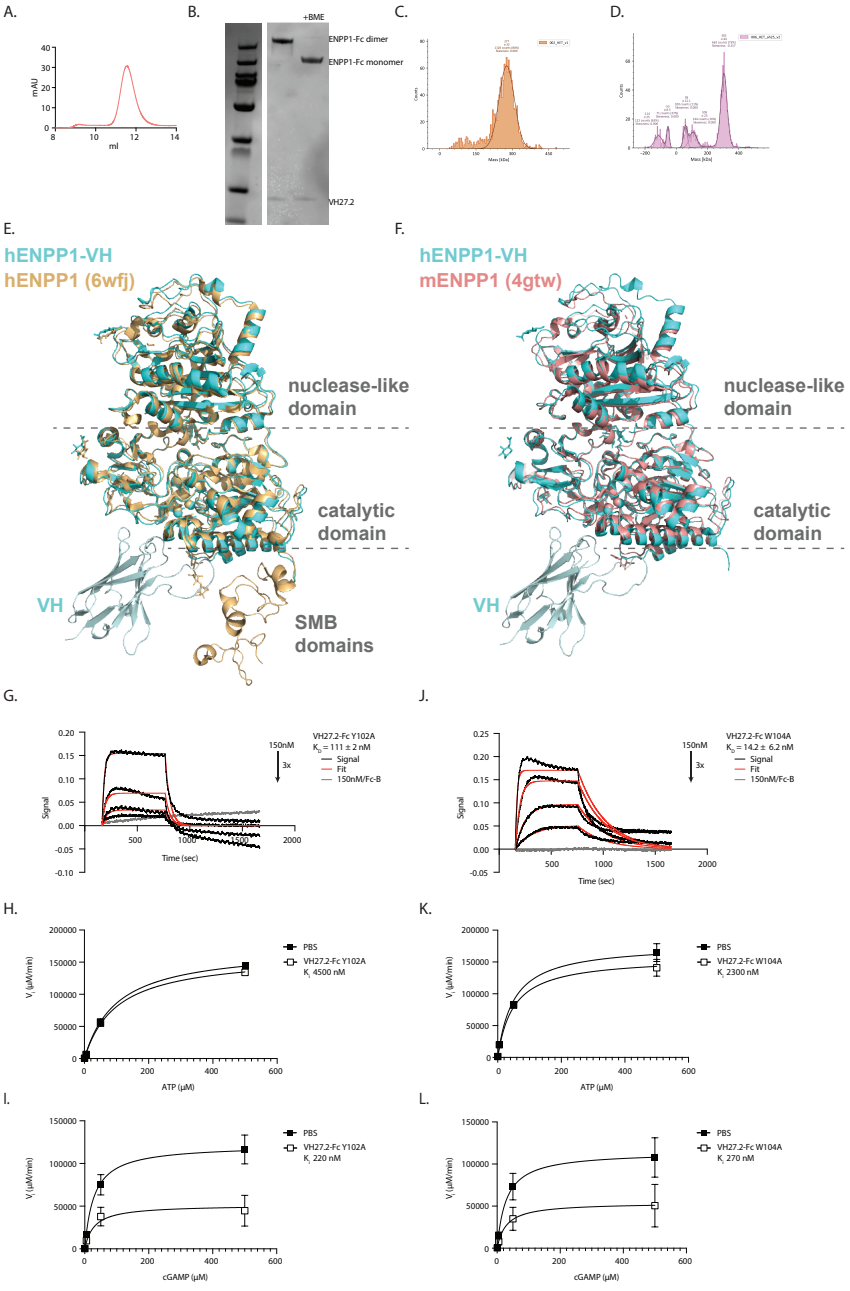
A.
B.
C.
D.
+BME
ENPP1-Fc dimer
ENPP1-Fc monomer
VH27.2
E.
hENPP1-VH
hENPP1 (6wfj)
nuclease-like domain
catalytic domain
VH
SMB domains
F.
hENPP1-VH
mENPP1 (4gtw)
nuclease-like domain
catalytic domain
VH
G.
J.
H.
K.
I.
L.
PBS
VH27.2-Fc Y102A
VH27.2-Fc W104A
Signal
Fit
150nM/Fc-B
Time (sec)
ATP (μM)
cGAMP (μM)

Figure 2.S 4 Additional data for cryo-EM and structure-guided VH CDR mutants.

A-D. Validation of VH-ENPP1 complex. Complex was purified by SEC (**A**) and co-elution of VH and ENPP1-Fc was analyzed by SDS-PAGE gel (**B**). Mass photometry of antigen alone (**C**) and SEC-eluted complex peak (**D**) demonstrated mass shift of approximately 30 KDa suggesting 2:1 VH:antigen stoichiometry. **E.** Parameters for cryo-EM data collection and data refinement. **F.** Cryo-EM structure of VH-ENPP1 complex aligned to PDB 6wjf. **G.** Cryo-EM structure of VH-ENPP1 complex aligned to PDB 4gtw. **H.** Representative biolayer interferometry signals and fits for VH27.2-Fc Y102A (N=2, mean and standard deviation). **I,J.** Michaelis-Menten kinetic analysis for VH27.2-Fc Y102A for ATP (**I**) and cGAMP (**J**) (N=2, mean and standard deviation). **K.** Representative biolayer interferometry signals and fits for VH27.2-Fc W104A (N=2, mean and standard deviation). **L,M.** Michaelis-Menten kinetic analysis for VH27.2-Fc W104A for ATP (**L**) and cGAMP (**M**) (N=2, mean and standard deviation).

2.8 References

1. J. A. Carozza, et al., Extracellular cGAMP is a cancer-cell-produced immunotransmitter involved in radiation-induced anticancer immunity. Nat. Cancer 1, 184–196 (2020).

2. J. A. Carozza, et al., Structure-Aided Development of Small-Molecule Inhibitors of ENPP1, the Extracellular Phosphodiesterase of the Immunotransmitter cGAMP. Cell Chem. Biol. 27, 1347-1358.e5 (2020).

3. J. A. Carozza, et al., ENPP1's regulation of extracellular cGAMP is a ubiquitous mechanism of attenuating STING signaling. Proc. Natl. Acad. Sci. 119, e2119189119 (2022).

4. J. Li, et al., Metastasis and Immune Evasion from Extracellular cGAMP Hydrolysis. Cancer Discov. 11, 1212–1227 (2021).

5. W. M. Lau, et al., Enpp1: A Potential Facilitator of Breast Cancer Bone Metastasis. PLoS ONE 8, e66752 (2013).

6. A. Goswami, et al., AVA-NP-695 Selectively Inhibits ENPP1 to Activate STING Pathway and Abrogate Tumor Metastasis in 4T1 Breast Cancer Syngeneic Mouse Model. Molecules 27, 6721 (2022).

7. M. Hu, et al., Dysregulated ENPP1 increases the malignancy of human lung cancer by inducing epithelial-mesenchymal transition phenotypes and stem cell features. Am. J. Cancer Res. 9, 134–144 (2019).

8. H. Cheng, et al., Activation of STING by cGAMP Regulates MDSCs to Suppress Tumor Metastasis via Reversing Epithelial-Mesenchymal Transition. Front. Oncol. 10, 896 (2020).

9. T. Li, et al., Antitumor Activity of cGAMP via Stimulation of cGAS-cGAMP-STING-IRF3 Mediated Innate Immune Response. Sci. Rep. 6, 19049 (2016).

10. L. Li, et al., Hydrolysis of 2′3′-cGAMP by ENPP1 and design of nonhydrolyzable analogs. Nat. Chem. Biol. 10, 1043–1048 (2014).

11. M. Gangar, et al., Design, synthesis and biological evaluation studies of novel small molecule ENPP1 inhibitors for cancer immunotherapy. Bioorganic Chem. 119, 105549 (2022).

12. X. Wang, X. Lu, D. Yan, Y. Zhou, X. Tan, Development of Novel Ecto-Nucleotide Pyrophosphatase/Phosphodiesterase 1 (ENPP1) Inhibitors for Tumor Immunotherapy. Int. J. Mol. Sci. 23, 7104 (2022).

13. S. Kim, et al., Abstract LBA009: Orally available ENPP1 inhibitor, TXN10128, restores STING activation in tumor microenvironment and confers anti-tumor responses in combination with immune checkpoint blockade. Mol. Cancer Ther. 20, LBA009–LBA009 (2021).

14. J. Baird, et al., "MV-626, a potent and selective inhibitor of ENPP1 enhances STING activation and augments T-cell mediated anti-tumor activity in vivo." (2018). (2018).

15. L. Corrales, V. Matson, B. Flood, S. Spranger, T. F. Gajewski, Innate immune signaling and regulation in cancer immunotherapy. Cell Res. 27, 96–108 (2017).

16. S.-R. Woo, L. Corrales, T. F. Gajewski, Innate Immune Recognition of Cancer. Annu. Rev. Immunol. 33, 445–474 (2015).

17. M. B. Fuertes, et al., Host type I IFN signals are required for antitumor CD8+ T cell responses through CD8α+ dendritic cells. J. Exp. Med. 208, 2005–2016 (2011).

18. S. J. Luen, P. Savas, S. B. Fox, R. Salgado, S. Loi, Tumour-infiltrating lymphocytes and the emerging role of immunotherapy in breast cancer. Pathology (Phila.) 49, 141–155 (2017).

19. P. García-Teijido, M. L. Cabal, I. P. Fernández, Y. F. Pérez, Tumor-Infiltrating Lymphocytes in Triple Negative Breast Cancer: The Future of Immune Targeting. Clin. Med. Insights Oncol. 10s1, CMO.S34540 (2016).

20. J. A. Seidel, A. Otsuka, K. Kabashima, Anti-PD-1 and Anti-CTLA-4 Therapies in Cancer: Mechanisms of Action, Efficacy, and Limitations. Front. Oncol. 8, 86 (2018).

21. J. R. Quesada, M. Talpaz, A. Rios, R. Kurzrock, J. U. Gutterman, Clinical toxicity of interferons in cancer patients: a review. J. Clin. Oncol. 4, 234–243 (1986).

22. S. Sleijfer, M. Bannink, A. R. Gool, W. H. J. Kruit, G. Stoter, Side Effects of Interferon-α Therapy. Pharm. World Sci. 27, 423–431 (2005).

23. F. Meric-Bernstam, et al., Phase I Dose-Escalation Trial of MIW815 (ADU-S100), an Intratumoral STING Agonist, in Patients with Advanced/Metastatic Solid Tumors or Lymphomas. Clin. Cancer Res. 28, 677–688 (2022).

24. K. J. Harrington, et al., Preliminary results of the first-in-human (FIH) study of MK-1454, an agonist of stimulator of interferon genes (STING), as monotherapy or in combination with pembrolizumab (pembro) in patients with advanced solid tumors or lymphomas. Ann. Oncol. 29, viii712 (2018).

25. T. Shree, et al., A Phase I/II Trial of Intratumoral CpG, Local Low-Dose Radiation, and Oral Ibrutinib in Patients with Low-Grade B-Cell Lymphoma. Blood 134, 2825–2825 (2019).

26. L. Motedayen Aval, J. E. Pease, R. Sharma, D. J. Pinato, Challenges and Opportunities in the Clinical Development of STING Agonists for Cancer Immunotherapy. J. Clin. Med. 9, 3323 (2020).

27. F. Roberts, D. Zhu, C. Farquharson, V. E. Macrae, ENPP1 in the Regulation of Mineralization and Beyond. Trends Biochem. Sci. 44, 616–628 (2019).

28. K. I. Onyedibe, M. Wang, H. O. Sintim, ENPP1, an Old Enzyme with New Functions, and Small Molecule Inhibitors—A STING in the Tale of ENPP1. Molecules 24, 4192 (2019).

29. C. Stefan, S. Jansen, M. Bollen, Modulation of purinergic signaling by NPP-type ectophosphodiesterases. Purinergic Signal. 2, 361–370 (2006).

30. J. W. Goding, B. Grobben, H. Slegers, Physiological and pathophysiological functions of the ecto-nucleotide pyrophosphatase/phosphodiesterase family. Biochim. Biophys. Acta BBA - Mol. Basis Dis. 1638, 1–19 (2003).

31. K. Johnson, M. Polewski, D. van Etten, R. Terkeltaub, Chondrogenesis Mediated by PP i Depletion Promotes Spontaneous Aortic Calcification in NPP1−/− Mice. Arterioscler. Thromb. Vasc. Biol. 25, 686–691 (2005).

32. R. A. Albright, et al., ENPP1-Fc prevents mortality and vascular calcifications in rodent model of generalized arterial calcification of infancy. Nat. Commun. 6, 10006 (2015).

33. Y. Nitschke, et al., ENPP1-Fc prevents neointima formation in generalized arterial calcification of infancy through the generation of AMP. Exp. Mol. Med. 50, 1–12 (2018).

34. B. Lorenz-Depiereux, D. Schnabel, D. Tiosano, G. Häusler, T. M. Strom, Loss-of-Function ENPP1 Mutations Cause Both Generalized Arterial Calcification of Infancy and Autosomal-Recessive Hypophosphatemic Rickets. Am. J. Hum. Genet. 86, 267–272 (2010).

35. F. Rutsch, Y. Nitschke, R. Terkeltaub, Genetics in Arterial Calcification: Pieces of a Puzzle and Cogs in a Wheel. Circ. Res. 109, 578–592 (2011).

36. B. A. Maddux, et al., Overexpression of the insulin receptor inhibitor PC-1/ENPP1 induces insulin resistance and hyperglycemia. Am. J. Physiol.-Endocrinol. Metab. 290, E746–E749 (2006).

37. I. D. Goldfine, et al., The Role of Membrane Glycoprotein Plasma Cell Antigen 1/Ectonucleotide Pyrophosphatase Phosphodiesterase 1 in the Pathogenesis of Insulin Resistance and Related Abnormalities. Endocr. Rev. 29, 62–75 (2008).

38. H. Wang, et al., ATP-degrading ENPP1 is required for survival (or persistence) of long-lived plasma cells. Sci. Rep. 7, 17867 (2017).

39. R. Watanabe, et al., Enpp1 is an anti-aging factor that regulates Klotho under phosphate overload conditions. Sci. Rep. 7, 7786 (2017).

40. K. Kato, et al., Crystal structure of Enpp1, an extracellular glycoprotein involved in bone mineralization and insulin signaling. Proc. Natl. Acad. Sci. 109, 16876–16881 (2012).

41. K. Kato, et al., Structural insights into cGAMP degradation by Ecto-nucleotide pyrophosphatase phosphodiesterase 1. Nat. Commun. 9, 4424 (2018).

42. M. L. Dennis, et al., Crystal structures of human ENPP1 in apo and bound forms. Acta Crystallogr. Sect. Struct. Biol. 76, 889–898 (2020).

43. S. Jansen, et al., Structure of NPP1, an Ectonucleotide Pyrophosphatase/Phosphodiesterase Involved in Tissue Calcification. Structure 20, 1948–1959 (2012).

44. C. J. Bracken, et al., Bi-paratopic and multivalent VH domains block ACE2 binding and neutralize SARS-CoV-2. Nat. Chem. Biol. 17, 113–121 (2021).

45. L. C. Sayles, et al., Genome-Informed Targeted Therapy for Osteosarcoma. Cancer Discov., CD-17-1152 (2018).

46. C. R. Schott, et al., "Development and characterization of new patient-derived xenograft (PDX) models of osteosarcoma with distinct metastatic capacities" (Cancer Biology, 2023) https:/doi.org/10.1101/2023.01.19.524562 (January 29, 2023).

47. A. Wellner, et al., Rapid generation of potent antibodies by autonomous hypermutation in yeast. Nat. Chem. Biol. 17, 1057–1064 (2021).

48. A. Ravikumar, G. A. Arzumanyan, M. K. A. Obadi, A. A. Javanpour, C. C. Liu, Scalable, Continuous Evolution of Genes at Mutation Rates above Genomic Error Thresholds. Cell 175, 1946-1957.e13 (2018).

49. F. Zhang, et al., Structural basis of a novel PD-L1 nanobody for immune checkpoint blockade. Cell Discov. 3, 17004 (2017).

50. A. Markham, Envafolimab: First Approval. Drugs 82, 235–240 (2022).

51. A. M. Scott, J. D. Wolchok, L. J. Old, Antibody therapy of cancer. Nat. Rev. Cancer 12, 278–287 (2012).

52. M. Imai, C. Landen, R. Ohta, N.-K. V. Cheung, S. Tomlinson, Complement-Mediated Mechanisms in Anti-GD2 Monoclonal Antibody Therapy of Murine Metastatic Cancer. Cancer Res. 65, 10562–10568 (2005).

53. A. Musolino, et al., Immunoglobulin G Fragment C Receptor Polymorphisms and Clinical Efficacy of Trastuzumab-Based Therapy in Patients With HER-2/ neu –Positive Metastatic Breast Cancer. J. Clin. Oncol. 26, 1789–1796 (2008).

54. F. Nimmerjahn, J. V. Ravetch, Fcγ receptors as regulators of immune responses. Nat. Rev. Immunol. 8, 34–47 (2008).

55. W. H. Yeap, et al., CD16 is indispensable for antibody-dependent cellular cytotoxicity by human monocytes. Sci. Rep. 6, 34310 (2016).

56. A. Salmerón, F. Sánchez-Madrid, M. A. Ursa, M. Fresno, B. Alarcón, A conformational epitope expressed upon association of CD3-epsilon with either CD3-delta or CD3-gamma is the main target for recognition by anti-CD3 monoclonal antibodies. J. Immunol. Baltim. Md 1950 147, 3047–3052 (1991).

57. M. Compte, et al., Functional comparison of single-chain and two-chain anti-CD3-based bispecific antibodies in gene immunotherapy applications. OncoImmunology 3, e28810 (2014).

58. A. D. Cotton, D. P. Nguyen, J. A. Gramespacher, I. B. Seiple, J. A. Wells, Development of Antibody-Based PROTACs for the Degradation of the Cell-Surface Immune Checkpoint Protein PD-L1. J. Am. Chem. Soc. 143, 593–598 (2021).

59. K. Pance, et al., Modular cytokine receptor-targeting chimeras for targeted degradation of cell surface and extracellular proteins. Nat. Biotechnol. (2022) https:/doi.org/10.1038/s41587-022-01456-2 (December 20, 2022).

60. G. Ahn, et al., LYTACs that engage the asialoglycoprotein receptor for targeted protein degradation. Nat. Chem. Biol. 17, 937–946 (2021).

61. J. A. Gramespacher, A. D. Cotton, P. W. W. Burroughs, I. B. Seiple, J. A. Wells, Roadmap for Optimizing and Broadening Antibody-Based PROTACs for Degradation of Cell Surface Proteins. ACS Chem. Biol. 17, 1259–1268 (2022).

62. C. Meazza, P. Scanagatta, Metastatic osteosarcoma: a challenging multidisciplinary treatment. Expert Rev. Anticancer Ther. 16, 543–556 (2016).

63. M. Schorb, I. Haberbosch, W. J. H. Hagen, Y. Schwab, D. N. Mastronarde, Software tools for automated transmission electron microscopy. Nat. Methods 16, 471–477 (2019).

64. A. Punjani, J. L. Rubinstein, D. J. Fleet, M. A. Brubaker, cryoSPARC: algorithms for rapid unsupervised cryo-EM structure determination. Nat. Methods 14, 290–296 (2017).

65. A. Punjani, H. Zhang, D. J. Fleet, Non-uniform refinement: adaptive regularization improves single-particle cryo-EM reconstruction. Nat. Methods 17, 1214–1221 (2020).

Publishing Agreement

It is the policy of the University to encourage open access and broad distribution of all theses, dissertations, and manuscripts. The Graduate Division will facilitate the distribution of UCSF theses, dissertations, and manuscripts to the UCSF Library for open access and distribution. UCSF will make such theses, dissertations, and manuscripts accessible to the public and will take reasonable steps to preserve these works in perpetuity.

I hereby grant the non-exclusive, perpetual right to The Regents of the University of California to reproduce, publicly display, distribute, preserve, and publish copies of my thesis, dissertation, or manuscript in any form or media, now existing or later derived, including access online for teaching, research, and public service purposes.

DocuSigned by:
Solomon, Paige
3F5312802E3F477...
Author Signature

3/11/2023
Date